

ELECTRON BEAM WELDING OF SELECTIVE LASER MELTED INCONEL 718

A Thesis

by

AKASH RAJENDRA SALI

Submitted to the Office of Graduate and Professional Studies of
Texas A&M University
in partial fulfillment of the requirements for the degree of

MASTER OF SCIENCE

Chair of Committee, Wayne Hung
Committee Members, Angie Hill Price
Bruce Tai

Head of Department, Andreas A. Polycarpou

December 2020

Major Subject: Mechanical Engineering

Copyright 2020 Akash Rajendra Sali

ABSTRACT

Selective Laser Melting (SLM) can produce near-net shaped parts, but their sizes are limited by the small dimensions of current powder bed fusion machines. This research applies Electron Beam Welding (EBW) to join SLM'ed Inconel 718 (IN718) parts by characterizing the welds based on their material and mechanical properties and comparing them with their rolled counterparts. Weld properties of the Hot Isostatically Pressed (HIP) samples were also compared. The dependent variable, electron beam heat input was varied between the range 180J/mm to 295J/mm to weld 12.7mm thick Inconel 718 samples. To analyze the quality of the welds, microhardness tests, tensile tests, and microstructure analysis of the fracture surfaces using optical and scanning electron microscope were executed. The chemical composition of various phase particles on the weld fracture surfaces was identified using the energy dispersive spectroscopy. Excellent weld penetration depths were achieved which were directly proportional to the electron beam heat input. Root void defects were observed at high heat inputs. SLM'ed IN718 samples had excellent yield and tensile strength that exceeded the rolled samples and the ASTM F3055-14a specification; however, they had inferior ductility. The HIP samples in this study were rather brittle. The brittleness of SLM'ed IN718 was due to the presence of brittle Laves phase, Nb-rich carbides, and Al-Ti-Oxides in the material matrix due to non-optimal SLM parameters. These issues can be reduced further by implementing optimal SLM parameters, and various post-processing techniques on the SLM'ed metal.

CONTRIBUTORS AND FUNDING SOURCES

Contributors

This work was supervised by a thesis committee consisting of Dr. Wayne Hung and Dr. Bruce Tai of the Department of Mechanical Engineering and Dr. Angie Price of the Department of Manufacturing and Mechanical Engineering Technology

Mr. Rodney Inmon of the Department of Aerospace Engineering assisted in Tensile Testing and Mr. Tom Stephens of Microscopy and Imaging Center guided the use of the Scanning Electron Microscope and Electric Discharge Spectroscopy system.

Funding Sources

Selective Laser Melted Inconel 718 samples and fabrication services were kindly provided by Knust-Godwin SBO, Houston, Texas.

NOMENCLATURE

ASTM	American Society for Testing and Materials
DTA	Differential Thermal Analysis
EBW	Electron Beam Welding
EDM	Electrical Discharge Machining
EDS	Energy Dispersive Spectroscopy
HAZ	Heat Affected Zone
HIP	Hot Isostatic Pressing
IN718	Inconel 718
SEM	Scanning Electron Microscope
SLM	Selective Laser Melting
SR	Stress Relieved
TEM	Transmission Electron Microscope
UTS	Ultimate Tensile Strength
VH	Vickers Hardness
YS	Yield Strength

TABLE OF CONTENTS

	Page
ABSTRACT	ii
CONTRIBUTORS AND FUNDING SOURCES.....	iii
NOMENCLATURE.....	iv
TABLE OF CONTENTS	v
LIST OF FIGURES.....	vii
LIST OF TABLES	xiii
1. INTRODUCTION.....	1
2. LITERATURE REVIEW	3
2.1. Secondary phases of Inconel 718.....	4
2.2. Selective Laser Melted IN718.....	6
2.3. Hot Isostatic Pressing.....	11
2.4. Joining of IN718	15
2.4.1. Laser welding of rolled IN718	15
2.4.2. EBW of rolled IN718	17
2.4.3. Pore or void formation mechanisms in Electron Beam Welds	23
2.4.4. Joining of SLM'ed IN718	26
2.5. Joining of other SLM'ed metals.....	28
3. EXPERIMENTS	34
3.1. Equipment and software:.....	35
3.2. Selective laser melting of Inconel 718	36
3.3. Hot Isostatic Pressing.....	39
3.4. Defining welding variables	40
3.5. Electron beam welding.....	42
3.6. Stress relieving.....	42
3.7. Hardness sample preparation	43
3.7.1. Molding	46
3.7.2. Grinding.....	48
3.7.3. Polishing.....	50

3.7.4. Etching.....	52
3.8. Tensile Sample Preparation.....	52
3.9. Testing.....	54
3.9.1. Microscopy.....	54
3.9.2. Micro Hardness Test.....	57
3.9.3. Tensile test.....	61
3.9.4. Microstructure Analysis.....	66
4. RESULTS AND DISCUSSION.....	70
4.1. Weld profile and defects.....	70
4.2. Tensile properties.....	76
4.3. Microhardness.....	81
4.4. Fractography.....	84
5. CONCLUSION.....	91
REFERENCES.....	93
APPENDIX A TENSILE STRESS-STRAIN CURVES.....	97
APPENDIX B MICROGRAPHS.....	102
APPENDIX C FRACTOGRAPHY.....	108
APPENDIX D ENERGY DISPERSIVE SPECTROSCOPY.....	111
APPENDIX E MICROHARDNESS.....	116

LIST OF FIGURES

	Page
Figure 2.1 Solidification diagram for IN718 (Adapted from Knorovsky et al., 1989)	5
Figure 2.2 Vickers Hardness test results for SLM'ed IN718 (Adapted from Deng et al., 2018)	9
Figure 2.3 Tensile test results for SLM'ed IN718 (Adapted from Deng et al., 2018)	9
Figure 2.4 Porosity of SLM'ed IN718 samples after HIP at various temperatures and pressures (Adapted from Tillmann et al., 2017)	13
Figure 2.5 Laser welding characteristics for rolled IN718 samples. (Adapted from Hong et al., 2008)	16
Figure 2.6 Weld width vs heat input for rolled IN718 (Adapted from Agilan et al., 2014)	20
Figure 2.7 Schematic of EBW and various defects (Adapted from Arata et al., 1973) ...	24
Figure 3.1 Flow chart of the experimentation process	34
Figure 3.2 Schematic of sample to be produced using SLM and corresponding SLM build direction.....	36
Figure 3.3 Building arrangement of SLM samples on the SLM machine base and respective laser assignment.....	37
Figure 3.4 Schematic of the setup for the EBW process.....	42
Figure 3.5 Schematic for Wire-EDM of hardness coupons	43
Figure 3.6 Molded hardness coupons.....	46
Figure 3.7 (A) CitoPress-15 molding machine; (B) Powder dispenser; (C) AntiStick powder	46
Figure 3.8 (A) Struers Uniforce grinding fixture; (B) Struers AbraPol-20 grinding and polishing machine; (C) Control Panel	48
Figure 3.9 (A) Grinding Wheels: (i) Emery - 80, (ii) Piano MD – 80, (iii) Piano MD – 220, (iv) Piano MD – 500, (v) Piano MD – 1200; (B) Sandstone block.....	50
Figure 3.10 (A) Dremel 4300 hand polisher; (B) Diamond polishing pastes	51

Figure 3.11 Struers Metason 200 ultrasonic cleaner	51
Figure 3.12 Design of tensile samples; Unit: mm	52
Figure 3.14 Typical tensile sample as per ASTM E8 subsize standard: (A) Front, (B) Side, (C) & (D) Label engravings on both ends of the specimen.....	53
Figure 3.15 As-built measurement locations on the tensile specimen; M1, M2, M3: gage section measurements; B1, B2, T1, T2: grip section measurements	54
Figure 3.16 Olympus STM 6 optical microscope	57
Figure 3.17 Schematic plan for hardness testing.....	58
Figure 3.18 Wilson VH1202 Vickers hardness tester	59
Figure 3.19 (A) MTS 810 tensile testing machine; (B) Arrangement of the tensile specimen in the crossheads; (C) Manual remote controller for crosshead movement	62
Figure 3.20 3D printed ABS plastic spacer to ensure the vertical alignment of the test sample on the tensile tester	63
Figure 3.21 Typical screen of MTS Station Manager Software	65
Figure 3.22 Real-time force-displacement-run time meters on the MTS Station Manager software	65
Figure 3.23 (A) Vega3 Tescan SEM; (B) Sample placement in the SEM chamber; (C) Controller; (D) Oxford Instruments x-act EDS system	68
Figure 3.24 VegaTC software screen	68
Figure 3.25 Aztec EDS software screen.....	69
Figure 4.1 (a) Spherical pore in SLM base metal surface of sample 11A (b) Pores and voids towards the end of the SLM base metal of sample 19B.....	71
Figure 4.2 Weld geometry for SLM+HIP+EBW samples 1A - 6A; K – Keyhole root void	72
Figure 4.3 Weld Geometry for SLM+HIP+EBW samples 7A to 9A and SLM+EBW samples 11A to 13A; K – Keyhole root void	72
Figure 4.4 Weld geometry for SLM+EBW samples 14A to 19A.....	73

Figure 4.5. Various defects in EBW of SLM'ed samples - Voids at nail head do not repeat in twin sample of (a) SLM+EBW sample 12A (272.6 J/mm) and (b) 17A (213.2 J/mm); (c) Unmelted lump defects in SLM+EBW sample 13A (249.8 J/mm);.....	74
Figure 4.6 Effect of E-Beam heat input on weld penetration depths of the welded samples.	75
Figure 4.7 Effect of beam current of weld area for the welded SLM samples. Weld area increased with an increase in beam current and a decrease in welding speed.	76
Figure 4.8 Typical Stress-Strain curve for the samples welded at a heat input of 180.4 J/mm. A91 curve is shifted by 25MPa, the 19A curve is shifted by 0.01 strain, and 9A-B curves are shifted by 0.025 strain for better visualization. ...	77
Figure 4.9 Variation of (a) Yield Strength, (b) Ultimate Tensile Strength and (c) Elongation of welded samples with E-Beam heat input.....	80
Figure 4.10 Microhardness of samples welded at 180.4J/mm: (a) SLM+HIP+EBW sample 9A/B, (b) SLM+EBW sample 19A/B, and (c) Rolled+EBW sample A9	83
Figure 4.11 Average hardness of each type of sample at high (295.3J/mm), medium (228.6J/mm), and low(180.4J/mm) heat inputs	84
Figure 4.12 SEM fractography of sample 20A (as-printed SLM); (a,b): Un-melted IN718 powder particles (Label 1 & 3), unfilled zone (label 2); (c) & (d) Brittle Laves (label 4)	85
Figure 4.13 SEM fractography of SLM+EBW sample 16A (209.6 J/mm) that fractured in the base metal; (a) Spherical pores (label 1) and (b) Brittle carbides (label 2).....	86
Figure 4.14 (a) Unfused SLM layer (label 1) and (b) Delaminated layer between the powder particle and the material matrix (label 2) on the fracture surface of sample 17B (213.2 J/mm). This sample fractured in the weld HAZ.....	87
Figure 4.15 EDS analysis of a site on the fracture surface of sample 17B (213.2 J/mm) indicating the presence of metal oxides.....	87
Figure 4.16 EDS analysis of a site on the fracture surface of SLM+HIP+EBW sample 7A (213.2 J/mm) showing disjointed IN718 layers (A and B).....	88

Figure 4.17 SEM fractography of SLM+HIP+EBW sample 7A (213.2 J/mm) indicating brittle surface. This sample was fractured in the weld HAZ.	88
Figure 5.1 Stress-strain curve for samples welded at heat input 295.3 J/mm (1A/B - SLM+HIP+EBW, 11A/B - SLM+EBW).....	97
Figure 5.2 Stress-strain curve for samples welded at heat input 272.6 J/mm (2A/B - SLM+HIP+EBW, 12A/B - SLM+EBW).....	97
Figure 5.3 Stress-strain curve for samples welded at heat input 249.8 J/mm (3A/B - SLM+HIP+EBW, 13A/B - SLM+EBW).....	98
Figure 5.4 Stress-strain curve for samples welded at heat input 247.6 J/mm (4A/B - SLM+HIP+EBW, 14A/B - SLM+EBW).....	98
Figure 5.5 Stress-strain curve for samples welded at heat input 228.6 J/mm (5A/B - SLM+HIP+EBW, 15A/B - SLM+EBW).....	99
Figure 5.6 Stress-strain curve for samples welded at heat input 209.6 J/mm (6A/B - SLM+HIP+EBW, 16A/B - SLM+EBW).....	99
Figure 5.7 Stress-strain curve for samples welded at heat input 213.2 J/mm (7A/B - SLM+HIP+EBW, 17A/B - SLM+EBW).....	100
Figure 5.8 Stress-strain curve for samples welded at heat input 196.8 J/mm (8A/B - SLM+HIP+EBW, 18A/B - SLM+EBW).....	100
Figure 5.9 Stress-strain curve for as printed samples (10A/B - SLM+HIP+EBW, 20A/B - SLM+EBW).....	101
Figure 5.10 Defects on SLM+HIP+EBW sample 1A/1B (295.3 J/mm).....	102
Figure 5.11 Defects on SLM+HIP+EBW sample 3A/3B (249.8 J/mm).....	102
Figure 5.12 Defects on SLM+HIP+EBW sample 4A/4B (247.6 J/mm).....	103
Figure 5.13 (A) Root keyhole defect on SLM+HIP+EBW sample 5A/5B (228.6 J/mm) (B) Pores on SLM+HIP+EBW sample 5A/5B base metal (228.6 J/mm)	103
Figure 5.14 (A) Root keyhole defect on SLM+HIP+EBW sample 6A/6B (209.6 J/mm) (B) Defect on SLM+HIP+EBW sample 6A/6B weld (209.6 J/mm)...	104
Figure 5.15 (A) Pore on SLM+HIP+EBW sample 7A/B weld (213.2 J/mm) (B) Defect on SLM+HIP+EBW sample 7A/B base metal (213.2 J/mm)	104

Figure 5.16 (A) Defect on SLM+HIP+EBW sample 8A/B weld (196.8 J/mm) (B) Crack on SLM+HIP+EBW sample 8A/B base metal (196.8 J/mm)	104
Figure 5.17 Defect on SLM+EBW sample 11A/B base metal (295.3 J/mm).....	105
Figure 5.18 Defects on SLM+EBW sample 13A/B base metal (249.8 J/mm)	105
Figure 5.19 Defects on SLM+EBW sample 14A/B base metal (247.6 J/mm)	105
Figure 5.20 Pores on SLM+EBW sample 15A/B (228.6 J/mm).....	106
Figure 5.21 Pores on SLM+EBW sample 16A/B (209.6 J/mm) base metal.....	106
Figure 5.22 Defects on SLM+EBW sample 17A/B (213.2 J/mm) weld boundary	106
Figure 5.23 Pore on SLM+EBW sample 18A/B (196.8 J/mm) weld boundary	107
Figure 5.24 Pore on SLM+EBW sample 19A/B (180.4 J/mm) weld	107
Figure 5.25 Fractography of SLM+EBW sample 16A/B (209.6 J/mm) fractured in the base metal	108
Figure 5.26 Fractography of SLM+EBW sample 17A/B (213.2 J/mm) fractured on the weld HAZ	109
Figure 5.27 Fractography of as-printed SLM sample 20A/B.....	110
Figure 5.28 EDS of SLM+HIP+EBW sample 7A/B (213.2 J/mm) site 1	111
Figure 5.29 EDS of SLM+HIP+EBW sample 7A/B (213.2 J/mm) site 2	111
Figure 5.30 EDS of SLM+EBW sample 16A/B (209.6 J/mm) site 1	112
Figure 5.31 EDS of SLM+EBW sample 16A/B (209.6 J/mm) site 2	112
Figure 5.32 EDS of SLM+EBW sample 16A/B (209.6 J/mm) site 3	113
Figure 5.33 EDS of SLM+EBW sample 16A/B (209.6 J/mm) site 4	113
Figure 5.34 EDS of SLM+EBW sample 17A/B (213.2 J/mm) site 1	114
Figure 5.35 EDS of SLM+EBW sample 17A/B (213.2 J/mm) site 2	114
Figure 5.36 EDS of non-welded sample 20A/B site 1	115
Figure 5.37 EDS of non-welded sample 20A/B site 2	115

Figure 5.38 Microhardness test result of SLM+HIP+EBW sample 1A/B (295.3 J/mm)	116
Figure 5.39 Microhardness test result of SLM+EBW sample 11A/B (295.3 J/mm)	116
Figure 5.40 Microhardness test result of SLM+EBW sample 15A/B (228.6 J/mm)	117

LIST OF TABLES

	Page
Table 2.1 Chemical composition of IN718 (wt %) (Adapted from Voort, 1991).....	3
Table 2.2 Designation of Sample and corresponding heat treatments for SLM'ed IN718 (Adapted from Deng et al., 2018).....	8
Table 2.3 Chemical composition inside the oxide inclusion (Adapted from Popovich et al., 2017)	14
Table 2.4 Tensile properties of the friction welded samples (Adapted from Prashanth et al., 2014)	32
Table 3.1 SLM parameters	38
Table 3.2 Chemical composition (wt%) of IN718 powder (Luvak Laboratories, n.d.) and ASM specification (Adapted from Voort, 1991)	39
Table 3.3 HIP parameters	40
Table 3.4 EBW parameters set as constants for the experiment	41
Table 3.5 Welding variables explored in the experiments	41
Table 3.6 Stress-relieving parameters	43
Table 3.7 Labeling scheme for hardness samples	44
Table 3.8 Grinding Steps.....	49
Table 3.9 Hardness test parameters	59
Table 3.10 Tensile test parameters	61
Table 4.1 Tensile properties of SLM+HIP+EBW samples.....	78
Table 4.2 Tensile properties of SLM+EBW samples	79

1. INTRODUCTION

Selective laser melting is a powder bed fusion process in which parts are built layer-by-layer with atomized metal powder. SLM can produce near-net-shaped parts with minimal material wastage as compared to conventional subtractive manufacturing processes. This unconventional method of producing parts provides greater geometrical flexibility to their designs with fewer constraints on manufacturability. It has exceeded from being a mere rapid prototyping technique to a method of manufacturing components that can be used in real engineering applications. Despite the advantages of SLM'ed parts, given the constraint on the chamber size of the powder bed fusion machines, their dimensions are limited. Consequently, current SLM machines fail to meet the requirement for large complex-shaped components desired by various industries such as aerospace, defense, automotive, nuclear, and energy. Thus, the development of efficient ways to join the smaller Selective Laser Melted components is necessary to utilize additive manufacturing to its full potential.

Inconel 718 superalloy is widely used in the above-mentioned industries. This is due to its superior mechanical properties such as tensile strength, hardness, creep resistance, and corrosion resistance even at temperatures as high as 650°C. Given their stable grain structure and strain hardening properties, it is expensive to execute complex machining operations on the conventionally manufactured IN718 parts. Thus, the SLM of IN718 has gained popularity to produce intricate parts. Welding of IN718 also comes with its challenges and thus has been explored widely by various researchers. Among all

the welding processes, Electron Beam Welding could provide excellent results in terms of weld quality and strength. It also exerts less thermal stress on the base metal thereby imposing minimal chemical and microstructural changes. Further, no literature is found on EBW of SLM'ed IN718. It is thus necessary to explore EBW to join SLM'ed IN718 parts. The objectives of this research are:

1. To weld and optimize the EBW parameters for joining of SLM'ed IN718.
2. To compare the weld properties with the rolled IN718 welds.
3. To identify the issues for improvement.

2. LITERATURE REVIEW

IN718's superior mechanical properties even at high temperatures are associated with precipitation of secondary phases at higher temperatures. Its chemical composition is defined in Table 2.1 as per ASM specifications.

Table 2.1 Chemical composition of IN718 (wt %) (Adapted from Voort, 1991)

Ni	Cr	Fe	Nb	Mo	Ti	Al	C	Co	Cu	Si	Mg
50-55	17-21	~17	4.75-5.5	2.8-3.3	0.65-1.15	0.2-0.8	<0.8	<1.0	<0.3	<0.35	<0.35

Many research articles discuss the phase change behavior of Inconel based on temperature and its effect on mechanical properties. SLM of IN718 has gained popularity with enhanced additive manufacturing equipment and product quality. This has led to widespread research on the effects of various SLM parameters on the quality of printed parts. To further enhance the quality of SLM'ed IN718, the hot isostatic process has also been explored. Various methods to join IN718 have been previously evaluated by many researchers. Electron Beam Welding and Laser welding are some of the most widely researched methods explored to join IN718 manufactured by conventional methods. Joining SLM'ed components has also gained popularity due to a need for large complex-shaped parts. Laser Welding, Electron Beam Welding, and Laser-arc hybrid welding are some of the methods explored for other SLM'ed materials. Whereas, Tungsten inert gas welding and brazing methods have been researched for joining of SLM'ed IN718.

2.1. Secondary phases of Inconel 718

IN718 was initially developed to provide high tensile properties. But, due to various secondary phases of the alloy and their stability at various temperature conditions, the material also showed good high temperature creep properties (EISELSTEIN, 1965). These secondary phases also affect the age-hardening properties of the alloy and the ensuing brittleness or ductility. It is thus important to understand the mechanisms behind the formation of these secondary phases.

An attempt was made to define a solidification phase diagram for IN718 using various phase compositions formed after a nonequilibrium welding process (Knorovsky et al., 1989). Four different commercial compositions of IN718 with element wt% as follows - Al(0.56-0.76), B(0.002-0.003), C(0.04-0.05), Cr(18.18-18.34), Fe(17.84-18.26), Mn(0.13-0.14), Mo(3.01-3.12), N(0.007-0.011), Nb(5.14-5.25), O(0.001), P(0.012-0.014), S(0.001-0.003), Si(0.19-0.23), Ti(0.9-1.01), and Ni(Rest) - were used for conducting the experiments. Before any experiments, the specimens were exposed to heat treatment at 1000°C for time <1hr.

To define the solidification diagram, Differential Thermal Analysis (DTA) was performed using DuPont 1090 on the specimen of weight 0.1g to 0.2g. The analysis parameters were: Heating rate of 10°C/min until they reached a temperature of 1450°C. Heating was conducted in an Argon-controlled environment. The samples were then cooled through all significant solidification temperature ranges also at a rate of 10 °C /s. To understand the phases formed after the welding process, metallography was performed on Inconel plates of 25mm width x 3mm thickness x 165mm long welded by

Gas Tungsten Arc Welding. The welding parameters were: 90A current, 3.6mm/min travel speed, 14J/m argon shielding, 1mm arc gap, and 60° tip angle using a 1mm diameter W-2 pct ThO₂ electrode. SEM, TEM, and Electron Micro Probe were used to obtain the microstructure of secondary phases and metallographic composition of constituent elements. Experimental electromagnetic pulse composition was compared with Analytical Electron microscopy composition for identification. The solidification diagram was made using Nb as the main composition element as it is a contributing element to various important phases under consideration. The DTA gave the various phase change and reaction temperatures. The solidification diagram prepared based on DTA and microanalysis considering an ideal interstitial free alloy was as shown in Figure 2.1.

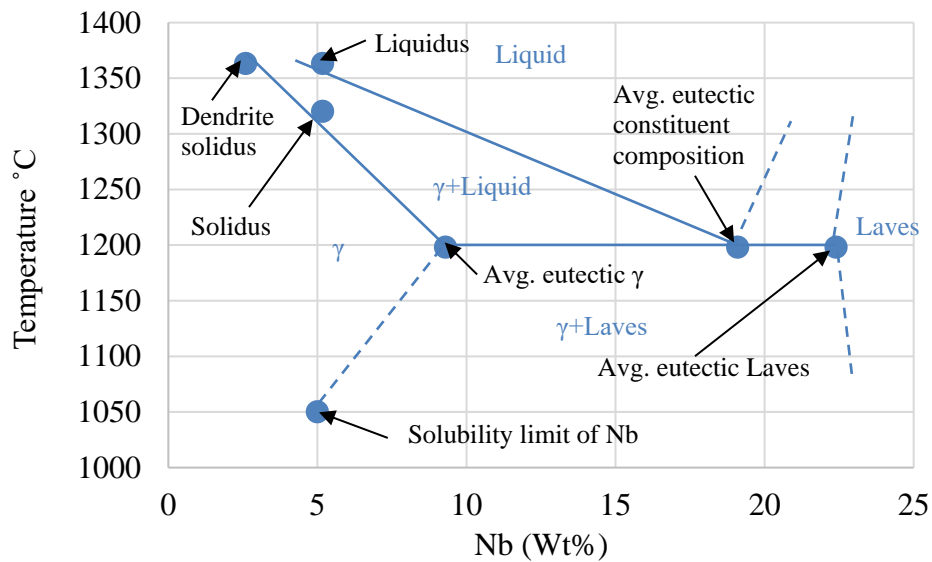


Figure 2.1 Solidification diagram for IN718 (Adapted from Knorovsky et al., 1989)

2.2. Selective Laser Melted IN718

Selective laser melted components generally exhibit inferior mechanical properties as compared to the conventionally manufactured components due to various factors. Layer wise building followed by quick solidification, localized heating and cooling leading to residual stresses, and inevitable development of pores due to lack of fusion or shrinkage are some of the factors that contribute to unconventional mechanical properties of SLM'ed components (Deng et al., 2018). Many researchers have explored these factors and their effect on the mechanical properties and the metallography of the component. Layer-wise build-up tends to give SLM'ed components an anisotropic nature leading to unequal mechanical properties in different directions.

Deng et al., 2018 compared the difference in mechanical properties of SLM'ed IN718 that were built in vertical and horizontal directions. In case of vertically built samples the tensile loading direction was along the print build direction while in case of the horizontally built samples, the tensile loading direction was perpendicular to the print build direction. The effect of various heat treatments was also studied. The samples were built on the EOS M290 machine using 65 μ m gas atomized IN718 powder. Layer height was set at 40 μ m and the building platform was preheated at 80°C. Argon vacuum was used to keep the environment free of oxygen. The samples were not subjected to any stress-relieving or HIP. But they were subjected to different heat treatments as shown in Table 2.2. The room temperature tensile tests were conducted on the Instron 5582 universal tensile machine with 100KN Load Cell at a strain rate of 0.01%/s measured

using a digital image correlation system. Vickers Hardness test was conducted on Struers DuraScan G5 tester using 300gf load and 15s dwell time.

No effect of specimen orientation was observed on the hardness of the samples. The heat treatments did increase the hardness of the specimens to ~ 350 HV as compared to 325 HV for AS samples. The improvement was associated with the precipitation of the strengthening γ'' phase and release of Nb from Laves back into the material matrix. Figure 2.2 shows a detailed comparison of the hardness values. The tensile properties show a significant dependence on the sample orientation. Samples that were built in vertical direction show inferior yield and tensile strengths as compared to the horizontally built samples. This dependence of tensile properties on the sample orientation was associated with the difference in crystallographic orientation and different amounts of residual stresses and dislocations accumulated in the tensile loading direction for each type of sample. Heat treatments also improve the tensile properties of the specimens. An opposite trend is observed for the ductility as indicated by %elongation at fracture for these samples. Refer Figure 2.3 for tensile test results.

Table 2.2 Designation of Sample and corresponding heat treatments for SLM'ed IN718 (Adapted from Deng et al., 2018)

Specimen Designation	Heat Treatment Condition
As Manufactured (AS)	None
Direct Ageing (DA)	720°C/8h/Furnace Cooling at 50°C/h to 620°C + 620°C/8h/Air Cooling
Solution Treatment + Dual Aging (SA)	<ul style="list-style-type: none"> • Solution Treatment: 980°C/1h/Water Cooling • Dual Aging: 720°C/8h/Furnace Cooling at 50°C/h to 620°C + 620°C/8h/Air Cooling
Homogenization + Dual Aging (HA)	<ul style="list-style-type: none"> • Homogenization: 1080°C/1h/Water Cooling • Dual Aging: 720°C/8h/Furnace Cooling at 50°C/h to 620°C + 620°C/8h/Air Cooling
Homogenization + Solution Treatment + Dual Aging (HSA)	<ul style="list-style-type: none"> • Homogenization: 1080°C/1h/Water Cooling • Solution Treatment: 980°C/1h/Water Cooling • Dual Aging: 720°C/8h/Furnace Cooling at 50°C/h to 620°C + 620°C/8h/Air Cooling

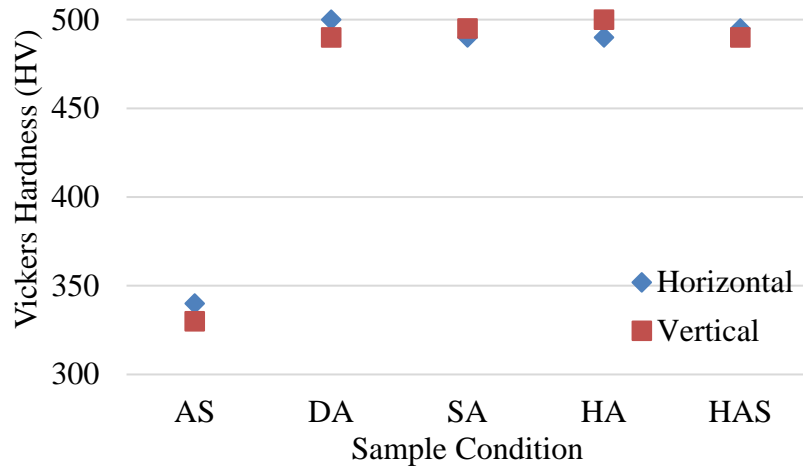


Figure 2.2 Vickers Hardness test results for SLM'ed IN718 (Adapted from Deng et al., 2018)

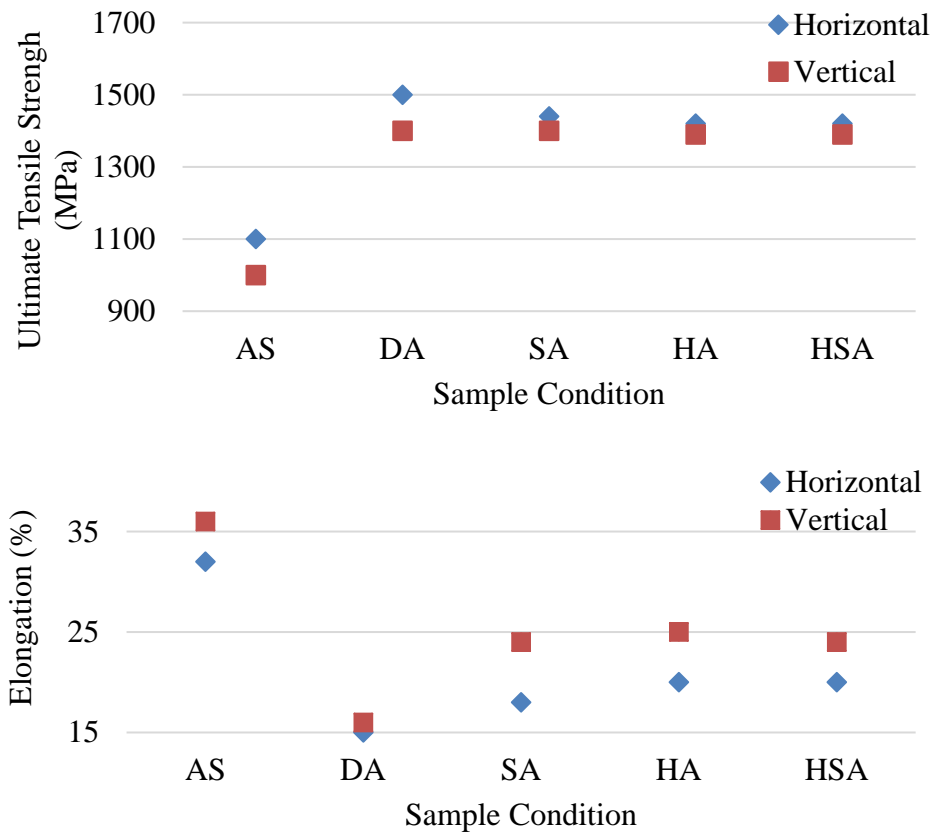


Figure 2.3 Tensile test results for SLM'ed IN718 (Adapted from Deng et al., 2018)

These observations were further supported by the results of another research study (Ströbner et al., 2015). Again, gas atomized IN718 powder was used to build cylindrical specimens of 13mm diameter and 70mm long with a powder layer thickness of 20 μ m in vertical and horizontal directions. The scanning layer was oriented in an optimal angle but scanned in the direction opposite to the previous layer. Two sets of heat treatments were performed: HT1 being based on AMS 5662 standard (Solution treatment at 980°C/1h/air cooling, followed by dual aging: 720°C/10h/furnace cooling for 2h to 650°C + 620°C/8h), and HT2 is based on AMS 5664 standard (Homogenization at 1065°C/1h followed by HT1 process). Tensile Tests were carried out at the room and two elevated temperatures (450°C and 650°C) using Zwick Z100 tester and using parameters defined in EN 100 02-1 and EN 100 02-2 standards respectively. Three repetitions of each test were conducted. Rockwell hardness tests were conducted at a load of 150kip and Vickers hardness tests were performed at a load of 10kip.

The room temperature tensile test results indicated anisotropic behavior with vertically built samples exhibiting lower tensile strength and Hardness values, but higher fracture elongation as compared to horizontally built samples. Heat-treated samples had better tensile strengths and hardness values but lower elongation at fracture as compared to the as-built samples. The hardness values were also higher for the horizontally built samples in the as-built state, but the difference vanished in heat-treated samples. High-temperature properties were lesser as compared to room temperature properties. The difference between the mechanical properties at different orientations was associated with the number of layers on the specimen. Vertical samples had a higher number of

layers leading to a higher number of joints in the loading direction. Further, the homogeneity of the alloy in the vertical direction was described to be weaker than the horizontal sample thereby leading to poor distribution of the γ'' phase. These two factors were associated with poor tensile properties of the vertical sample. Heat treatments showed improvement in mechanical properties as compared to as-built samples. Further, the difference between the properties of horizontal and vertical samples was also reduced after heat treatments. This was associated with the precipitation of the γ'' phase after aging.

2.3. Hot Isostatic Pressing

Due to the gases trapped in the molten pools of SLM metals, they tend to have a rather porous structure. This defect adversely affects the mechanical properties of the SLM'ed part. As explored by many researchers, HIP can be used to reduce this porosity. Research (Aydinöz et al., 2016) concluded that HIP not only reduces the porosity but this thermal process also leads to a change in the microstructure of the SLM'ed part. This leads to the elimination of submicron cells and long-grain structure. These microstructural changes were found to improve the ductility of the SLM'ed samples under monotonic tensile tests. 8mm x 3mm x 2.5mm sized specimen was built on a 250HL SLM machine using 30micron gas atomized IN718 powder. SLM machine was set at 30 μ m layer thickness, 540 mm/s scanning speed, and 100W laser power. The samples were exposed to HIP in an argon environment at 1150°C and 1000 bar pressure for 4 hours followed by free cooling in the furnace. The specimens were ground and polished to the grit size of 5microns and observed under the optical microscope,

scanning electron microscope, and energy dispersive spectroscopy for microstructure analysis. The tensile tests were conducted on a servo-hydraulic testing machine while the Vickers hardness test was conducted using a Microjet-Buhler system using a load of 9.81N.

Based on the microstructure analysis, HIP at a temperature of 1150°C led to the recrystallization of the SLM specimens leading to the coarsening of the grains and a loss of their columnar structure. This change in microstructure was associated by the authors to the high temperature and localized deformation during the HIP. Tensile and hardness properties were also affected by the HIP process. As-built SLM specimens had higher yield strength and hardness but low ultimate strength and ductility. This was associated with the presence of submicron cell structures, high density of dislocations, and laves. A fall in yield strength and rise in ductility after HIP was associated with microstructure evolution leading to the dissolution of laves, reduced dislocations, and elongated cell structures.

Another research (Tillmann et al., 2017) indicated the effect of various HIP parameters on the porosity of the samples SLM'ed using the same parameters as that by (Aydinöz et al., 2016). As shown in Figure 2.4 the porosity reduces as the HIP temperature and pressure are increased.

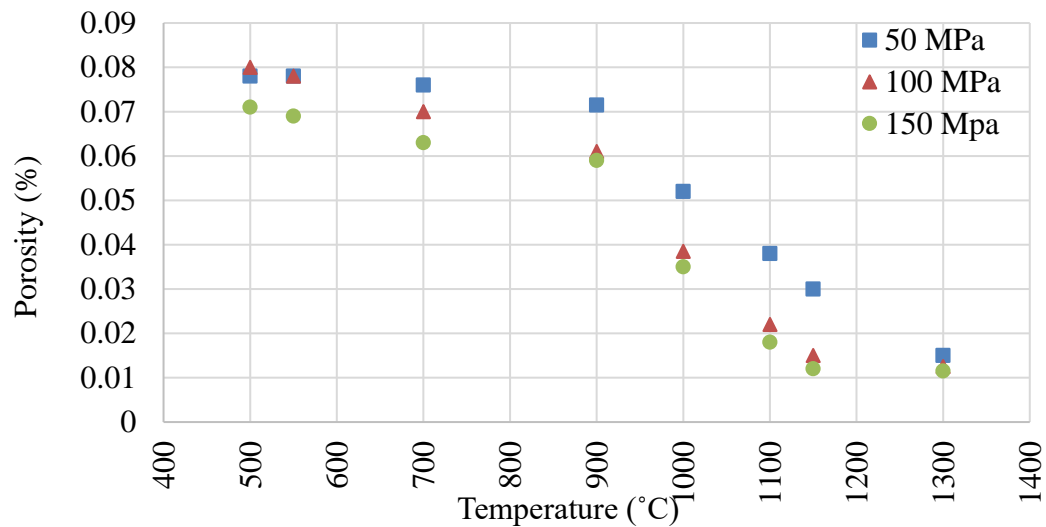


Figure 2.4 Porosity of SLM'ed IN718 samples after HIP at various temperatures and pressures (Adapted from Tillmann et al., 2017)

In another research (Popovich et al., 2017) an improvement in mechanical properties and porosity recorded after HIP was associated with the dissolution of γ' and δ phases. The 70 x 20 x 10 mm samples were SLM'ed on 280HL system at two different powers of 250W and 950W using gas atomized IN718 powder. 250W samples were built with 50 μ m layer thickness, 0.12mm hatch distance and 700mm/s scanning speed whereas 950W samples were built with 100 μ m layer thickness, 0.5mm hatch distance, and 320mm/s scanning speed. The samples were HIPed in an argon environment based on AMS 5664E at 1180°C for 3 hours at 150MPa pressure followed by furnace cooling. The specimens were machined to their final form using EDM followed by grinding and polishing to 3 microns. The samples were then tested with Zwick 100KN load cell tensile tester at a strain rate of 1.5mm/min and tested for Vickers hardness with 1kgf load. Samples were ground and polished to 1 micron and etched

using 15ml HCl, 10ml glycerol, and 5ml HNO₃ (Glyceregia reagent) for grain structure reveal and using 40ml HCl, 2g CuCl₂ and 40ml ethanol (Kalling's reagent) for precipitate reveal. The microstructure was analyzed using an optical microscope – Keyence VHX-5000 and SEM – JEOL JSM 6500F.

Microstructure analysis revealed closure of pore by plastic flow and grain growth after HIP. But here the columnar grain structure was not removed as seen in the by Aydinöz et al., 2016. NbC precipitates were also observed on the dendrite boundaries of HIP'ed samples contributing to improved ductility. HIP temperature also led to the dissolution of laves and lead to microstructure homogenization. There was a reduction in yield and tensile strength of the HIP'ed samples but improved elongation to fracture as compared to the as-processed SLM samples. The hardness of the HIP'ed samples was also found to be lesser as compared to the as-processed SLM samples.

EDS analysis of the tensile fracture surface of HIP'ed samples indicated the presence of Al₂O₃ within the enlarged cracked areas. These oxides were identified to be very brittle and had poor adhesion with the base metal. This led to the partial melting of the subsequent layer. Table 2.3 shows chemical composition inside the oxide inclusion as compared with typical Inconel 718.

Table 2.3 Chemical composition inside the oxide inclusion (Adapted from Popovich et al., 2017)

	O	Al	Cr
Oxide Inclusion	41	51	8
Typical	0	0.58	18.9

2.4. Joining of IN718

Welding processes like laser welding and electron beam welding have been widely researched for joining of IN718 given their favorable weld characteristics.

2.4.1. Laser welding of rolled IN718

Laser welding of rolled IN718 was explored by Hong et al., 2008. 5mm thick rolled IN718 plates with two different grain sizes as per ASTM #4 and ASTM #10 were welded using a CW CO₂ laser welding machine. Laser power was varied from 5kW to 10kW in steps of 1kW while the speed was varied from 1 m/min to 4m/min with steps of 0.5m/min. The samples were heat-treated before welding at two different conditions: solution treatment at 955 °C and solution treatment at 955 °C + aging (955 STA). After welding, the samples were heat-treated at three different conditions: direct aging (DA), solution treatment (955 °C) + aging, and cycle solution heat treatment (CHT) at 1000 °C for 3min followed by furnace cooling at 3 °C/min and then holding at 985 °C for 8min. Each sample was analyzed for its microstructure using an optical microscope and a scanning electron microscope. Tensile samples were machined as per ASTM E8 sub-size specimen dimensions.

A defect-free full penetration weld was achieved for the samples welded at laser-focused on the surface with 6kW power with 2.5m/min speed and at 8kW with 4m/min speed. Weld defects observed at other parameters were as shown in Figure 2.5.

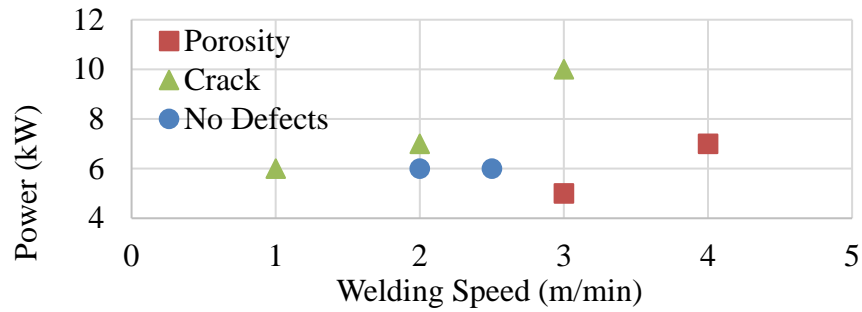


Figure 2.5 Laser welding characteristics for rolled IN718 samples. (Adapted from Hong et al., 2008)

Microstructure analysis revealed the presence of micro-fissures on HAZ of the large-grained IN718 welded with 6kW and 2.5m/min. No such fissures were observed on fine-grained samples. Micro fissures still existed for large-grained samples even after post-weld heat treatment. Carbides and delta phase precipitates were observed on the grain boundaries of these samples. No HAZ defects were recorded for post-weld treated fine-grained samples. Carbide and delta phase precipitates were also lower in volume.

The tensile properties of as-rolled specimens were higher than pre-weld treated samples. The poor performance of pre-weld treated samples was associated with Niobium segregation and delta phase precipitation after the heat treatment. The cyclic and aging post-weld heat-treated samples showed the best results for tensile tests due to crack liquidation and delta phase precipitation at grain boundaries. At this condition the UTS was 1417MPa, YS was 1265MPa, and the elongation was 5% as compared to base metal properties of 1380MPa, 1068MPa, and 18% respectively.

2.4.2. EBW of rolled IN718

One of the advantages of EBW is its capability to produce negligible heat-affected zones. Researchers studied the variation in the formation of EBW heat-affected zones and their properties at different pre-weld heat treatment conditions using microhardness measurements (C. A. Huang et al., 2005). 3mm x 40mm x 60mm IN718 sheets were used as the test specimen. These samples were heat-treated before welding at two different conditions: one by solution treatment at 950°C for 1 hour followed by quenching in water, and other by solution treatment followed by precipitation treatment at 760°C for 4h followed by water quenching. These samples were polished and cleaned for EBW using two different welding passes namely first pass (50kV, 100mA, 3.46mm depth, 2173mm/min feed) and second pass (50kV, 60mA, 3.42mm depth, 1524mm/min feed).

The EBW'ed samples were tested using Matsuzawa Digital Microhardness Tester with 300g load. A careful analysis was conducted to identify the indentation load to avoid inappropriate readings. It was observed that any load under 100gf gave a high variation in hardness measurements for IN718. Loads of 300gf and 500gf were found to be most suitable. The hardness test result revealed a lower hardness of the fusion zone/HAZ as compared to base metal for precipitation pretreated samples. As-received and solution pre-treated samples had a uniform hardness distribution. The spike in hardness values for precipitation treated samples was associated with their high thermal sensitivity and precipitation of γ' and γ'' phases in the HAZ.

Another research (Madhusudhana Reddy et al., 2009) tried to reduce the formation of laves phase and niobium segregation to improve the tensile properties of the weld by using various forms of electron beam oscillations during the welding process. The effects of post-weld heat treatments were also explored in this research. 205 x 105 x 3.1 mm solution treated IN718 plates were used for EBW.

The oscillations were performed in different patterns such as sine, square, triangular, ramp, circular, and elliptical patterns at frequencies ranging from 5 to 200 Hz. Least niobium segregation was observed at 15Hz oscillation frequency. The welded samples were treated by two solution treatments: 980°C/1h/air cooling and 1080 °C/1h/air cooling. After each of these treatments, dual aging was performed: 720 °C/8h/furnace cooling + 620 °C/8h/air cooling. All samples were analyzed for microstructure on SEM. The Vickers hardness test was performed at a load of 100gf. Tensile samples were prepared from welded samples based on the ASTM E8 standard and were tested on the INSTRON testing machine at a strain rate of 2mm/min.

Microstructure analysis revealed that the elliptical weld oscillations were the most effective in reducing the segregation of niobium and laves formation. This was associated with weld metal solidification. Oscillating welds led to the formation of several small weld pools at any point in time leading to better cooling rate, high fluid flow, and reduced thermal gradients in the weld pool. After solution treatment at 1080°C, the remnant laves phase completely dissolved and clear grain boundaries emerged. Although, this led to the formation of a large grain structure adversely affecting the mechanical properties of the base material.

The room temperature tensile test properties of the elliptical oscillated welds were higher as compared to unoscillated welds in both direct-aging and 980 °C solution treatment + aging conditions. The failure occurred in the weld zone for these samples. The samples treated at 1080 °C broke outside the weld.

EBW heat input plays a significant role in the fusion zone and HAZ microstructure, controlling liquation cracking and segregation of alloying elements (Agilan et al., 2014). Electron beam bead-on plate trials were conducted on 2mm thick cold rolled IN718 sheets that were thoroughly cleaned with acetone. Heat input was varied by varying beam current from 18mA to 90mA with a constant speed of 30mm/s and a constant voltage of 60kV. Five samples indicated as S1, S2, S3, S4, and S5 were chosen for analysis. The welded samples were polished and etched using oxalic acid for microstructure analysis under OLYMPUS GX-71 optical microscope and JEOL SEM.

The microstructure analysis revealed that, as the heat input was increased, the width of the fusion zone increased. This was due to the higher melting of base metal at higher beam current. The bead width at the middle portion of the weld was higher than that at the bottom for samples S1 and S5. The opposite was observed for other samples. Figure 2.6 shows the variation in bead width with heat inputs.

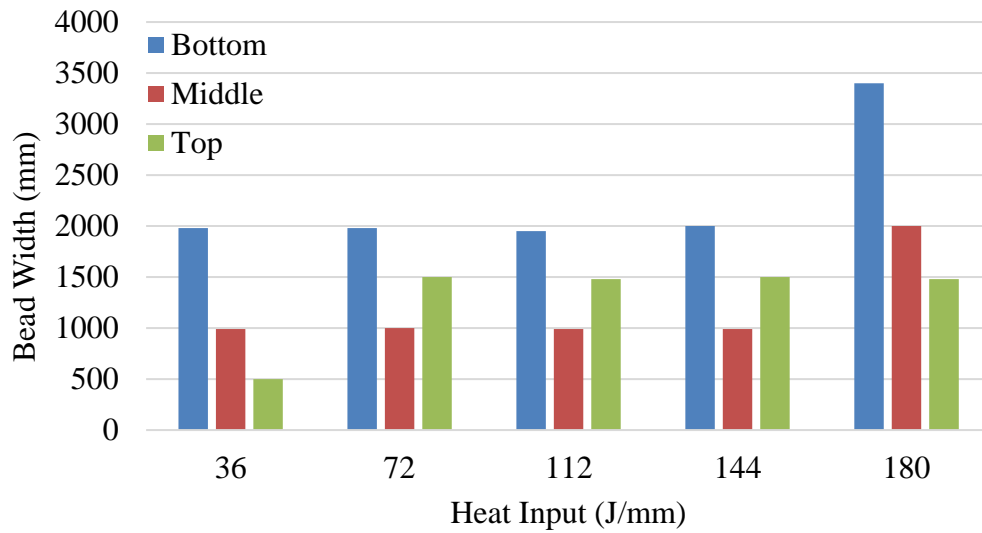


Figure 2.6 Weld width vs heat input for rolled IN718 (Adapted from Agilan et al., 2014)

SEM analysis also showed that there was significant segregation of Nb, Ti, and Mo in the interdendritic regions and Cr, Al, and Fe in the dendritic regions. Although, variation in the heat input did not seem to influence this behavior. But heat input variation did influence the formation of micro-fissures in HAZ. The lowest heat input sample indicated the presence of HAZ micro-fissures while all other samples were free from it. This was associated with a higher temperature gradient in HAZ at lower heat input providing higher grain boundary area for cracking.

The effect of base metal condition and welding speed on the weld geometry was observed in another research (Mei et al., 2016). 165mm x 26mm x 1.6mm IN718 plates were subjected to various heat treatments before welding: N4 - 1100 °C/1h /air-cooled; N3 - 1040 °C/1 h/air-cooled; N2 - 950 °C/1 h/air-cooled; N1 – as-rolled. All these samples were EBW'ed at a speed of 1270 mm/min. The effect of varying welding speed

was tested on sample B with three different speeds: N3 – 1270mm/min, N5 – 1207mm/min, and N6 – 1143mm/min. Other welding parameters were kept constant at 125kV voltage, 65mA beam current, and 400J/mm input energy. V restraint test was performed to test the specimen for cracking. The samples were polished and etched using Kalling's reagent and observed under the optical microscope and SEM with EDS for microstructure Analysis.

The microstructure analysis revealed an increase in the laves formation as the welding speed was decreased. This was associated with higher micro-segregation at the weld center. No such association of micro-segregation was observed with the base metal condition. The base metal configuration had a significant effect on HAZ cracking. All the specimens welded at the same welding speed indicated the presence of intergranular cracks. But, the increase in grain size with an increase in heat treatment temperature increased the cracking in HAZ. Welding speed also influenced HAZ cracking, where decreasing the welding speed led to a reduction in total crack length and average crack length.

Other research attempted EBW of 12 mm thick IN718 plates by using two weld passes, first full penetration pass at 60kV, 120mA and 11mm/s, and second cosmetic penetration pass at 60kV, 30mA and 11mm/s welding parameters (Gao et al., 2011). The gap between welding parts was maintained at 0.1mm for good surface quality. The welded samples were then heat-treated by solution treatment (980°C/1h/air cooling) and dual aging (720°C/8h/furnace cooling at 50°C/h + 620°C/8h/air cooling). The 12mm thick sample was cut into three along the thickness, each being 3.5mm thick. This was

done to analyze the mechanical properties of the thick weld at the top, middle, and bottom sections. The samples were polished and etched with a mixed acid solution and then observed under a microscope. Samples were tested at 650°C on Instron 5500R tensile testing machine. HVS-1000Z was used for the Vickers hardness test at a load of 9.8N and 15s dwell time.

Microstructure analysis revealed that the grain size decreased gradually in the HAZ, dendrites are preserved at the top and bottom of the fusion zone while columnar grains are developed in the middle of the fusion zone. Delta phase precipitates increased in grain boundaries after heat treatment leading to a reduction of strengthening gamma phases thereby leading to a fall in the hardness of the weld center. In general, the hardness at the top of the weld was higher than that at the bottom. High-temperature tensile tests revealed that the tensile strength was best at the bottom of the weld (1200MPa) and worst at the top (1100MPa). The strength of the weld for the whole joint was 1100 MPa. Elongation at fracture also increased from the top (9%) to bottom (18%). This was due to the brittle fracture surface of the weld at the top. The elongation of the whole joint was 17%.

The EBW was successfully utilized to join 12.7mm-thick rolled IN718 plates (Patel et al., 2020). Weld area and penetration depth increased with an increase in heat input. However, root keyhole defects were observed at a high heat input power of 3250W. Samples welded at low heat inputs exhibited higher tensile strength that exceeded base material specification (837MPa) and fractured outside the weld with

typical elongation of 57% while those samples that welded at a higher heat input fractured at the welds.

2.4.3. Pore or void formation mechanisms in Electron Beam Welds

A study conducted on the electron beam welds of 6.5mm thick rolled CP-titanium attributed the presence of voids and pores to three major factors: instability of the keyholes in the partial penetration welds, dissolved and trapped gases, and solidification shrinkage (Huang, 2011; Kar et al., 2019). The welding parameters were set as 175kV beam voltage, 80mA beam current, 25mm/s beam speed, and 10^{-8} mbar vacuum pressure. Due to intense evaporation of metal caused by EBW, a high “recoil pressure” is built up around the electron beam leading the molten metal to flow around the beam. As the beam moves forward, the molten metal attempts to fill the gap left by the beam. However, due to the increasing surface roughness and the resulting resistance to the flow of molten metal during solidification, molten metal is unable to fill the void at the weld-bottom leading to the formation of weld root voids. The bubbles of dissolved gases or vaporized metal try to rise and escape from the pool of molten metal with the buoyancy. However, the metal needs to be in the molten state for enough time to develop sufficient buoyancy required for the bubble to rise and escape the weld surface. In the case of electron beam welding, the fast cooling rates associated with high welding beam speed and narrow weld area prevented the escape of the gas bubbles leading to the formation of spherical pores in the weld zone. Small pores are also seen on the fusion zone boundary present there due to the poor flow of molten metal over the gases trapped on the solid walls at the fusion zone boundaries. The irregular-shaped voids are formed

due to shrinkage caused by the difference in the volume of liquid and solid phases during the solidification of molten metal.

An EBW study on eight different materials, indicated the formation of defects such as porosity, unmelted lumps, spiking, and cold shut (Arata et al., 1973). The rolled materials experimented in this research included three types of austenitic stainless steel (SUS27, SUS27N, 30Cr-16NiN) consisting of 0.2% Nitrogen content, two types of carbon steel (SM41 and S35C), two types of aluminum (1200Al and 5083 alloy), and Titanium TP28. The 30mm-thick plates of each of these materials were welded in an upslope welding position with an inclination of $\pm 30^\circ$. The electron beam voltage was set as 150kV, the beam current was varied between 10-40mA, the welding speed was varied between 30-240c.p.m., and the work chamber was set in 4×10^{-4} torr vacuum. Figure 2.7 shows various defects that can be formed in electron beam welds.

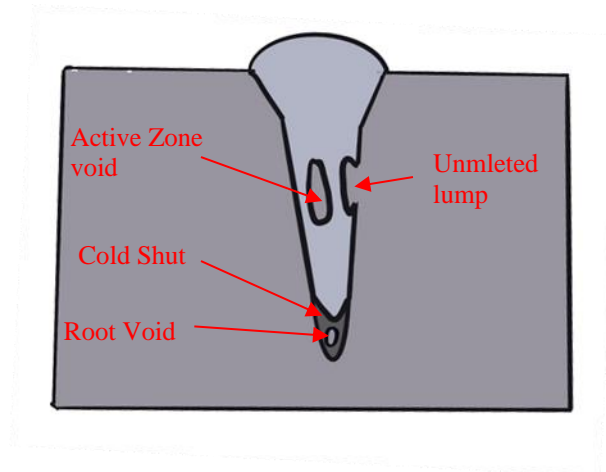


Figure 2.7 Schematic of EBW and various defects (Adapted from Arata et al., 1973)

The root voids were observed towards the tip of the penetration due to the entrapment of gases. It was reported that the formation of root voids depended on the

chemical composition of each material. The concentration of nitrogen in the material defined the formation of these root voids in the case of austenitic stainless steel. In the case of carbon steel, these defects increased with an increase in the percentage of oxygen in the material. However, in the case of titanium which also contains oxygen, such voids were not observed. In the case of aluminum alloy, the presence of a high vapor pressure element – Magnesium influenced the formation of root voids. No influence of weld penetration depth was observed on the formation of these root voids.

The active porosity formed in the vicinity of the beam travel path due to the action of the beam active zone or the beam zone around the focal point. These defects were formed in the steels but not in aluminum and titanium. The presence of oxygen and nitrogen influenced the formation of these pores. It was also found that the active porosity was directly proportional to the beam current, power, and density. Long chains of porosity on the top of the weld surface also called arcing porosity were formed due to arcing in the electron gun and the formation of weld vapors during the welding process. Thus, it was a common find in the aluminum alloy weld due to the presence of high vapor pressure magnesium in its composition. Other defects like unmelted lumps were also seen in steel welds.

In the case of the AZ series magnesium alloy, it was observed that the porosity in the weld zone was dependent on the aluminum content in the alloy (Chi et al., 2008). The delta precipitates of aluminum oxide present in the alloy dissolved due to the heat of electron beam welding. This led to the release of oxygen gas forming bubbles in the weld fusion zone and got trapped due to the fast cooling of molten metal. In the case of

EBW of rolled Inconel 718 alloy, the partial penetration welds indicated root void defects due to the entrapment of vaporized metal which could not be filled by the molten metal due to early isolation of the weld tip as the electron beam moved forward.

2.4.4. Joining of SLM'ed IN718

Varestraint test was performed on the SLM'ed IN718 parts welded by the Tungsten Arc Welding process in one research to identify the cracking susceptibility of SLM as printed and HIPed alloy (Raza et al., 2018). The SLM'ed samples were 100mm x 50mm x 3.4mm thick. The samples were subjected to the HIP at 1160°C/105MPa/3h. The top of the HIP'ed samples was machined to remove any oxide layer which made them 3.3mm thick. Wrought samples of dimension 150mm x 60mm x 3.2mm were also welded for comparison with SLM'ed samples. The SLM'ed samples were welded parallel to building direction with parameters of 70 A current, 1mm/s speed, and arc length of 2mm. The welded samples were polished to 3microns and etched using oxalic acid. The crack length was analyzed using a stereomicroscope and the microstructure of the weld was analyzed using SEM and EDS.

The varestraint test results indicated that the cracking was highest in the HIP'ed SLM samples. The total crack length increased steeply from 2mm at 0.8% strain to 11mm at 2.8% strain and remained constant until a strain of 4.1%. In case of the as-built SLM samples total crack length increased from 0mm at 0.8% to 8mm at 2.8% and remained constant until the strain of 4.2%. This was associated with the formation of a large grain structure after exposure to high temperatures during HIP. The larger grain

boundaries have more stress concentration which leads to crack initiation. The as-printed SLM sample had similar cracking as that of wrought IN718 samples.

Other research investigated the joining of SLM'ed IN718 by the brazing method (Xia et al., 2018). SLM IN718 sample was prepared from gas atomized alloy powder of 45-65 micron size with 350W laser power, 700mm/s scanning speed, 0.06mm layer thickness, and 0.1mm hatch distance. SLM'ed samples were etched using a solution of HCl, CH₃CH₂OH, and CuCl₂ to study the microstructure of the as-printed sample. SLM'ed block was cut into smaller blocks of size 20mm x 20mm x 4mm for brazing. BNi-2 filler metal foil of thickness 60 microns and 20mm x 6mm dimension was prepared. The SLM'ed sample was polished to rid of any oxide layers. The samples were clamped with a 50kPa pressure with filler metal foil squeezed between two SLM blocks. The arrangement was then brazed in a vacuum furnace at 6×10^{-3} Pa and 1060°C for 30min. The brazed samples were then cut to the dimension of 40mm x 3 mm x 4mm and then ground, polished, and etched for 30 seconds. These samples were then tested for their microhardness and microstructure. 40mm x 6mm x 5mm brazed joints were subjected to room temperature shear loads at a rate of 0.5mm/min to measure their mechanical properties.

Microstructure analysis revealed the formation of an Isothermally Solidified Zone (ISZ) surrounded by Diffusion Affected Zone (DAZ). ISZ EDS revealed the presence of the gamma phase of Ni dissolved in large quantities of Cr, Fe, and Si. DAZ contained brittle precipitates like Ni(Cr), FeNi₃, CrB₂, and Ni₃Si. The hardness test revealed a fall in the hardness at the boundaries of DAZ with the base metal and ISZ.

DAZ indicated a high fluctuation in hardness readings while the hardness in the ISZ was more constant. The shear test revealed the strength of the brazed joint to be 802MPa which fractured in mixed brittle (DAZ) – ductile (ISZ) nature. This shear value was about 77% of the base metal.

2.5. Joining of other SLM'ed metals

Electron Beam Welding was explored to join SLM components made of Aluminum alloy AlSi10Mg (Nahmany et al., 2015). Weld geometry and microstructure were analyzed for the welded parts. 10mm diameter bars were vertically SLMed using AlSi10Mg powder of size 7-50microns. The samples were welded circumferentially and perpendicular to the building direction. The SLM'ed samples were compared against cast A356-T6 specimen. EBW was performed using Westgate machine with parameters: Power ranging from 120W to 600W and heat inputs ranging 21 – 58 J/mm. This was achieved by varying beam current from 6mA to 16mA and travel speed from 240mm/min to 1000 mm/min with a constant voltage of 60kV. Welded samples were characterized as transverse and planar cross-sections. Samples were polished to 0.5microns and etched in Flick's Reagent for microstructure exposure. Welds were analyzed under an optical microscope and SEM. Microhardness tests were conducted on MMT-7 tester at a load of 100g.

Microstructure analysis of the SLM'ed base metal revealed the presence of defects at locations where melting pools overlapped. Minimal HAZ was observed around EBW of SLM'ed parts. EBW heat input had a strong influence on the overall geometry of the weld whereas welding speed affected the penetration depth of the weld.

Higher welding speeds led to deeper weld penetration but also produced a large number of pores in the weld as compared to slower welding speeds. Further, the use of lower speeds at high heat input was found to produce higher porosity in weld metal than what was present in the base metal, hence this combination of welding parameters was not recommended for welding of SLM'ed parts. Beam current also influenced the weld penetration, with deeper penetration with increasing current. Weld area increased from 0.15 mm² at 250mm/min to 2.4mm² at 1000mm/min travel speed. The penetration depth linearly increased from 1.5mm at 21J/mm to 2.75mm at 36J/mm heat input at a constant speed of 1000mm/min. The penetration depth linearly increased from 0.4mm at 22J/mm to 0.6mm at 30J/mm heat input at a constant speed of 500mm/min. Hardness tests indicated that weld metal had a slightly lower hardness of 103HV as compared to the base metal 111HV.

Laser welding was explored to join SLM'ed titanium alloy Ti-6Al-4V in another research (Yu et al., 2018). 5mm thick titanium alloy plates were SLM'ed using 300W laser power, 1000mm/s scanning speed, hatch spacing of 0.12mm, and a layer thickness of 40microns in an argon environment. SLM'ed parts were then stress relieved at 500°C/2h/furnace cooling (#4). Wrought plates of the same alloy were also fabricated for comparison. A various set of welding parameters was used for welding SLM-SLM and SLM-Wrought parts. SLM-SLM welded samples were heat-treated at 850°C/2h/furnace cooling (#3) while others were stress-relieved at 500°C/2h/furnace cooling (#1). SLM-Wrought samples were also stress relieved (#2). Tensile samples were fabricated from the welded plates as per the ASTM E8 standard and tested on a 100kN load tester.

Microhardness was measured at a load of 1.96N and dwell time of the 20s. The microstructure was analyzed using an optical microscope and SEM equipped with EDS.

All the samples showed full penetration welds except for samples welded with parameter (4kW, 2.5m/min, 0mm beam focus) as this had the lowest heat input at the highest welding speed. All the welded samples were free from cracks, but some porosity was observed in all the samples. Sample welded at (4kW, 1m/min, 0mm beam focus) has the least porosity. Minimal weld width was attained for samples welded with (4kW, 1m/min, 0mm beam focus). Overall, (4kW, 1m/min, 0mm beam focus) sample proved to be the optimal welding parameters for SLM-SLM samples and the same was used to weld SLM-Wrought samples. The hardness of the weld zone of samples #1 and #2 was equivalent to the SLM base metal but was higher than the wrought counterpart. HAZ had a relatively lower hardness as compared to the weld zone. After heat treatment, a reduction in hardness was observed in all the locations. All welded samples broke at the weld zone with almost the same tensile and yield strengths. The mechanical properties of all-welded samples were higher than the wrought specimen. The properties slightly deteriorated after heat treatment.

Other research explored Laser-Arc Hybrid welding to join the SLM'ed stainless steel 316L parts to their wrought counterparts (Casalino et al., 2013). A hybrid welding system was produced by running Laser weld and GTAW (TIG) arc torch in the opposite direction on the SLM'ed samples.

SLM parts were produced using Stainless Steel 316L powder with SLM parameters: 100W laser power, 30 μ m layer thickness, and scanning speed of 200mm/s.

The samples were welded in two configurations: (a) Laser leading followed by GTAW and (b) GTAW leading followed by laser welding. Three set of welding parameters were used for each combination giving a sum total of six different experimentation samples. The samples were tested for their microhardness at 200g indentation load and tensile properties.

Microhardness tests at the top of the weld revealed lower hardness of the fusion zone as compared to wrought steel in Laser leading configuration and the opposite was observed for GTAW leading configuration. The hardness dipped at the weld center for all the samples. SLM'ed base metal had the highest hardness as compared to wrought samples or fusion zone for all the configurations. This was associated with higher thermal gradients in the SLM parts developed during their manufacturing process. Tensile tests revealed the weld strength of welded samples (600MPa) to be on par with the wrought samples (580MPa). But the welded samples had lower elongation (~2.5mm) as compared to the wrought samples (~5.72mm).

Friction welding was explored to join SLM'ed aluminum alloy parts in another research (Prashanth et al., 2014). 12mm diameter and 60mm long samples were SLMed using Al-12Si powder with SLM parameters: 1455 mm/s scanning speed, 320W power, 50 μ m layer thickness, and 110 μ m hatch spacing. The welding surface was machined to rid of oxide layers. Friction welding was performed with a pressure of 75Mpa, upset pressure of 100MPa, burn-off length of 3mm, and a spindle speed of 1000rpm. Welded samples were analyzed for their microstructure using SEM and optical microscope. The Vickers hardness test was performed with a load of 0.1N and 10s dwell time. Room

temperature tensile test was carried out on ASTM E8 based cylindrical samples fabricated from welded specimens and at a rate of 0.0001 per sec. The results were compared with cast samples fabricated from the same material.

The hardness of the SLM'ed weld zone (~80HV) was measured to be lower than the base metal (~95HV). The opposite trend was observed for cast parts. The hardness of the cast weld zone (~70HV) was measured to be higher than the base metal (~56HV). Higher hardness for SLM base metal was due to saturated Al precipitates. The weld matrix had homogenously distributed Si and Al making it less brittle as compared to the base metal. Table 2.4 summarizes the tensile properties of the tested samples. Welded SLM samples had higher ductility and strength as compared to welded cast samples. Although the strength was less as compared to as-printed SLM parts.

Table 2.4 Tensile properties of the friction welded samples (Adapted from Prashanth et al., 2014)

	Ultimate Strength (MPa)	Elongation (%)
SLM as-prepared	380	2.75
SLM welded	305	9
Cast as-prepared	200	9.5
Cast welded	150	2

EBW has shown promising results for welding of rolled IN718 and other SLM'ed parts. The HIP has shown promising results in reducing the porosity of SLM'ed parts but also deteriorates the mechanical properties slightly. No published information was found that established EBW of SLM'ed IN718. Thus, an effort has been made as a

part of this research to test SLM'ed IN718 samples welded by EBW in HIP'ed and as-printed conditions and compare the results with the rolled IN718 samples and ASTM F3044-14a standard.

3. EXPERIMENTS

The experiment was conducted in three stages. First, the samples were built using SLM, and then EBW'ed using nine different heat inputs. For the second stage, samples built and welded using the same parameters as stage one were exposed to HIP (The as-printed welded samples will also be referred to as SLM+EBW and the HIP'ed welded samples will be referred to as SLM+HIP+EBW in this document). Finally, both the sets of samples were tested for their mechanical properties, hardness, and microstructure, and the results were compared with their rolled counterparts and ASTM specifications. Experimentation and research on the rolled samples were conducted in parallel in another study (Patel et al., 2020). Figure 3.1. shows the entire experimental process.

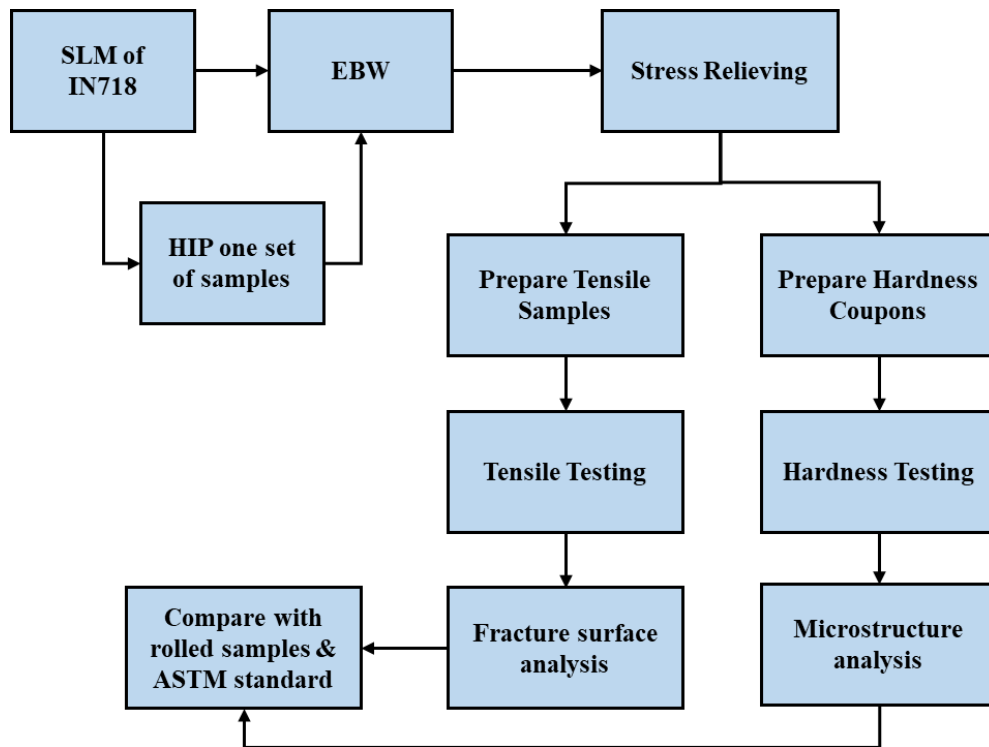


Figure 3.1 Flow chart of the experimentation process

3.1. Equipment and software:

The following equipment were used during research to perform tasks necessary for the experiments:

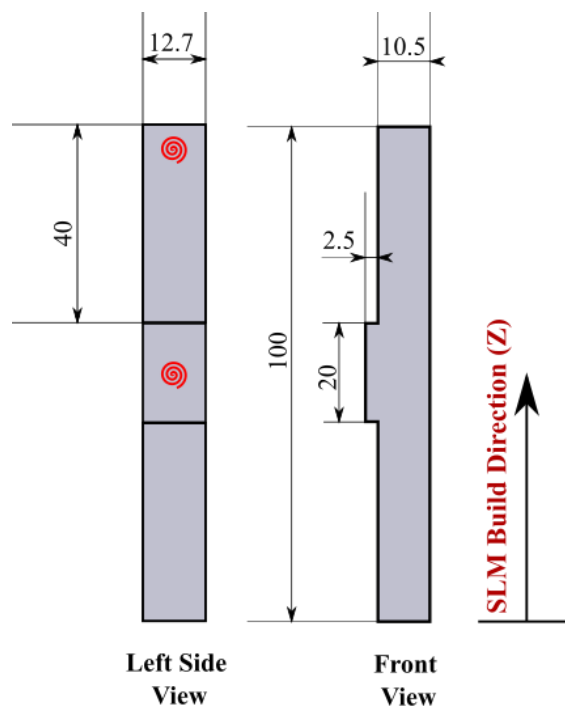
1. Renishaw AM400 SLM Machine
2. Sciaky EBW System
3. Struers CitoPress -15
4. Struers AbraPol -20
5. Dremel Hand Polisher
6. Wen Electric Engraver
7. Struers Metason 200 ultrasonic polisher
8. MTS 810 Material Testing System
9. Olympus STM6 optical microscope
10. Wilson VH1202 Vickers Hardness Tester
11. Vega 3 Tescan Scanning Electron Microscope
12. Oxford Instruments x-act Energy Dispersive Spectroscopy system

The following software were used during research to perform tasks necessary for the experiments:

1. MATLAB R2018a
2. Olympus cellSens
3. MTS Station Manager

3.2. Selective laser melting of Inconel 718

The experimentation samples were produced such that they can be machined to meet ASTM E8 tensile test standards. Further, the experiments were to be performed such that the samples are tested to prove their strengths in the worst-case scenario. In the case of SLM'ed samples, the strength is the worst in the building direction due to the lacking coherency between adjacent layers. Thus, SLM samples were built such that the build direction was along the loading direction for tensile tests. Refer Figure 3.2 for the schematic of the SLM sample and the building scheme. Each sample was labeled at two locations as shown.




- Notes:
1. All Dimensions are in mm
 2.  Location for label

Figure 3.2 Schematic of sample to be produced using SLM and corresponding SLM build direction.

In total, 40 SLM samples were built using the Renishaw AM400 machine. The machine has four different laser beams that can operate simultaneously. The samples were labeled as 1A to 20A and 1B to 20B. The placement of these forty samples on the SLM bed was as shown in Figure 3.3. The samples 1A to 5A and 1B to 5B were built using laser #1, samples 6A to 10A and 6B to 10B were built using laser #4, samples 11A to 15A and 11B to 15B were built using laser #2, and samples 16A to 20A and 16B to 20B were built using laser #3. SLM parameters are shown in Table 3.1.

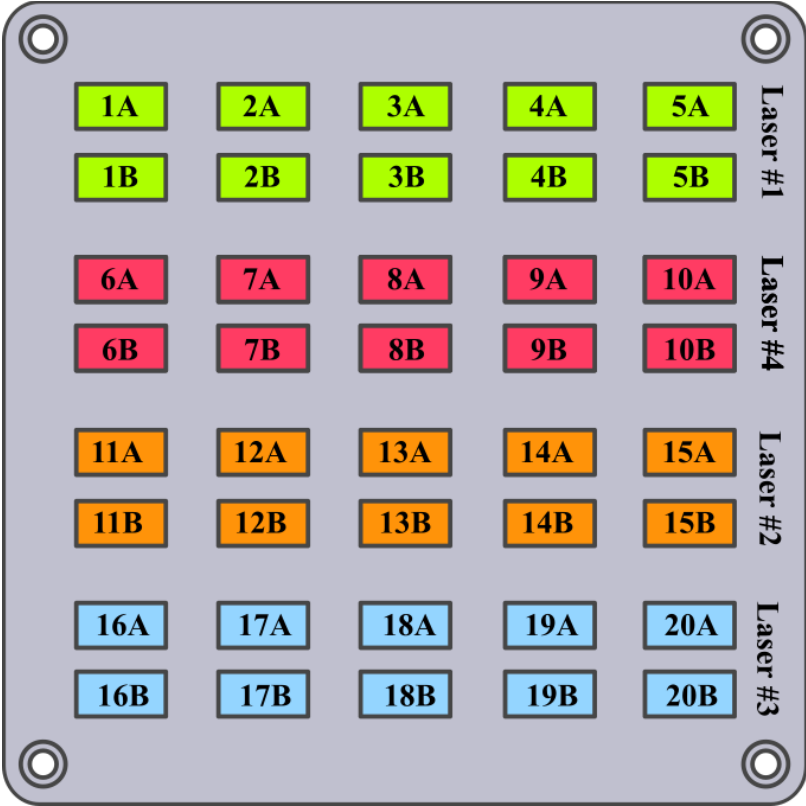


Figure 3.3 Building arrangement of SLM samples on the SLM machine base and respective laser assignment

Table 3.1 SLM parameters

Parameter	Value
Laser Power (W)	275
Scanning Speed (m/s)	0.786
Scanning Pattern	Stripe
Hatching Distance (microns)	110
Layer Height (microns)	60

Gas Atomized IN 718 powder of average particle size 50 μ m was used for SLM.

The composition is as shown in Table 3.2.

Table 3.2 Chemical composition (wt%) of IN718 powder (Luvak Laboratories, n.d.) and ASM specification (Adapted from Voort, 1991)

	Powder used for experiments	ASM specification
Ni	51.99	50-55
Cr	18.58	17-21
Fe	19.73	~17
Nb	5.17	4.75-5.5
Mo	3.02	2.8-3.3
Ti	0.99	0.65-1.15
Al	0.49	0.2-0.8
C	0.024	<0.8
Co	0.14	<1.0
Cu	0.12	<0.3
Si	0.073	<0.35
Mg	0.074	<0.35

3.3. Hot Isostatic Pressing

The effect of hot isostatic pressing was also to be observed as a part of the experiments. The HIP is a method used to reduce the porosity of a component. For the experiments, SLM'ed samples 1A to 10A and 1B to 10B were subjected to HIP with parameters as shown in Table 3.3.

Table 3.3 HIP parameters

Parameter	Value
Gas	Argon
Temperature [°C (°F)]	1163 (2125)
Pressure [MPa (ksi)]	103 (15)
Time (hrs)	4

3.4. Defining welding variables

To completely define an electron beam welding process, several parameters need to be defined. The major contributing parameters are as follows:

1. Electron Beam Voltage
2. Electron Beam Current
3. Electron Beam Speed
4. Electron Beam Focus location
5. Vacuum level and gas used

Experiments were conducted with three levels of the following variables:

1. Electron Beam Current
2. Electron Beam Speed

Electron Beam Heat input was the dependent variable given by:

$$\text{Heat Input} \left(\frac{J}{mm} \right) = \frac{\text{Beam Current (mA)} \times \text{Beam voltage (mV)}}{\text{Welding speed} \left(\frac{mm}{s} \right)} \quad (1)$$

All other EBW parameters were set constant. They are as shown in Table 3.4.

Table 3.5 depicts the combination of variables explored for the experiments.

Table 3.4 EBW parameters set as constants for the experiment

Parameter	Value
Electron Beam Voltage (kV)	50
Electron Beam Focus location	On the surface of the sample
Vacuum level (μTorr)	22

Table 3.5 Welding variables explored in the experiments

SLM + HIP + EBW sample label	SLM + EBW sample label	Beam Current (mA)	Welding Speed (mm/min)	Heat Input (J/mm)
1A, 1B	11A, 11B	65	660.4	295.3
2A, 2B	12A, 12B	60	660.4	272.6
3A, 3B	13A, 13B	55	660.4	249.8
4A, 4B	14A, 14B	65	787.4	247.6
5A, 5B	15A, 15B	60	787.4	228.6
6A, 6B	16A, 16B	55	787.4	209.6
7A, 7B	17A, 17B	65	914.4	213.2
8A, 8B	18A, 18B	60	914.4	196.8
9A, 9B	19A, 19B	55	914.4	180.4
10A, 10B	20A, 20B	Unwelded Sample		

3.5. Electron beam welding

All SLM'ed samples were welded using electron beam welding at their respective parameters as shown in Table 3.5. Eighteen samples 1A/B to 9A/B were arranged as shown in Figure 3.4 on the EBW machine bed. Each sample was separated using spacers. This was done to prevent adhesion of adjacent samples post welding. Change in EBW parameters for each set of samples was programmed in the computer control of the EBW machine. This allowed the welding of all eighteen samples in one pass. The same process was repeated for samples 11A/B to 19A/B.

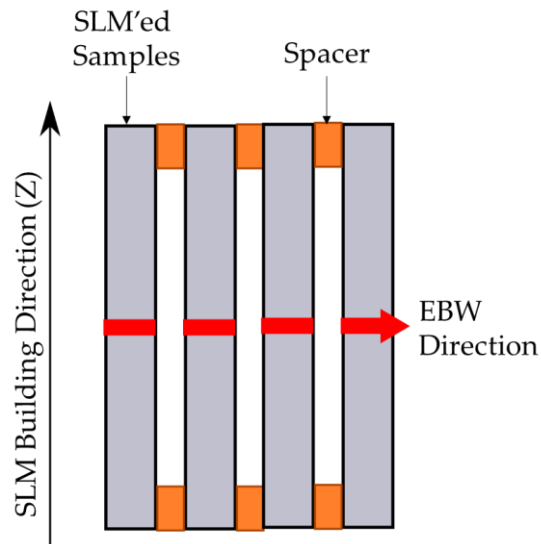


Figure 3.4 Schematic of the setup for the EBW process

3.6. Stress relieving

All the samples were stress-relieved at parameters shown in Table 3.6.

Table 3.6 Stress-relieving parameters

Parameter	Value
Temperature (°C)	970
Time (hr)	1

3.7. Hardness sample preparation

Using wire electrical discharge machining, coupons were cut off from each sample for hardness testing. The schematic of wire-EDM of the sample is shown in Figure 3.5.

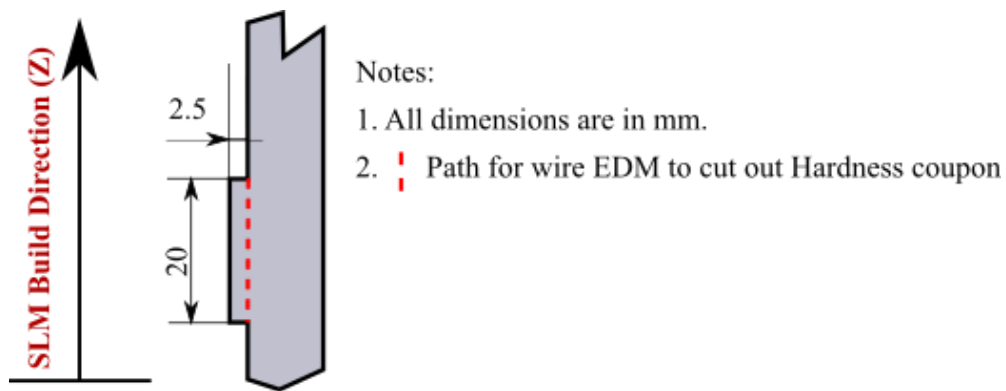


Figure 3.5 Schematic for Wire-EDM of hardness coupons

The hardness coupons were to be molded in an epoxy mold to provide better grip when performing hardness tests. As a means of identification, a coding system was developed to distinguish each sample based on its EBW parameters. Samples were cut as per their respective codes using hand files and hack saws before molding. The sample names and their respective arrangements have been shown in Table 3.7.

Table 3.7 Labeling scheme for hardness samples

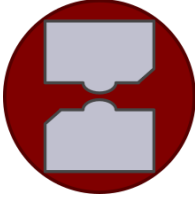
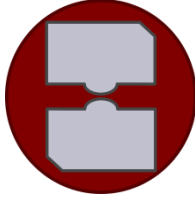
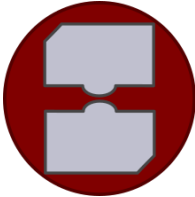
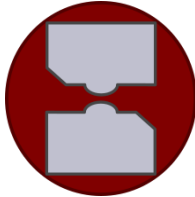
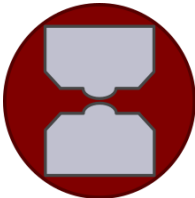
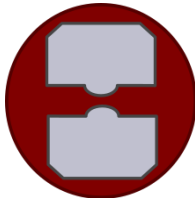
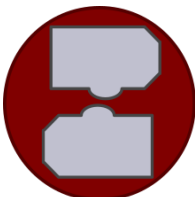
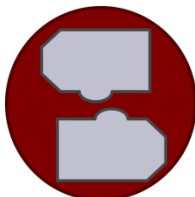
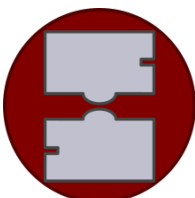
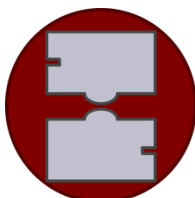
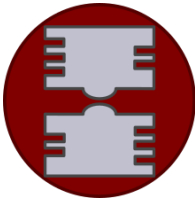
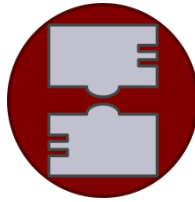
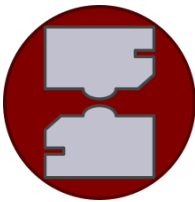
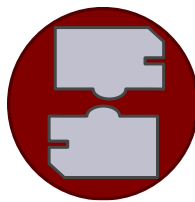
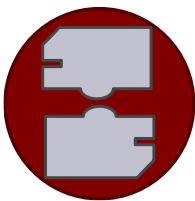
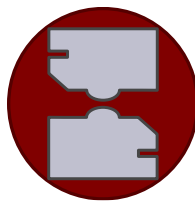
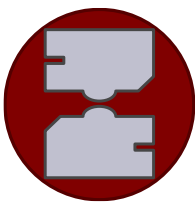
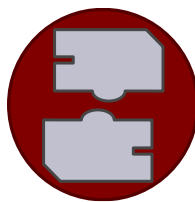
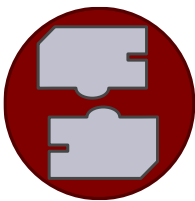
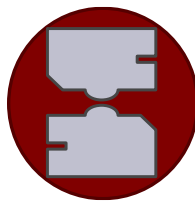
Sample label	Sample arrangement	Sample label	Sample arrangement
1A/1B		2A/2B	
3A/3B		4A/4B	
5A/5B		6A/6B	
7A/7B		8A/8B	
9A/9B		10A/10B	

Table 3.7 Continued

Sample label	Sample arrangement	Sample label	Sample arrangement
11A/11B		12A/12B	
13A/13B		14A/14B	
15A/15B		16A/16B	
17A/17B		18A/18B	
19A/19B		20A/20B	

3.7.1. Molding

As defined in the coding scheme, two hardness coupons were molded on one puck. Figure 3.6 shows a typical molded sample. Molding was performed on the Struers CitoPress-15 machine shown in Figure 3.7 (A).



Figure 3.6 Molded hardness coupons

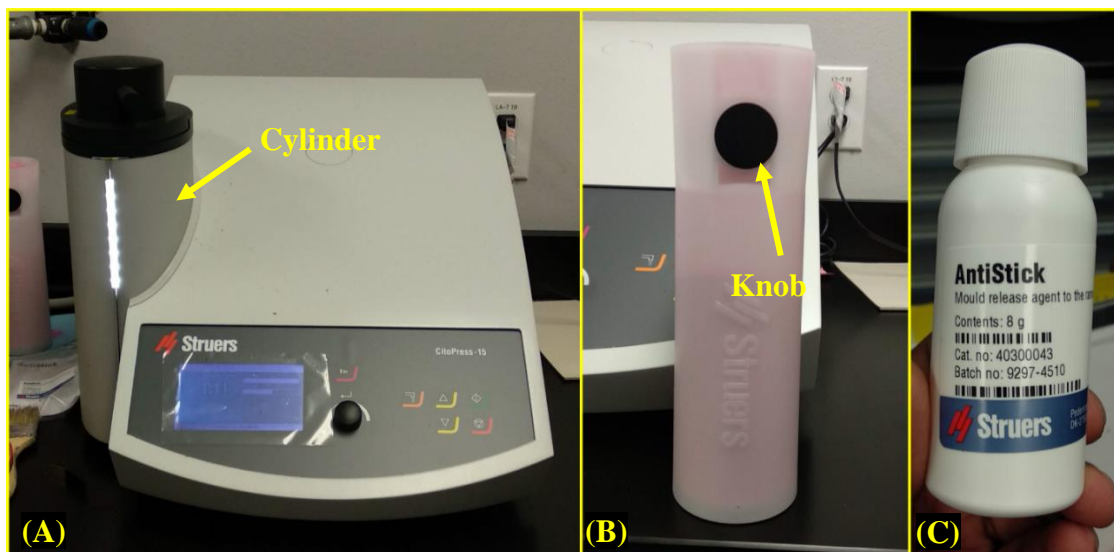


Figure 3.7 (A) CitoPress-15 molding machine; (B) Powder dispenser; (C) AntiStick powder

The molding procedure is as follows:

1. The machine is switched on. Program set for 'Multi-fast RED' powder is preset. The program defines pressing time and temperature for the powder in use.
2. The cap on the top of the cylinder is screwed open.
3. Using the yellow UP arrow key on the buttons panel, the ram inside the cylinder is raised.
4. Using a brush, residues and dirt particles are cleaned off from the surface of the ram. AntiStick powder is applied on the ram surface and the inner surface of the cylinder cap.
5. Hardness coupons are placed on the ram as shown in Table 3.7.
6. Ram is lowered by pressing the yellow DOWN arrow key on the buttons panel.
7. Using the powder dispenser shown in Figure 3.7(B), the cylinder is filled with the RED powder. The knob on the dispenser is turned seven times to dispense enough powder (40ml) required to get appropriate thickness on the molded puck.
8. The cylinder cap is screwed close.
9. Ram is raised using a yellow UP arrow key on the buttons panel and the pressing operation is started by pressing the green START button.
10. The typical pressing operation takes 7 minutes for completion. The machine beeps after the pressing operation is complete.
11. The cylinder cap is screwed open and the ram is raised using the yellow UP arrow key.
12. The molded puck is removed from the cylinder for further processing.

3.7.2. Grinding

Having a smooth and polished surface on the hardness sample is necessary to avoid erroneous test readings. Further, it provides better results when observing under a microscope. Grinding of molded pucks was done using the Struers AbraPol-20 machine as shown in Figure 3.8(B).

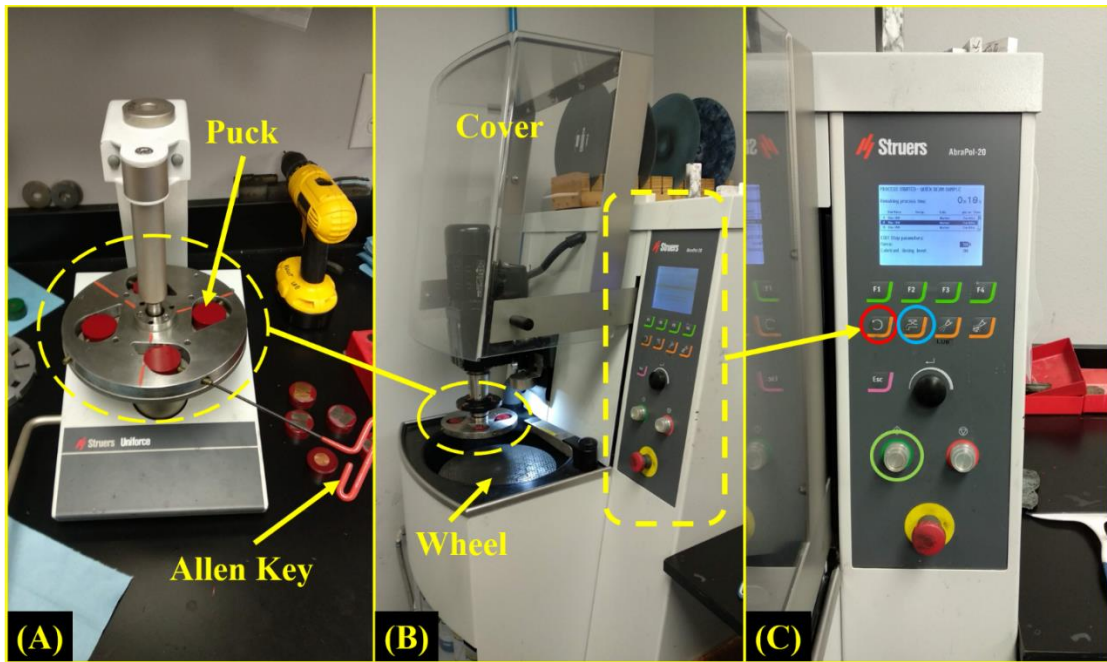


Figure 3.8 (A) Struers Uniforce grinding fixture; (B) Struers AbraPol-20 grinding and polishing machine; (C) Control Panel

The process followed for grinding operation is as follows:

1. Four pucks are fixed face down on the Struers Uniforce fixture using an Allen key as shown in Figure 3.8 (A).
2. Struers AbraPol-20 shown in Figure 3.8 (B), a semi-automatic grinding machine, is switched on.

3. Grinding is performed in 7 steps using different grinding wheels or machine parameters. The machine is programmed accordingly. The details are as shown in Table 3.8.

Table 3.8 Grinding Steps

# Step	Grinding Wheel*	Time (mins)	Fixture Downward Force (N)	Wheel Upward Force (N)	Speed (rpm)
i	Emery - 80	3	50	50	50
ii	Emery - 80	2	130	50	120
iii	Emery - 80	1	50	50	50
iv	Piano MD - 80	2.5	50	50	50
v	Piano MD - 220	1	50	50	50
vi	Piano MD - 500	1	50	50	50
vii	Piano MD - 1200	2	50	50	50

*Roughness of grinding wheels decrease down each type

4. The machine cover is opened. The fixture with four pucks is placed in the appropriate holder and a sound fit is ensured.
5. The appropriate grinding wheel as depicted in Table 3.8 and as shown in Figure 3.9 (A) is placed on the wheelbase shown in Figure 3.8 (B).
6. A dry run of the wheel is initiated using the revolve button marked red in Figure 3.8 (C) on the machine control panel. The water (lubricant) supply is turned on using the button marked blue in Figure 3.8 (C).

7. For grinding steps iv to vii, a sandstone block is shown in Figure 3.9 (B) is used to sharpen the wheel surface.
8. Grinding operation is initiated using the green knob. The machine runs the set step and stops after the set time for each step.
9. The fixture is removed, and grind quality is checked. After inspection, the fixture is placed back into its position.
10. The black knob is rotated clockwise to move to the next grinding step and the process is repeated from point 5.
11. Once all the steps are complete and the required finish is obtained, the pucks are disengaged from the fixture using Uniforce and the Allen key.

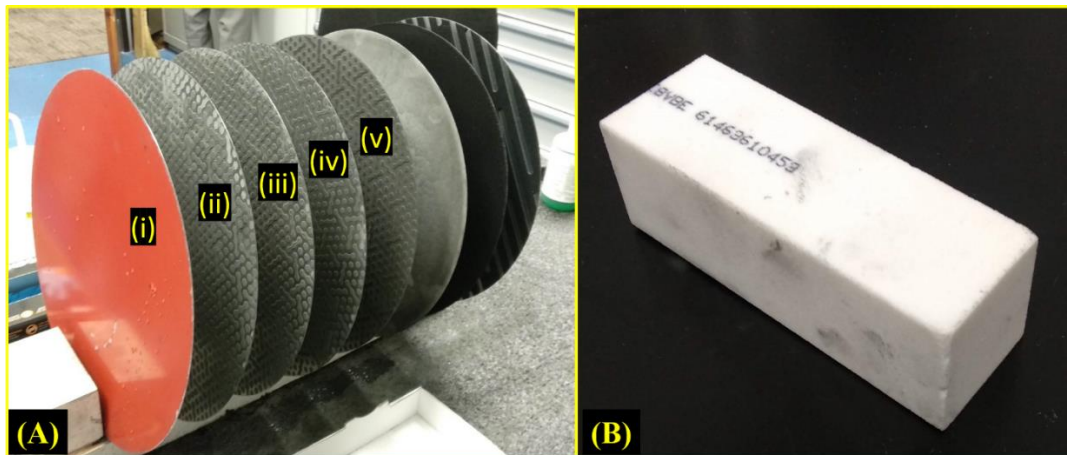


Figure 3.9 (A) Grinding Wheels: (i) Emery - 80, (ii) Piano MD – 80, (iii) Piano MD – 220, (iv) Piano MD – 500, (v) Piano MD – 1200; (B) Sandstone block

3.7.3. Polishing

The ground pucks were further polished to achieve a smooth surface. Polishing was performed using Dremel 3000 hand polisher with three types of diamond polishing

pastes in the following order: 7/5 microns, 1 micron, and 0.5 microns. Refer Figure 3.10 for polishing equipment used.

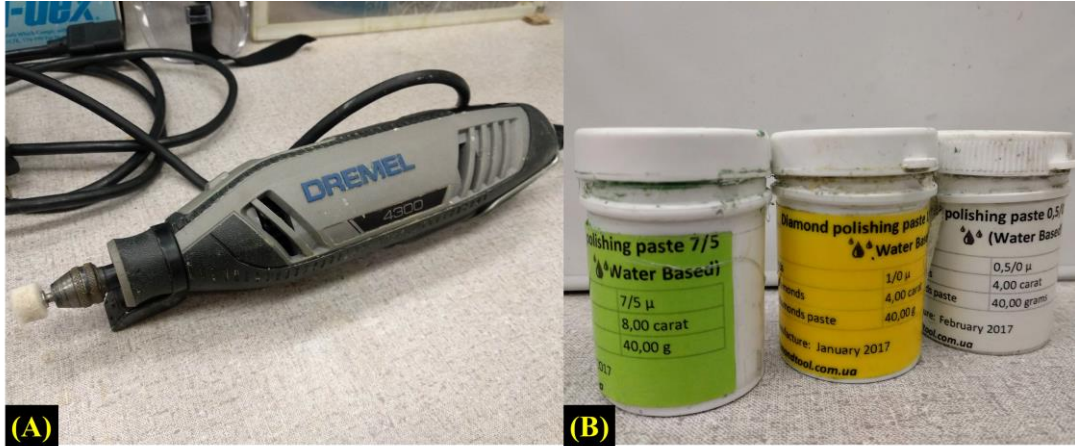


Figure 3.10 (A) Dremel 4300 hand polisher; (B) Diamond polishing pastes

The sample surface was cleaned thoroughly using Q-Tips followed by ultrasonic cleaning in isopropyl alcohol for 120sec before switching to a different polishing paste to get rid of remnant particles on the polished surface. Refer Figure 3.11 for the cleaning device used.



Figure 3.11 Struers Metason 200 ultrasonic cleaner

Polished samples were stored in an airtight enclosure to prevent contamination in any form.

3.7.4. Etching

The polished surfaces were etched to enhance features such as weld geometry, surface defects such as cracks and microstructure. The etching was performed as per standard ASTM E407-07 by rubbing Aqua Regia etchant (4 HCl (33%) + 1 HNO₃ (67%)) over the surface using cotton swabs for multiple steps of varied times (15sec to 30sec) until the weld geometry and the grain boundaries were visible. After etching, the specimen surface was rinsed with isopropyl alcohol and dried using an air blower.

3.8. Tensile Sample Preparation

Tensile samples were cut from EBW'ed samples using wire-EDM as shown in Figure 3.12. The thickness was reduced to 6mm from the original 12.7mm by machining equal thickness of material from both the ends of the SLM'ed sample.

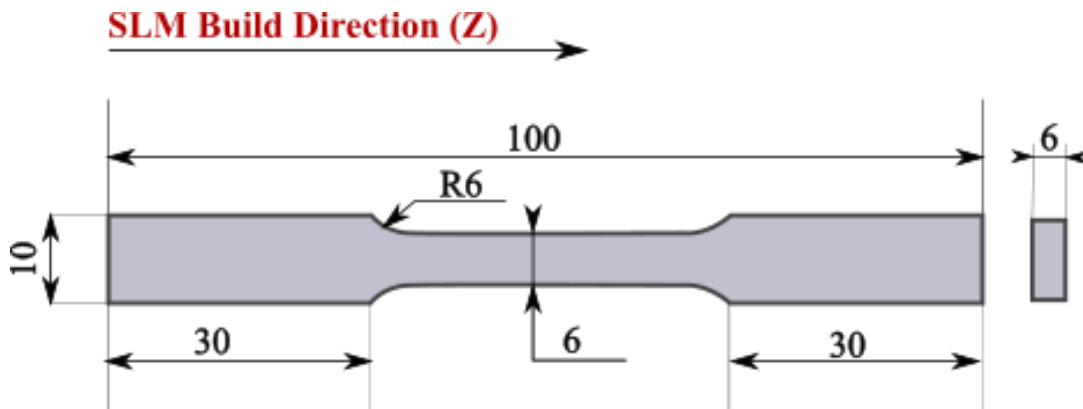


Figure 3.12 Design of tensile samples; Unit: mm

The tensile samples were prepared as per ASTM E8 Standard (Standard Test Methods for Tension Testing of Metallic Materials) subsize specimen dimensions. Wen

electric engraver was used to engrave both ends of each specimen with its sample name on the side as shown in Figure 3.13 (C) & (D).

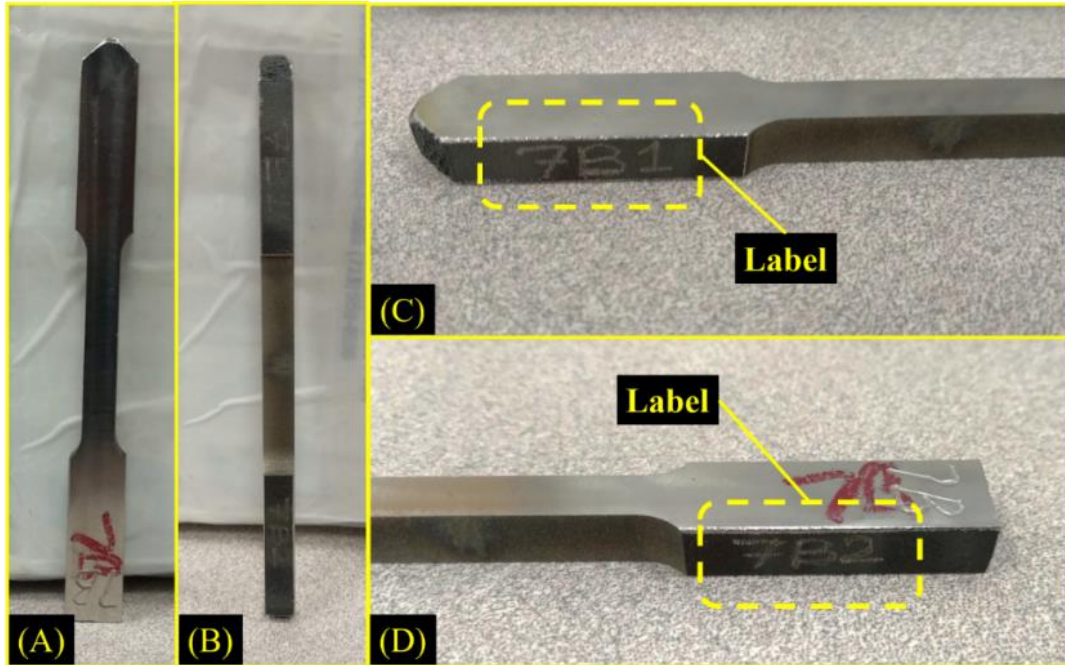


Figure 3.13 Typical tensile sample as per ASTM E8 subsize standard: (A) Front, (B) Side, (C) & (D) Label engravings on both ends of the specimen

As-built gage section area dimensions of each specimen were recorded using Vernier calipers for accurate tensile test results. Gage thickness and gage width were measured at three different levels over the gage length as shown in Figure 3.14 to consider machining error. Dimensions of the grip sections were also measured and recorded at locations B2, B1, T2, and T1 using Vernier calipers.

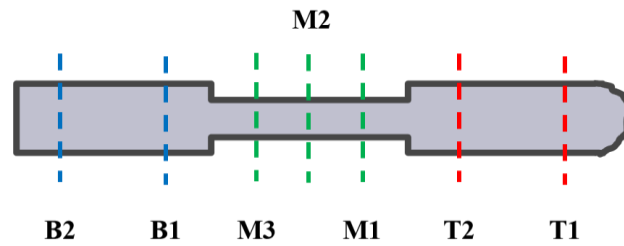


Figure 3.14 As-built measurement locations on the tensile specimen; M1, M2, M3: gage section measurements; B1, B2, T1, T2: grip section measurements

3.9. Testing

Four types of tests were conducted as a part of the experiments:

1. Microscopy to analyze the weld geometry and presence of defects such as pores, voids, and cracks in the weld zone or base metal.
2. Microhardness test to determine the hardness of the weld zone and the surrounding base metal.
3. Tensile test to determine the mechanical properties such as yield strength, ultimate tensile strength, young's modulus, toughness, and elongation at fracture to collectively determine the strength and ductility of each specimen.
4. Microstructure analysis to determine the nature of aberrant materials observed on the material surface.

3.9.1. Microscopy

Hardness coupons molded into pucks were observed under the Olympus STM6 optical microscope shown in Figure 3.15. The Olympus STM6 is a semi-automatic microscope equipped with four levels of magnification lenses: 5x, 10x, 20x, and 50x. The focal point can be adjusted by moving the lenses in the vertical direction (Z). This

can be done manually using a control panel which allows fine to coarse control over focus. The bed is equipped with dials that can be controlled manually to move the bed in two mutually perpendicular directions (X and Y) on the horizontal plane. The position monitor indicates the current position of X, Y, and Z axes with respect to the set reference point. Each axis can be set to zero at any location to find the respective axis co-ordinate of any other location with respect to the zero location. The microscope has a computer-controlled camera wherein different camera controls such as ISO, exposure, and shutter speed can be controlled using the software. The viewfinder can also be used for an optical view in a better resolution.

The process followed for microscopy of the specimen:

1. The molded puck is placed on the bed under the lens after the machine is turned on and necessary adjustments are made on the computer.
2. The lowest magnification lens i.e. 5x is equipped and the same is set on the computer software. The computer is set on live mode to view real-time imagery recorded by the microscope.
3. Using the black knob on the control panel, the focus (Z-axis) is adjusted until the image on the computer screen is clear.
4. The specimen is manually rotated such that crosshairs on the computer screen align with the horizontal and vertical edges of the specimen respectively.
5. Weld Geometry:

- a. Using the dials, the bed is moved such that the image indicates the weld top profile is on the center of the screen. The image is captured using the software.
- b. The dial is moved in the Y direction and the next part of the weld profile is captured.
- c. This process is continued until the entire profile is captured via multiple images.
- d. The images are stitched together using image processing software to obtain the complete weld geometry and can be analyzed further.

6. Defects:

- a. Using the dials, the entire specimen surface is scouted for defects at the lowest magnification (5x).
- b. In case a potential defect is spotted, the bed is fixed in that location such that the defect is positioned in the center of the computer screen.
- c. The lens is switched to higher magnification as required by the size of the defect. The same lens magnification is set on the software. The focus is adjusted using the control panel until clear imagery is seen.
- d. To ensure that the defect under question is a void, a crack, or a pore the focus is set such that a sharp image of the surrounding surface is observed. The Z-axis on the position monitor is set zero. Next, the focus is adjusted such that the center of the suspected defect is observed clearly. If the Z coordinate on the position monitor is negative, the suspected defect is indeed a void, crack,

or pore. Else, it is an external medium such as a burr or dirt particle adhered to the specimen surface. The surface shall be cleaned thoroughly and air-dried to be free of such external agents.

- e. Images of the defects are captured using the software for further analysis.

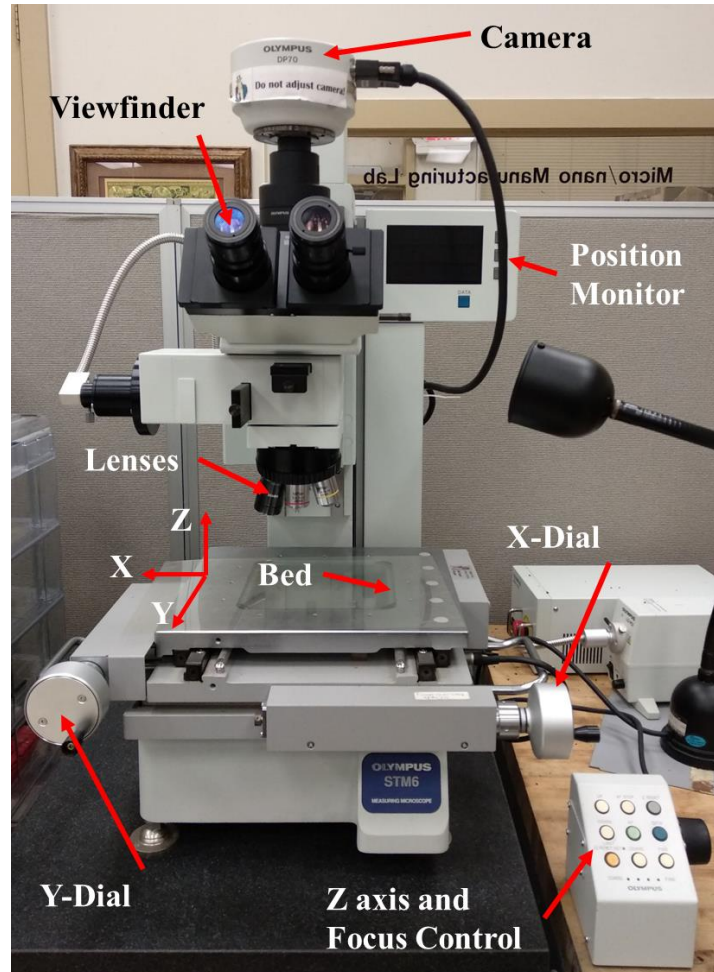


Figure 3.15 Olympus STM 6 optical microscope

3.9.2. Micro Hardness Test

The microhardness of each specimen was tested at two levels (Level A = 0.3mm and Level B = 4.8mm from the top) along with the weld depth. The horizontal distance

between two indents on each level was set to be $3d$ where d is the largest diagonal length of a typical indent on the specimen. The schematic plan for the hardness tests is as shown in Figure 3.16.

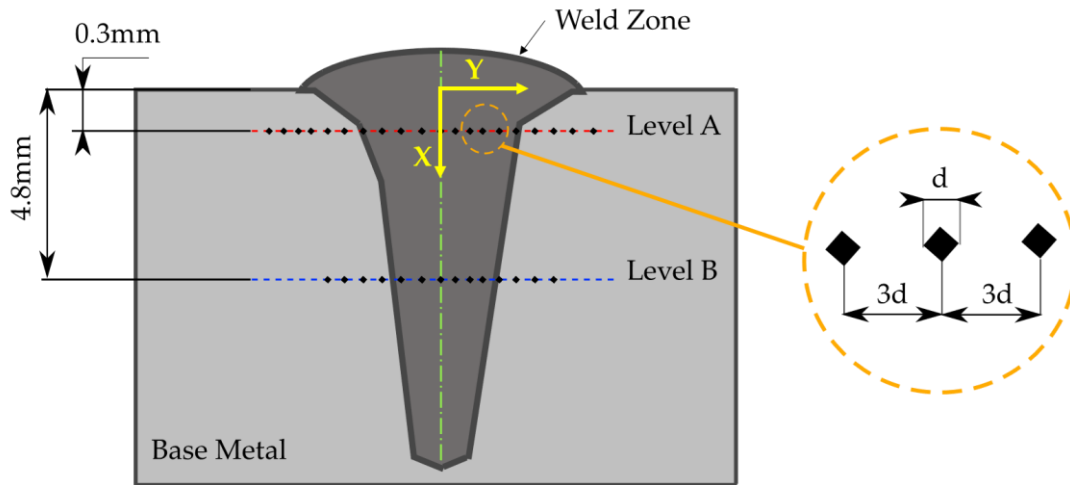


Figure 3.16 Schematic plan for hardness testing

The microhardness test was performed using the Wilson VH1202 Vickers hardness tester shown in Figure 3.17. VH1202 is a manual VH tester with lenses of three magnifications: 5x, 10x, and 50x. The bed has a fixture to hold molded pucks and is equipped with two digital micrometers to adjust the bed along X and Y axes. Z-axis and the focus can be adjusted using a dial knob on the side of the machine. A rotary viewfinder can be used to view the magnified image of the specimen surface. A digital touch screen allows setting various parameters such as Load and Dwell Time. These parameters were set as shown in Table 3.9.

Table 3.9 Hardness test parameters

Parameter	Value
Load (gf)	300
Dwell Time (sec)	15

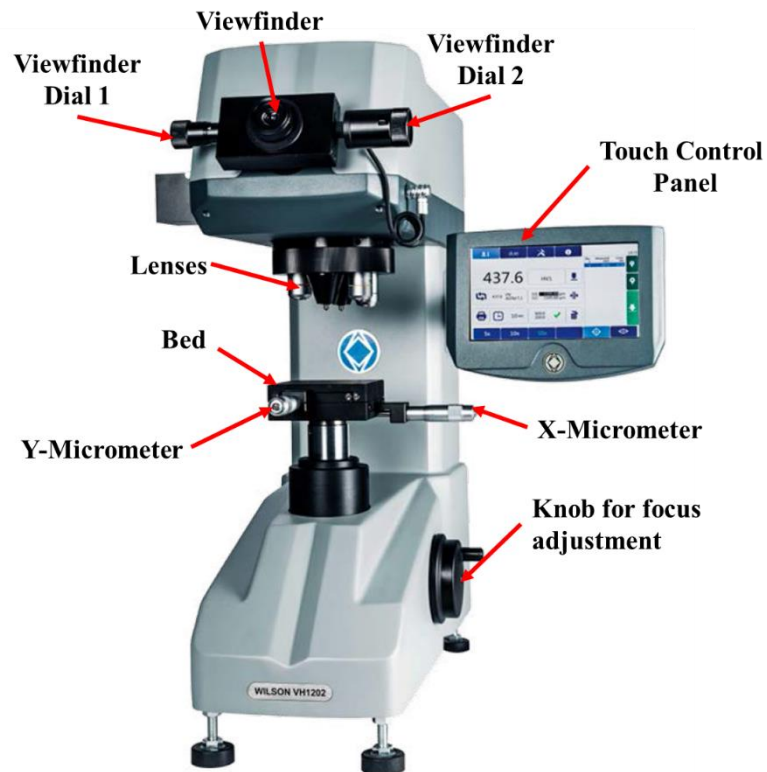


Figure 3.17 Wilson VH1202 Vickers hardness tester

The process followed for hardness testing:

1. The puck is installed in the fixture on the hardness tester bed and the machine is turned on. The parameters are set as shown in Table 3.9.

2. Using the viewfinder, and the micrometers, the specimen's horizontal and vertical edges are aligned with the beds Y- and X-axis respectively.
3. Identifying the weld center:
 - a. Using the Y micrometer, the viewfinder crosshair is first aligned to the left edge of the weld zone. The micrometer is set to zero.
 - b. The micrometer is rotated, and the crosshair is aligned with the right edge of the weld zone.
 - c. The value indicated by the micrometer is the width of the weld zone at that location. This value is halved and the micrometer is moved in the negative Y direction by that value. This is the weld center.
4. Testing on level A:
 - a. Using the X micrometer, the crosshair is aligned on the top edge of the specimen and the micrometer is set to zero.
 - b. The micrometer dial is rotated to cover 0.3mm distance along with the weld depth.
 - c. The lens is switched to 10x magnification and the focus is adjusted for clarity.
 - d. Using the control panel, the indenter is activated and allowed to indent the specimen surface.
 - e. Once the indenter retracts, the indentation is viewed under the viewfinder.
 - f. The crosshair is aligned on one of the corners of the indentation using the dial on the viewfinder. Using the other dial, the vertical line is split in two and a line is moved to the opposite corner of the indentation. The movement of the

crosshair vertical line is recorded as the indentation diagonal length on using the touchscreen control panel.

- g. The same is repeated for the other diagonal. The indicated hardness value is recorded.
 - h. To measure the hardness on the next point, the Y micrometer is rotated to move the bed by distance '3d', and steps a to g are repeated.
5. To test on level B, the same process is followed as that for level A with the only difference being the X micrometer dial distance to be 4.8mm instead of 0.3mm.
 6. The hardness measurements are plotted using data visualization software.

3.9.3. Tensile test

The tensile test was conducted on MTS 800 tensile testing machine shown in Figure 3.18 (A). The machine is hydraulically powered and has dual control (Manual + Computer). The tensile tests were conducted as per the ASTM E8 standard. Test parameters were set as shown in Table 3.10.

Table 3.10 Tensile test parameters

Parameter	Value
Test Type	Displacement Controlled
Load Cell (KN)	100
Applied Strain Rate (mm/min)	0.5
Data Acquisition frequency (Hz)	5

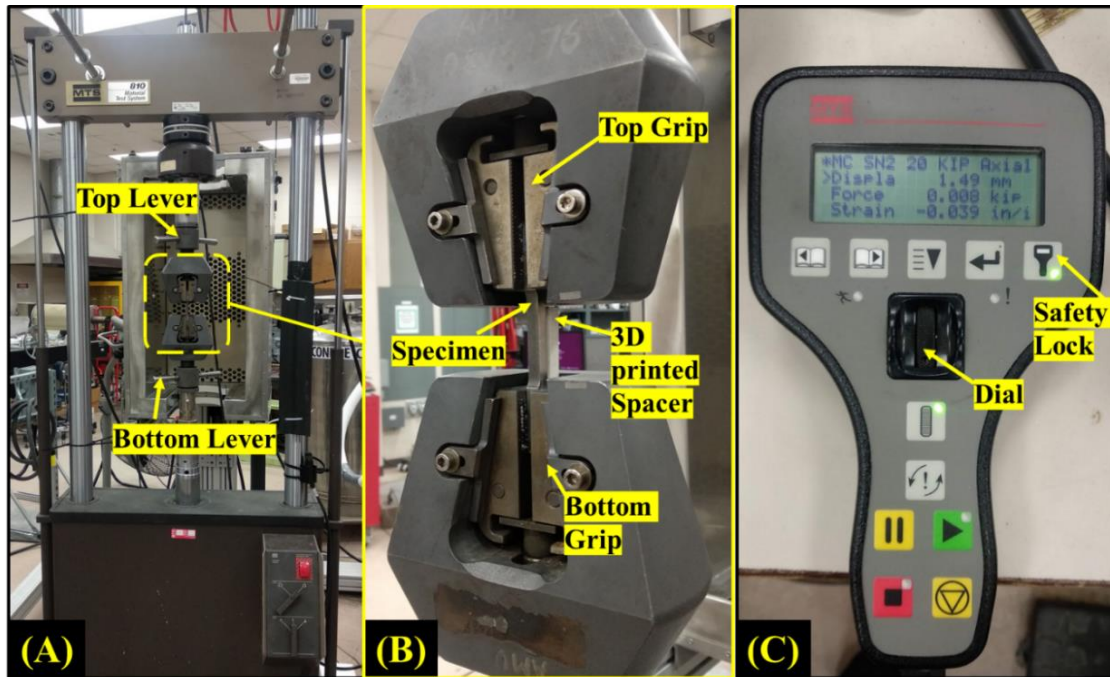


Figure 3.18 (A) MTS 810 tensile testing machine; (B) Arrangement of the tensile specimen in the crossheads; (C) Manual remote controller for crosshead movement

The following process was followed for tensile testing:

1. The machine is powered on and the hydraulic supply is turned on.
2. MTS Station Manager software is opened on the computer connected to the testing machine. A typical software screen is shown in Figure 3.18.
3. A new procedure is created in the software with parameters defined in Table 3.10. Here the procedure is named IN718.000. All the files created under this procedure will have the same parameters defined for the procedure.
4. A new specimen file is created by pressing button A shown in Figure 3.18 to record the test data of the current specimen being tested. Here the specimen is named A31R.

5. Button Interlock is pressed followed by the button with three green bars to activate the control of the testing machine via the software. These buttons can be found under the block marked with B in Figure 3.18.
6. The button marked C in Figure 3.18 is pressed to unlock the manual control of the machine. Further, the safety lock button is pressed on the remote controller shown in Figure 3.18 (C).
7. Using the dial on the manual remote controller, crossheads are moved closer to one another such that they just match the specimen length.
8. Using the lever adjacent to the respective crosshead, the grips are loosened.
9. To ensure the specimen is gripped between the crossheads vertically, a 3d printed spacer (95 x 7 x 3 mm) as shown in Figure 3.19 is placed touching the specimen and the crosshead wall. This provides a reference for the vertical gripping of the specimen. The specimen is placed between the top grips and the top lever is tightened carefully.

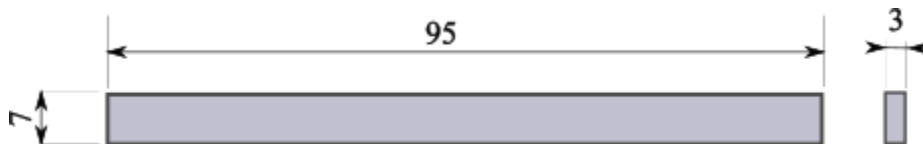


Figure 3.19 3D printed ABS plastic spacer to ensure the vertical alignment of the test sample on the tensile tester

10. Using the dial on the manual remote controller, the lower crosshead is moved up until the lower grips can properly cover the lower grip section of the specimen.
11. The lower grips are carefully tightened using the bottom lever.

12. The safety lock on the manual remote control is turned on and manual control is turned off using the button marked C on the software screen.
13. Buttons D and E marked on the software screen are pressed to activate real-time force, displacement, and time meters. The force and displacement are set to zero by pressing the button marked in Figure 3.20.
14. The play button under block marked F in Figure 3.20 is pressed to start the test.
15. The crossheads move away from each other with the strain rate defined in the procedure. When the specimen breaks, the stop button in block F is pressed to stop the crosshead displacement.
16. Manual control is turned on using the same process as in step 6 and the crossheads are moved further apart from each other using the dial on the manual controller.
17. Using respective levers, the grips are loosened to remove both the parts of the broken specimen. These parts are safely stored without disturbing the fracture surface.
18. The force-displacement-run time data for the specimen tested is saved as a .txt file by the station manager software when the file is saved. This data is further analyzed to obtain important mechanical properties of the specimen.

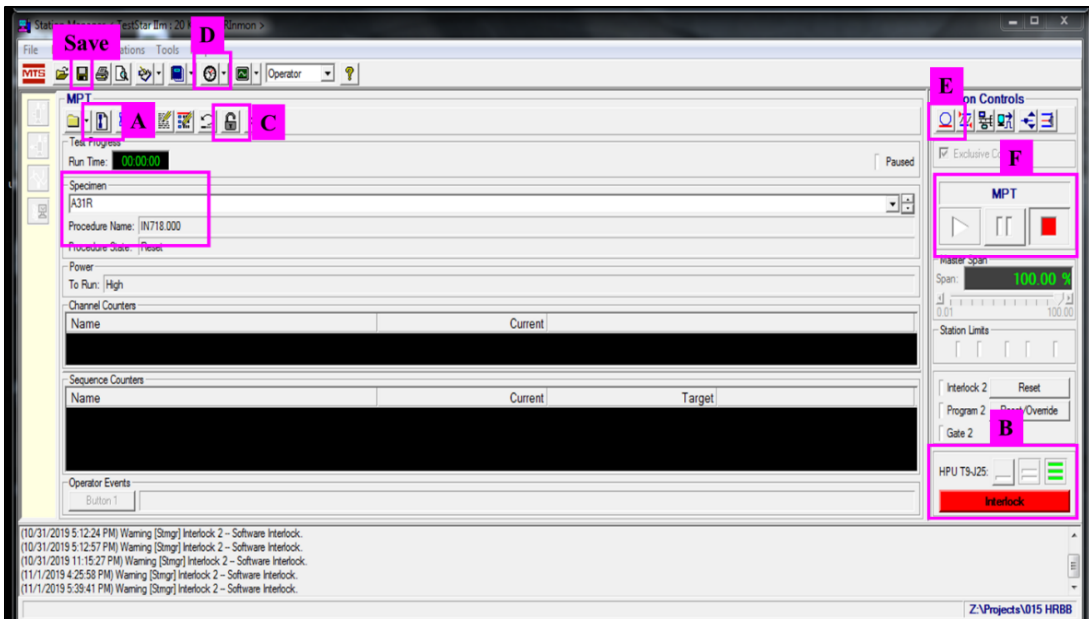


Figure 3.20 Typical screen of MTS Station Manager Software



Figure 3.21 Real-time force-displacement-run time meters on the MTS Station Manager software

3.9.4. Microstructure Analysis

Vega 3 Tescan microscope was used for SEM analysis while Oxford Instruments x-act was used for EDS as shown in Figure 3.22. The following procedure was followed for microstructural analysis:

1. Gas cylinders were turned on to provide the SEM machine with pressurized gas necessary for maintaining a vacuum inside the measuring chamber.
2. On the computer screen VegaTC software (Figure 3.23) was used to control the SEM. The vent button was pressed on the screen to vent the vacuum from the chamber.
3. The chamber door was opened and the sample is fixed appropriately on the bed using a conducting tape as shown in Figure 3.22 (B). Care shall be taken that no non-conducting substance is in contact with the sample to avoid interference in the SEM recordings.
4. Chamber is closed and the vacuum is pumped in the chamber using the pump button on the computer screen. SEM is ready for operation once the chamber pressure reaches 10^{-2} Pa.
5. The electron gun is turned on to initiate scanning by pressing the HV button and setting the initial voltage at 15kV. If the image is unclear, the voltage can be further increased as per requirement.
6. Using the carousel on the screen and the controller (Figure 3.22 (C)) surface of interest is brought under the electron beam path.

7. MAG and WD scrolls on the controller are used to adjust the vertical distance of the sample surface from the electron beam gun until the image is clear and in focus. WD is recommended to be set at 9mm for the best results. The brightness and contrast of the SEM image can be adjusted using the three buttons on the top right of the controller.
8. Once, the required site is identified, the Acquire button can be pressed to capture the image of the surface microstructure.
9. To identify the chemical composition of a site on the sample surface, the SEM is adjusted over the required site. EDS software Aztec (Figure 3.24) is used to control the EDS detector. The data acquisition settings were set as 10keV energy range, 1024 channel resolution, 4 min as process time, and 50sec live acquisition time.
10. The detector was turned on using the bottom right button highlighted in Figure 3.24. EDS has two modes: Analyzer mode – to identify the general chemical composition of a site and Point&ID mode – to identify chemical composition at a specific point in a site.
11. In Analyzer Mode – Spectrum is directly acquired using the Start Button on the software screen for the site set on the SEM screen. In Point&ID mode, the image of the site is first captured using the scan image button. Then mouse cursor can be moved over the scanned image and placed at a point where the spectrum is to be acquired.
12. Detected elements can be confirmed in the ‘Confirm Elements’ window. Spectral data and the scanned images can be saved for further analysis.

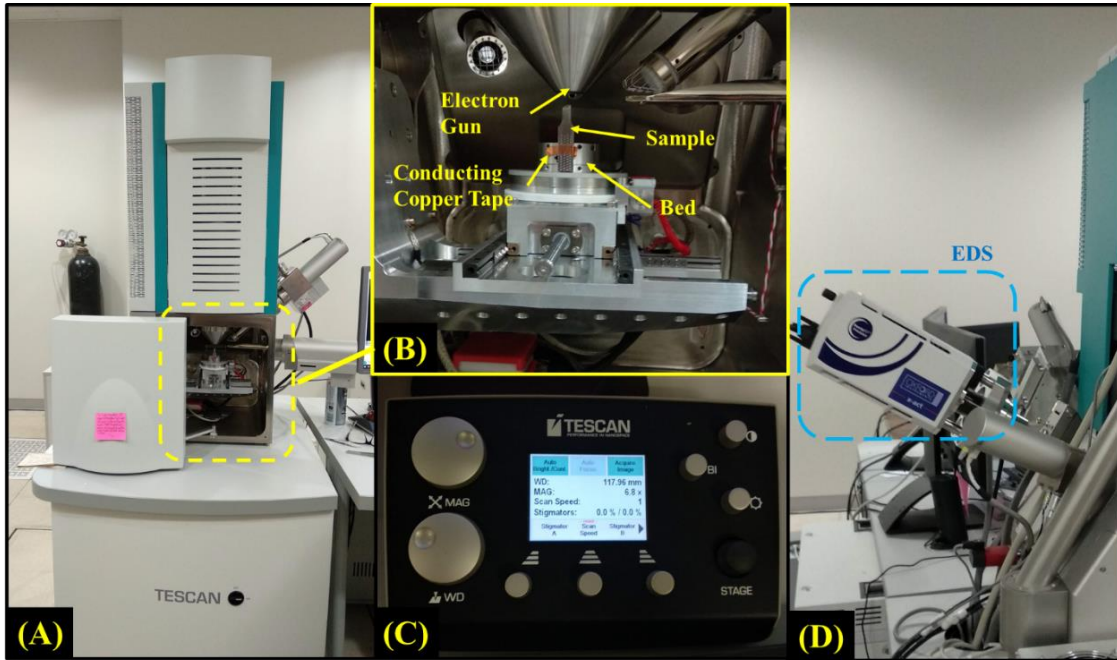


Figure 3.22 (A) Vega3 Tescan SEM; (B) Sample placement in the SEM chamber; (C) Controller; (D) Oxford Instruments x-act EDS system

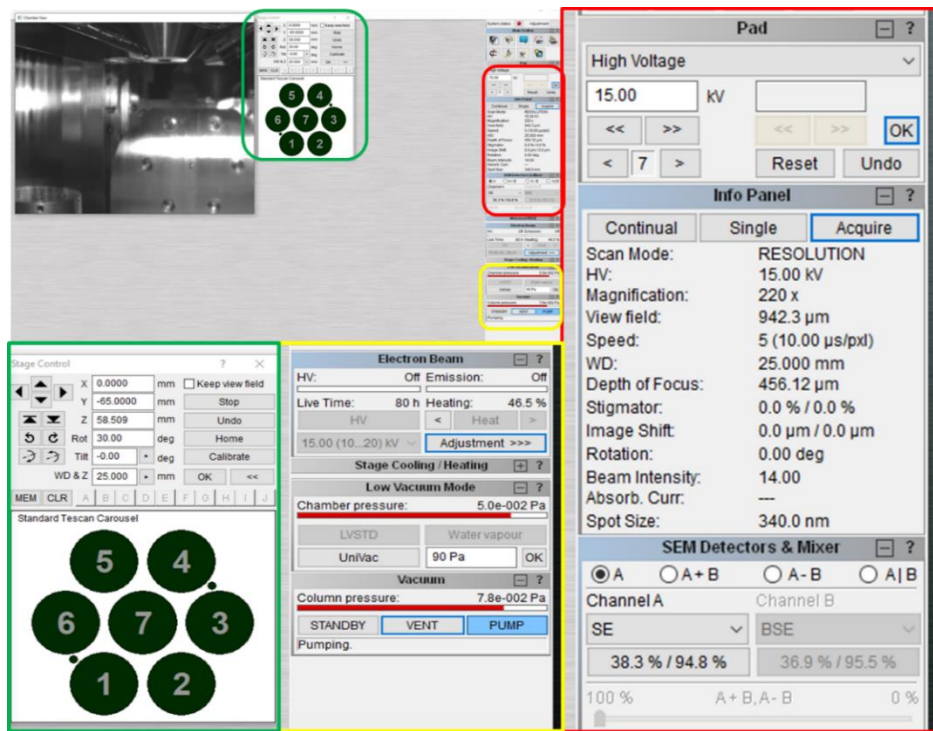


Figure 3.23 VegaTC software screen

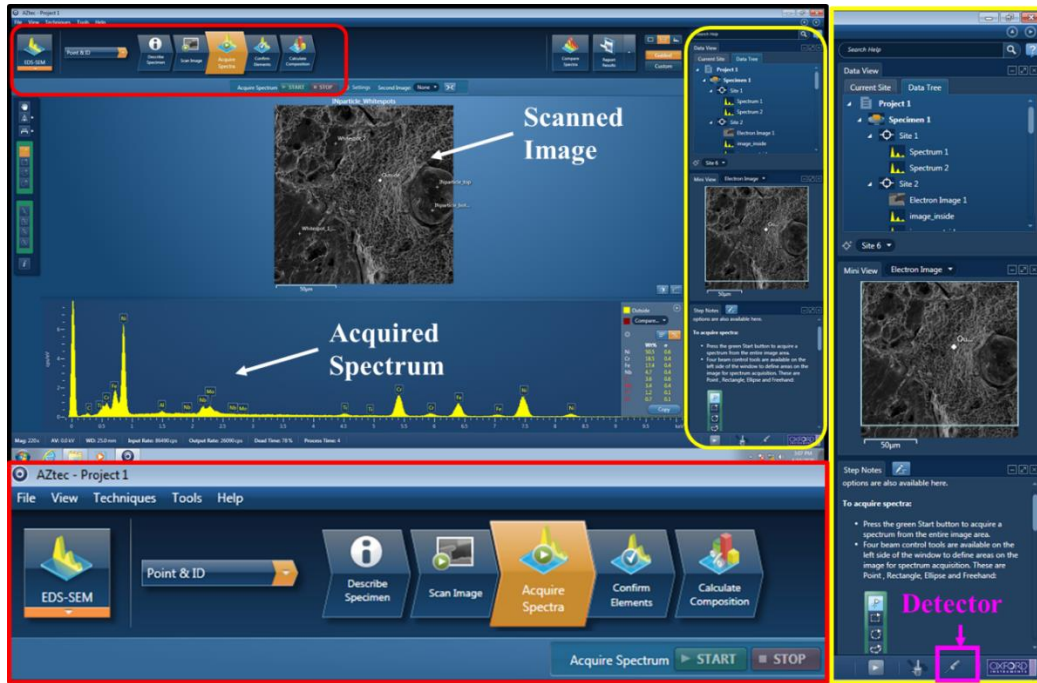


Figure 3.24 Aztec EDS software screen

4. RESULTS AND DISCUSSION

From the various tests conducted on the SLM'ed and rolled samples important results were found. Microscopy indicated the geometry of the weld and the features of the base metal surface. Mechanical strength and microhardness were established using the tensile and Vickers hardness tests. Finally, the fracture behavior of the tensile samples was explained based on the microstructure analysis of the fracture surfaces and the chemical composition at various peculiar locations on these surfaces.

4.1. Weld profile and defects

Electron beam welding penetrated very deep in the SLM metal and provided excellent weld penetration depths as seen in Figure 4.2, Figure 4.3, and Figure 4.4. The weld cross-sections had a 'nail' shaped structure. The top of the weld had a wide 'nail-head' shape which gradually reduced in width to a 'nail-tip' shape at the bottom. Longer exposure of the beam, larger effective diameter of the electron beam, and low thermal gradients led to a larger melt pool at the top led to its larger width. This nail shape was consistent within all the welded samples. Similar results were recorded for electron beam welds of the rolled IN718 published in prior literature (Agilan et al., 2014; C. A. Huang et al., 2005; Patel et al., 2020).

The as-printed SLM base metal revealed the presence of defects such as gas-filled spherical pores, and irregularly shaped voids on their surface (Figure 4.1 (a)). These defects were concentrated on the boundaries of the printed samples (Figure 4.1 (b)). These defects were suspected to be formed due to the partial melting of particles

during the SLM process, the collapse of the molten pool on the scanning surface, denudation of adjacent un-melted particles by the molten metal, quick solidification of the molten metal spattered in front of the scanning path, or entrapment of environmental gas bubbles within the molten pool during the SLM process. Similar defect formation was recorded in SLM'ed metals in previous research (Khairallah et al., 2016). There was a reduction in surface porosity on the SLM+HIP+EBW samples due to the exposure to high pressure and temperature during the HIP process. No defects were seen on the base metal of the rolled samples.

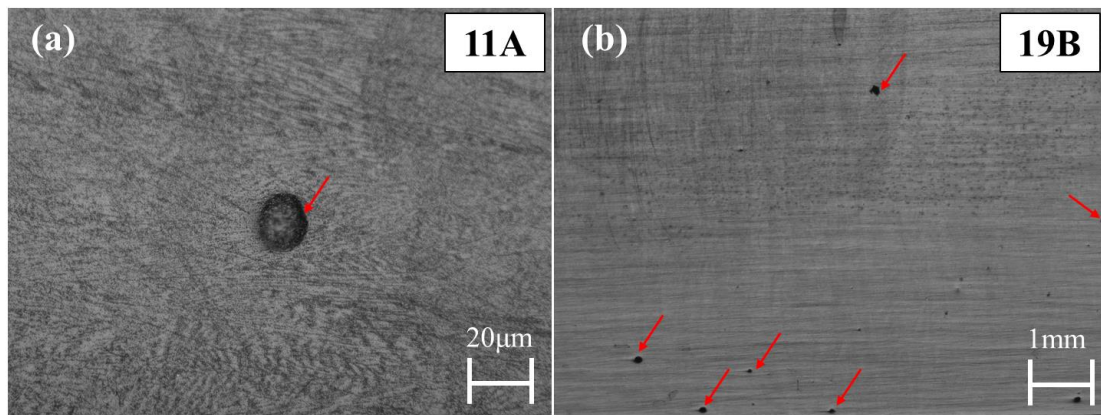


Figure 4.1 (a) Spherical pore in SLM base metal surface of sample 11A (b) Pores and voids towards the end of the SLM base metal of sample 19B

At higher heat inputs, root voids were observed at the bottom of the weld as seen in Figure 4.2 for SLM+HIP+EBW samples welded at heat inputs in the range of 295.3 J/mm to 209.6J/mm. Whereas in the case of SLM+EBW samples, these root voids were observed at heat inputs from 295.3J/mm to 249.8 J/mm as seen in Figure 4.3. In the rolled samples these defects were observed at high heat inputs and high welding speeds (247.6J/mm at 787.4mm/min, and 213.2J/mm at 914.4mm/min).

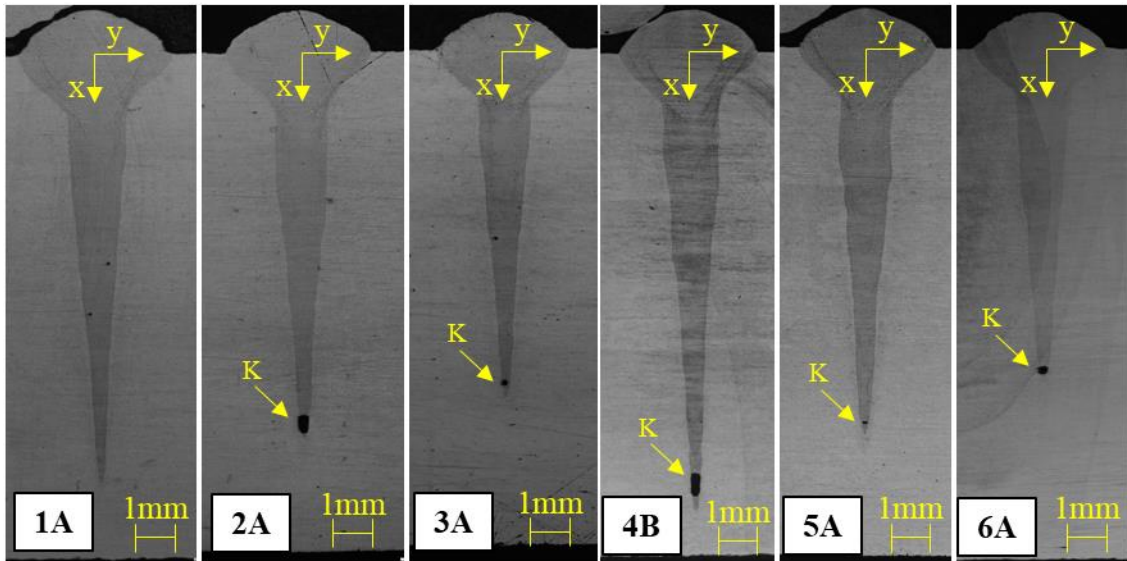


Figure 4.2 Weld geometry for SLM+HIP+EBW samples 1A - 6A; K – Keyhole root void

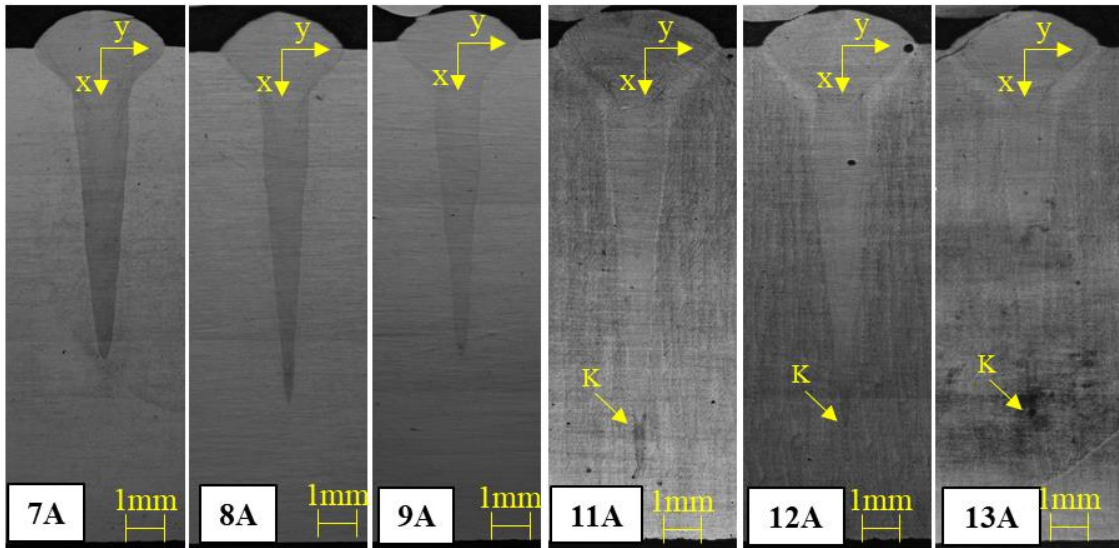


Figure 4.3 Weld Geometry for SLM+HIP+EBW samples 7A to 9A and SLM+EBW samples 11A to 13A; K – Keyhole root void

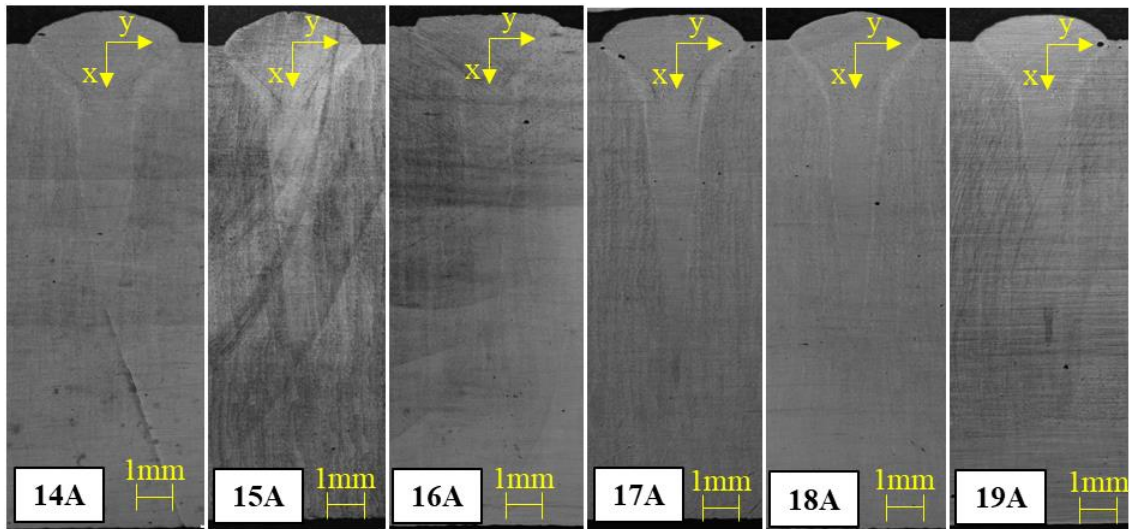


Figure 4.4 Weld geometry for SLM+EBW samples 14A to 19A.

The high energy electron beam led to the violent melting of the IN718 metal along its path and formed a crater with molten metal flowing upwards around the beam boundary. As the beam moved forward, the molten metal collapsed and solidified with a void at the weld-bottom that could not be filled owing to the fast cooling of the molten metal. Similar mechanisms were suspected in EBW of other metals in previous publications (J. Huang, 2011; Jawwad et al., 2005; Kar et al., 2019).

Voids and spherical pores were also observed at the top of the weld on the interface of the weld zone and the base metal in some SLM samples as seen in Figure 4.5. Again, due to the violent melting of the metal during the EBW process, the gases trapped in the pores or the voids of the SLM'ed base metal are released in the molten metal. Due to the heat of the molten metal, the released gases expanded or coalesced to rise towards the top of the weld. However, the molten metal solidified before the gases could escape the metal surface leading to the formation of spherical pores towards the top of the welds. A

similar mechanism was reported in EBW of previously published literature (Arata et al., 1973; Chi et al., 2008; J. Huang, 2011; Kar et al., 2019). The irregular voids seen in the weld region could be due to the solidification shrinkage of the molten metal or poor flow of molten metal in the boundaries due to high fluid viscosity and surface roughness. This was also reported in published literatures (J. Huang, 2011; Kar et al., 2019).

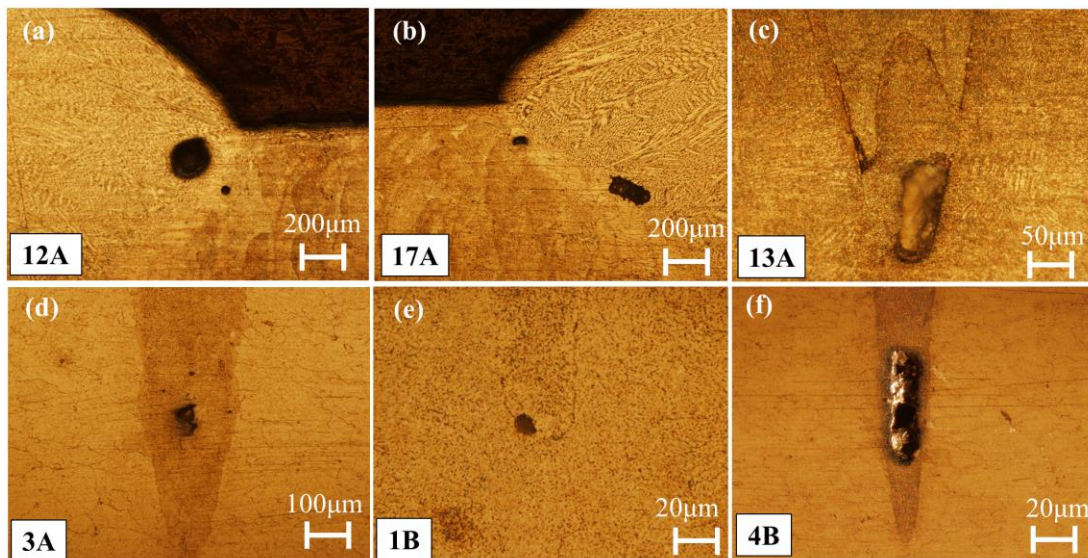


Figure 4.5. Various defects in EBW of SLM'ed samples - Voids at nail head do not repeat in twin sample of (a) SLM+EBW sample 12A (272.6 J/mm) and (b) 17A (213.2 J/mm); (c) Unmelted lump defects in SLM+EBW sample 13A (249.8 J/mm); (d) Void inside the weld of the SLM+HIP+EBW sample 3A (249.8J/mm); Root void in the weld of SLM+HIP+EBW samples (e) 1B (295.3 J/mm) and (f) 4B (247.6 J/mm)

A linear dependency of the weld penetration depth on the heat input can be observed in Figure 4.6. The overall weld area also increased with an increase in the electron beam current and a decrease in the welding speed as seen in Figure 4.7. As the beam voltage was constant at 50kV, the weld area also increased with an increase in the heat input. Slow beam speeds, high beam current, and eventually the higher heat inputs

allowed more interaction between the beam and the material, forming a larger molten volume and weld area. Penetration depth and weld area also depended on the thermal conductivity of the material. Thus, the rolled samples which were free of defects and hence had a higher conductivity showed the highest weld penetration as compared to the SLM'ed samples. SLM+EBW samples had the least penetration and weld area as their thermal conductivity was affected by the presence of gas-filled pores, voids, and metal-carbide/oxide phases in the metal matrix. An improvement is seen in SLM+HIP+EBW samples due to the closing of some of the pores due to HIP.

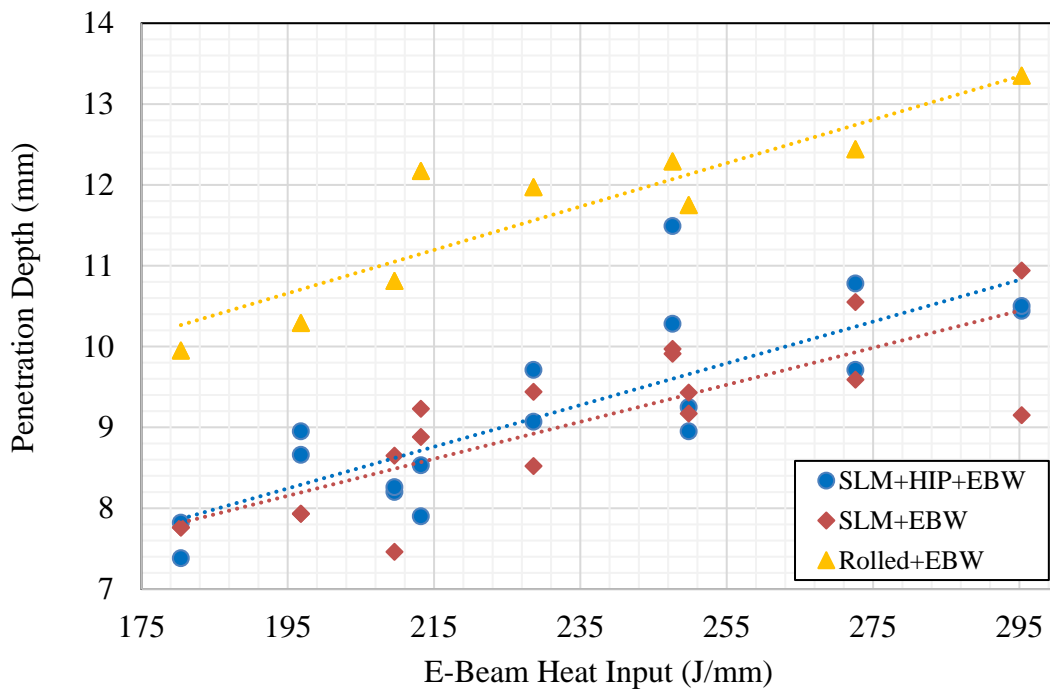


Figure 4.6 Effect of E-Beam heat input on weld penetration depths of the welded samples.

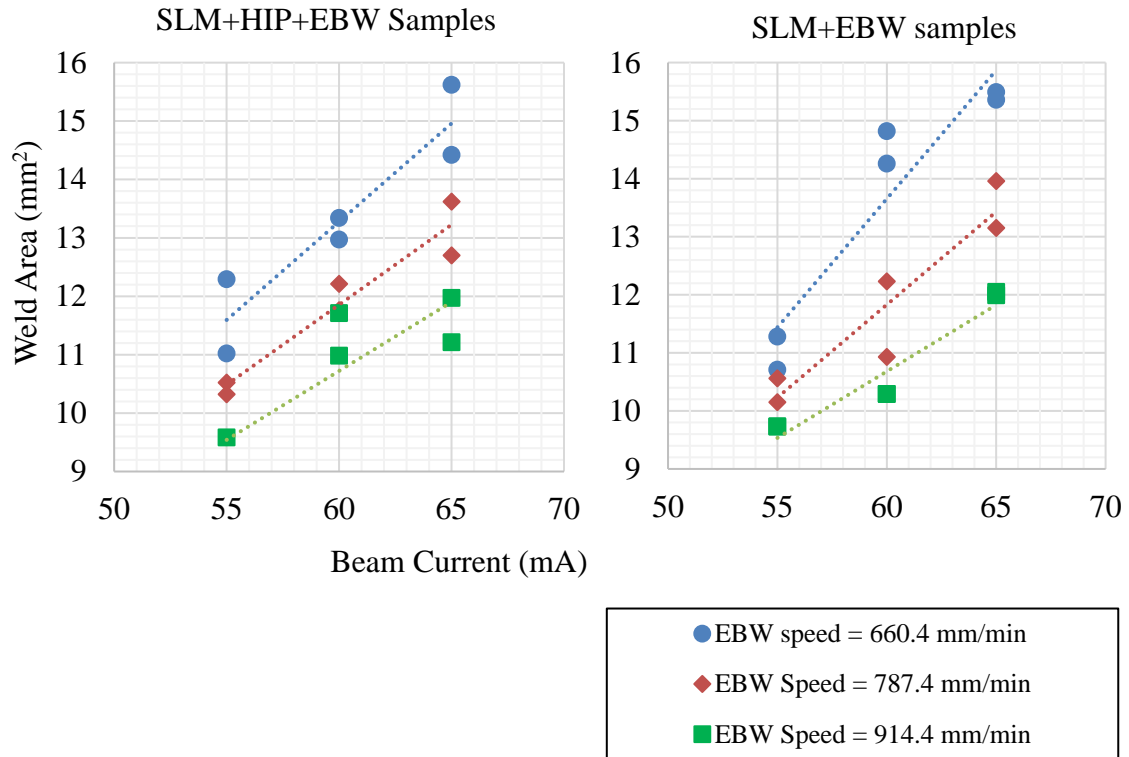


Figure 4.7 Effect of beam current of weld area for the welded SLM samples. Weld area increased with an increase in beam current and a decrease in welding speed.

4.2. Tensile properties

All the EBW samples fractured at the weld center due to the brittle nature of the welds, except SLM+EBW sample 16A (209.6 J/mm). All unwelded samples broke randomly away from the center with a 45° fracture surface. The typical stress-strain curves observed for SLM+HIP+EBW and SLM+EBW samples are shown in Figure 4.8. SLM+HIP+EBW samples were extremely brittle with poor fracture elongation and fractured even before reaching the yield point. SLM+EBW samples had a normal fracture behavior where the samples broke after entering the plastic deformation stage. All the mechanical properties extracted from the stress-strain curve of each sample are

summarized in Table 4.1 and Table 4.2. Toughness was calculated from the area under the stress-strain curve.

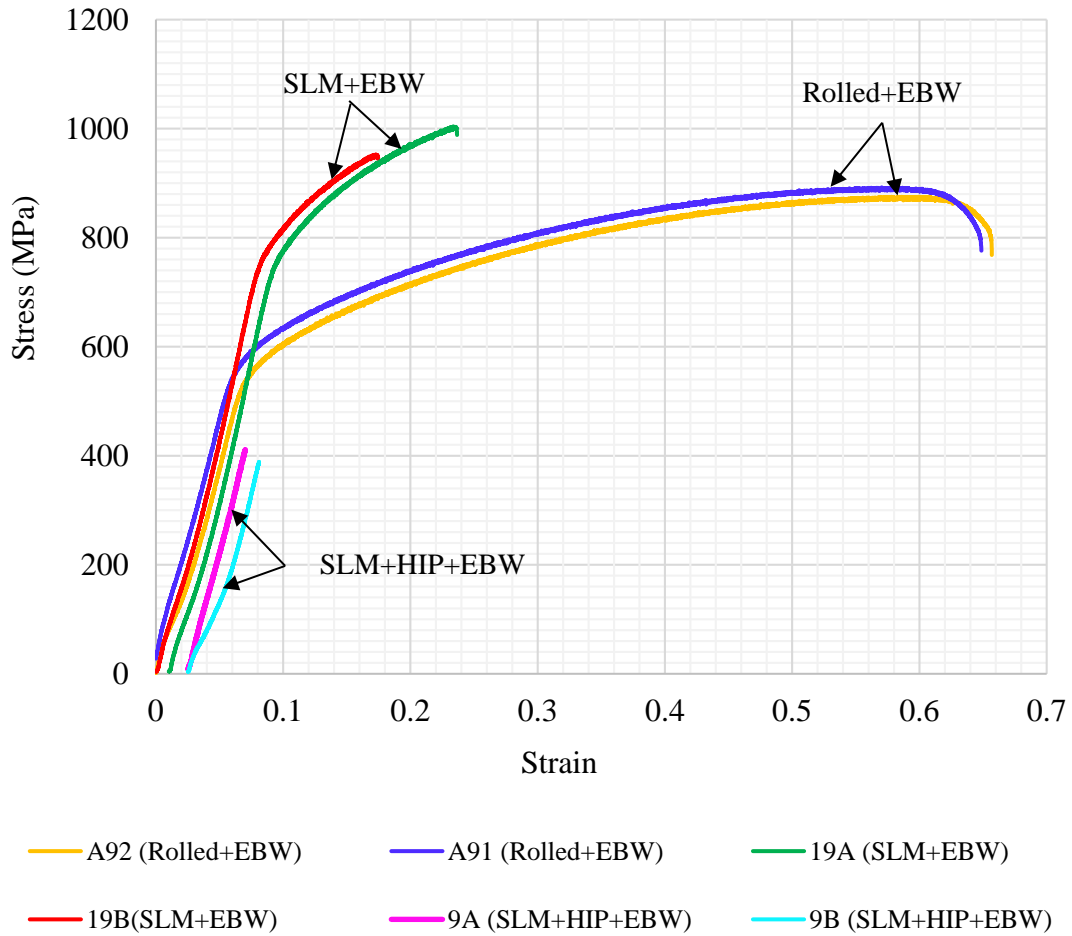


Figure 4.8 Typical Stress-Strain curve for the samples welded at a heat input of 180.4 J/mm. A91 curve is shifted by 25MPa, the 19A curve is shifted by 0.01 strain, and 9A-B curves are shifted by 0.025 strain for better visualization.

Table 4.1 Tensile properties of SLM+HIP+EBW samples

Sample Label	EBW Heat Input (J/mm)	YS (MPa)	UTS (MPa)	Young's Modulus (GPa)	Elongation at Fracture (%)	Toughness (J/mm³x10⁻³)
A/B	295.3	400, 394	400, 394	9.14, 9.47	4.53, 4.93	8.96, 9.09
2 A/B	272.6	399,327	399,327	9.50,8.74	4.65, 3.86	8.94, 6.18
3 A/B	249.8	413, 432	413, 432	9.64,9.64	4.71,5.64	9.48, 10.99
4 A/B	247.6	390, 446	390, 446	9.32, 9.73	4.71, 5.05	8.86, 10.91
5 A/B	228.6	439, 436	439, 436	9.66, 10.14	5.24, 5.76	10.79,10.94
6 A/B	209.6	319, 443	319, 443	8.57, 9.78	3.81, 5.81	6.05, 11.42
7 A/B	213.2	393, 342	393, 342	9.00, 8.90	4.83, 5.74	9.01, 8.32
8 A/B	196.8	346, 343	346, 343	9.39, 8.64	3.56, 5.04	6.39, 7.66
9 A/B	180.4	411, 389	411, 389	9.12, 9.38	4.53, 5.6	9.21, 9.35
10 A/B	-	800, 803	1134,1085	10.2, 10.1	32.44,24.72	284.25,191.53

Table 4.2 Tensile properties of SLM+EBW samples

Sample Label	EBW Heat Input (J/mm)	YS (MPa)	UTS (MPa)	Young's Modulus (GPa)	Elongation at Fracture (%)	Toughness (J/mm³ x 10⁻³)
11A/B	295.3	720, 722	937, 998	10.9, 10.5	16.9, 22.5	102, 155
12 A/B	272.6	715, 724	925, 987	11.0, 10.5	17.0, 20.6	98, 143
13 A/B	249.8	722, 703	951, 1004	10.8, 10.4	19.1, 22.3	117, 161
14 A/B	247.6	714, 724	899, 967	10.9, 10.7	15.1, 18.2	85, 102
15 A/B	228.6	737, 706	976, 932	10.9, 10.6	19.5, 16.8	125, 103
16 A/B	209.6	724, 709	889, 931	10.7, 11.6	15.8, 16.4	87, 102
17 A/B	213.2	719, 712	927, 899	10.9, 10.8	18.8, 13.4	125, 75
18 A/B	196.8	702, 708	891, 888	10.7, 11.2	16.5, 14	88, 77
19 A/B	180.4	735, 710	1004, 953	10.9, 11.1	22.7, 17.5	159, 110
20 A/B	-	741, 745	1045,1024	10.8, 10.9	28.1, 27.7	210, 198

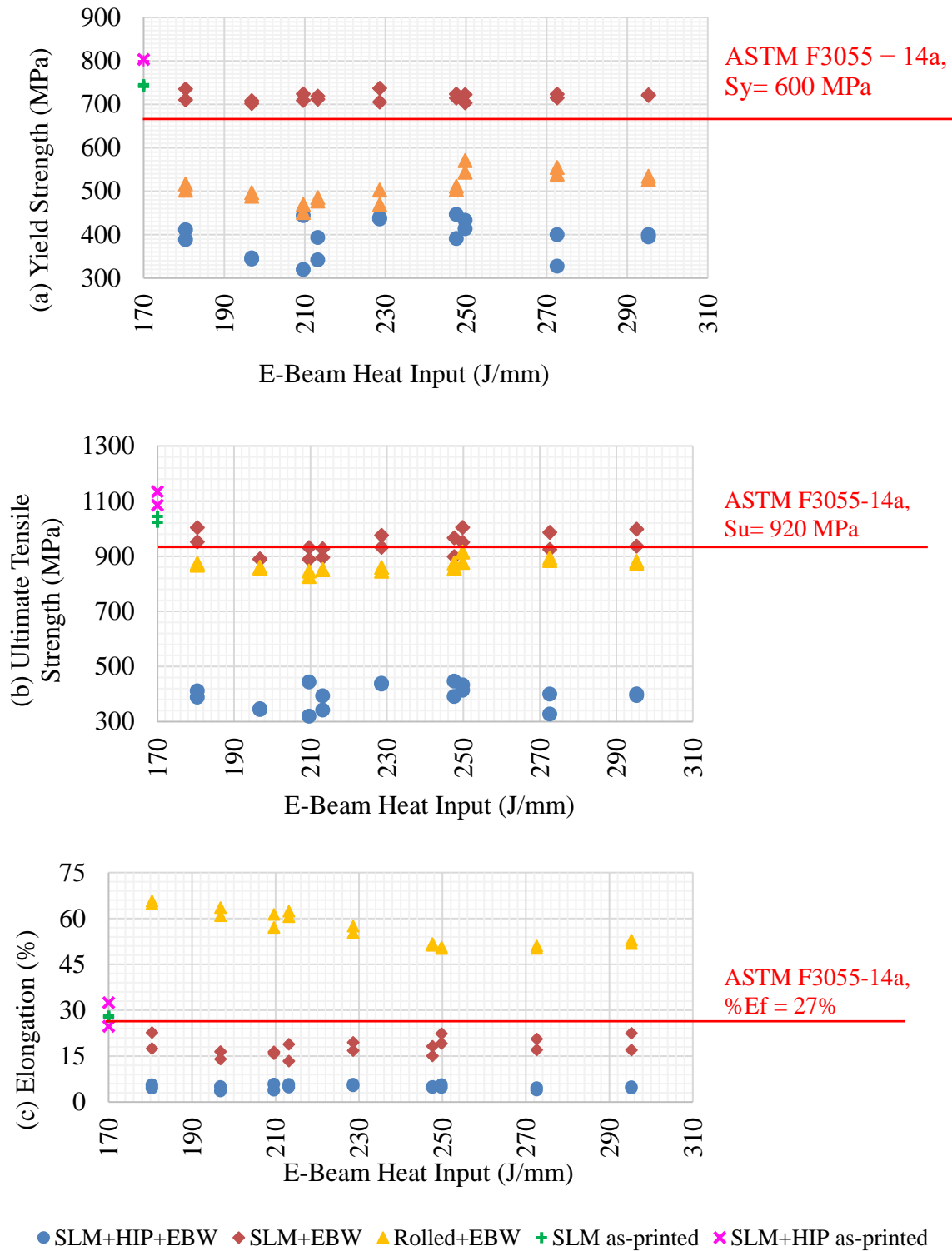


Figure 4.9 Variation of (a) Yield Strength, (b) Ultimate Tensile Strength and (c) Elongation of welded samples with E-Beam heat input

Referring to Figure 4.8, and Figure 4.9, it was observed that:

- The stress-strain curves had good repeatability at the same heat input for all conditions. A similar trend was observed for EBW of rolled IN718 samples in a previously published literature (Agilan et al., 2014).
- The yield strengths of all the SLM+EBW samples exceeded that of the rolled samples and the ASTM F3055-14a specification (600MPa). However, the SLM+HIP+EBW samples were extremely brittle and could neither exceed the rolled sample properties nor the specification.
- In the case of tensile strength, SLM+EBW samples exceeded the rolled samples at all the heat inputs. Also, at least one replicate of each welded sample except for sample 18A-B (196.8 J/mm) exceeded the ASTM specification (920MPa). Again, the SLM+HIP+EBW samples could not exceed the rolled samples and the specification.
- All SLM'ed welded samples were brittle and thus could neither meet the specifications or the rolled samples. However, as-printed SLM'ed samples 10A/B and 20A/B did meet the ASTM specifications (27%).

4.3. Microhardness

The typical microhardness test result (for samples - 9A/B, 19A/B, and A9 - welded at 180.4 J/mm) is shown in Figure 4.10. The origin of the coordinate system XY is located at the top of the weld zone as indicated in Figure 3.16. Dotted lines indicate the weld zone width at the respective weld depth. Refer Figure 4.11 for a summary of hardness test results for samples at different heat inputs. It can be observed that:

- In general, the rolled samples were the softest followed by the SLM+HIP+EBW samples. SLM+EBW samples were the hardest. Nb-rich Laves were formed in the SLM'ed samples due to the rapid heating and cooling of IN718 powder. These Laves impede the dislocation motion thereby increasing the hardness of the material. The HIP may have homogenized the material matrix and dissolved some of the Laves reducing their hardness.
- The top of the weld was observed to be softer than the weld zone below for all types of samples. The top of the weld was subjected to the electron beam for a longer time promoting grain growth leading to the softening of the material. A similar trend was observed for EBW of rolled IN718 samples in prior published data(Gao et al., 2011).
- In all the samples, the weld zone was found to be softer than the base metal. This was due to the rapid heating and cooling of the molten weld pool leading to a formation of inter-crystalline delta phases in the grain boundaries resulting in the reduction of the hardness in SLM'ed samples. The preferential grain structure in the rolled samples was disturbed due to the re-melting of the material during the welding process leading to the reduction in the hardness of these samples. The same was reported previously (Gao et al., 2011).

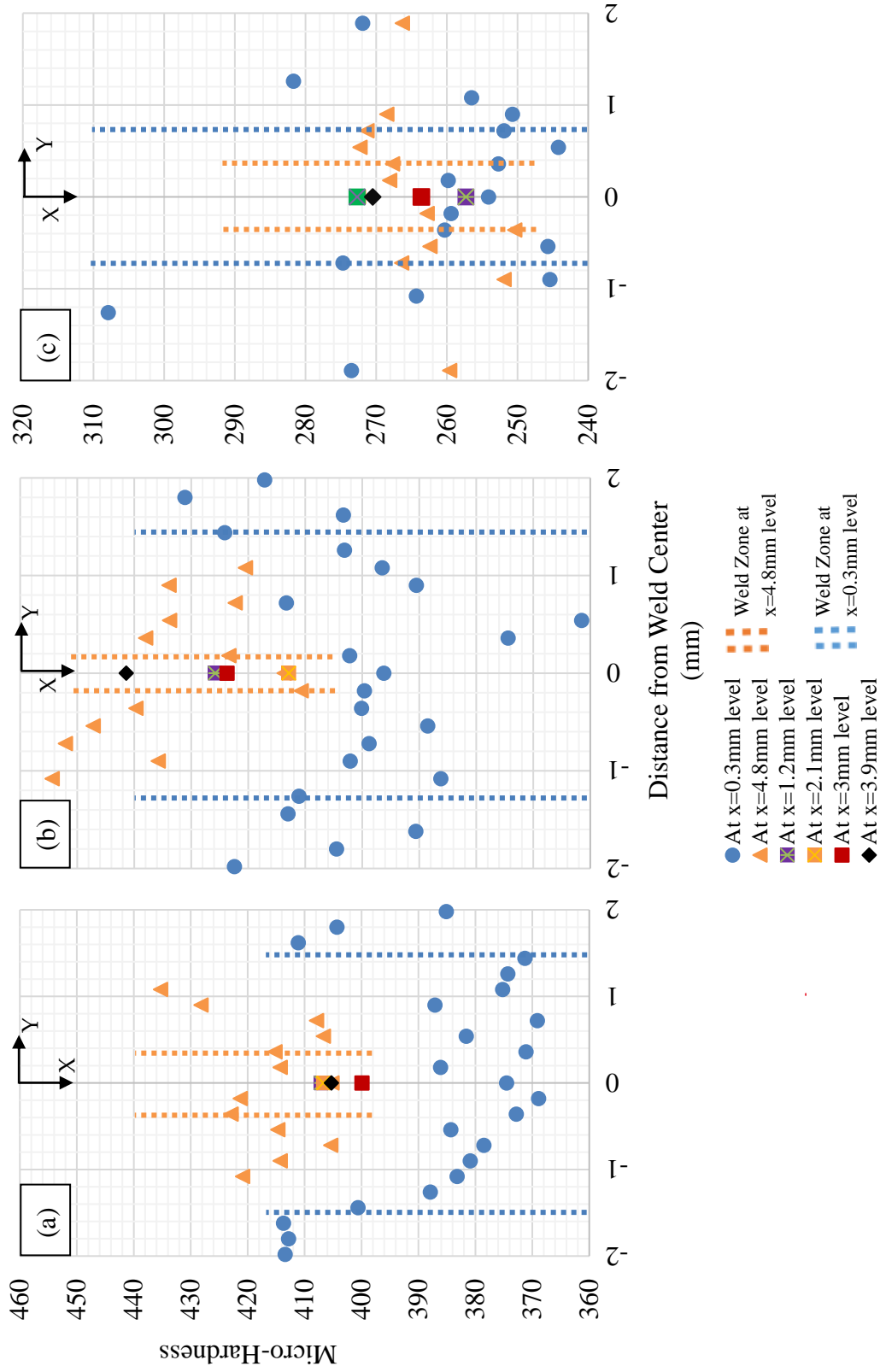


Figure 4.10 Microhardness of samples welded at 180.4J/mm: (a) SLM+HIP+EBW sample 9A/B, (b) SLM+EBW sample 19A/B, and (c) Rolled+EBW sample A9

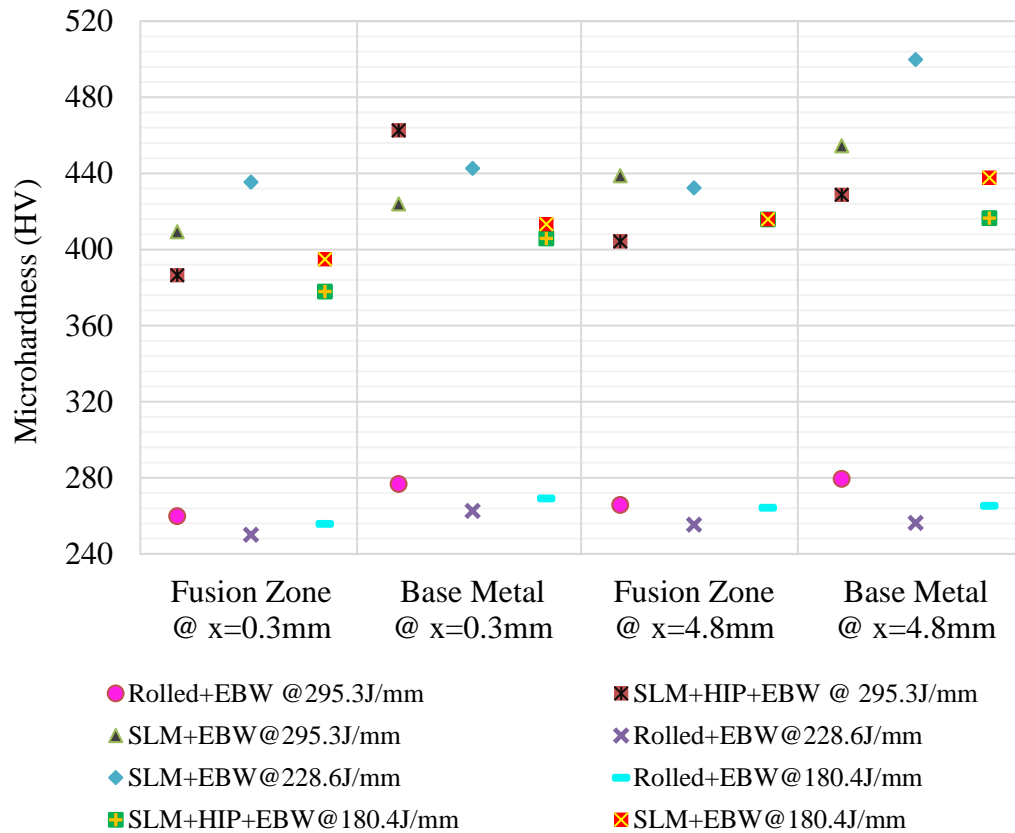


Figure 4.11 Average hardness of each type of sample at high (295.3J/mm), medium (228.6J/mm), and low(180.4J/mm) heat inputs

4.4. Fractography

The tensile behavior of the SLM’ed welds is explained by the microstructure of their fracture surfaces in this section. As-printed SLM’ed sample 20A fractured randomly away from the gage center. The fracture surfaces of this sample revealed low ductility as seen in Figure 4.12. Unmelted IN718 powder particles were observed indicating a need for further optimization of SLM parameters. These unmelted particles acted as the weak spots in the material matrix and degraded the mechanical properties.

Brittle NbC particles and laves were also detected which contributed to the brittle fracture of the sample.

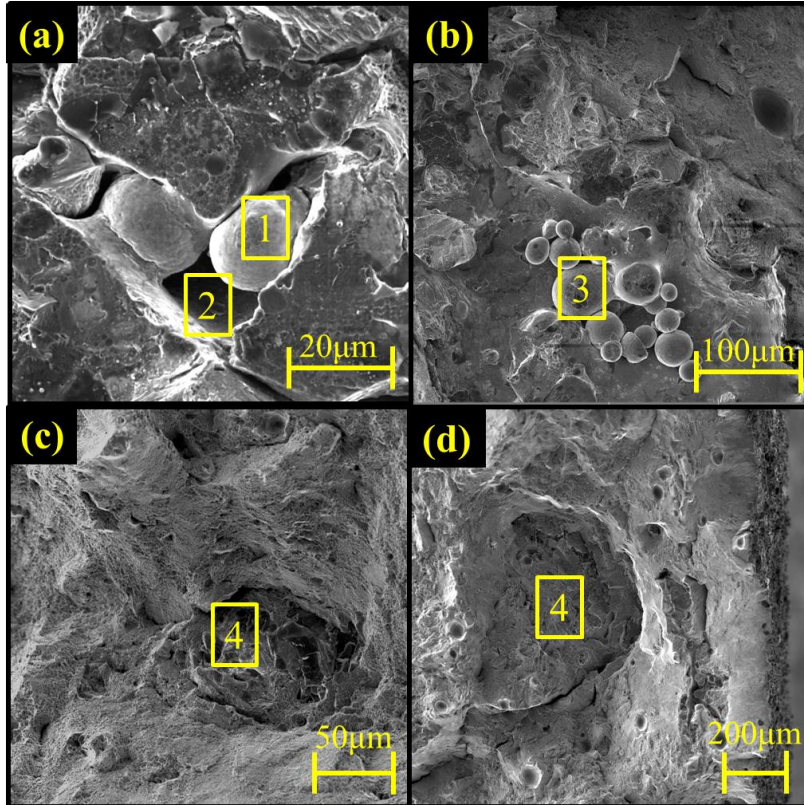


Figure 4.12 SEM fractography of sample 20A (as-printed SLM); (a,b): Un-melted IN718 powder particles (Label 1 & 3), unfilled zone (label 2); (c) & (d) Brittle Laves (label 4)

SLM+EBW sample 16A fractured outside the weld with a brittle mechanism due to the presence of defects at the fracture site. Porosity was observed on the surface of the sample which could have been inherited from the SLM process. Large sites of brittle NbC precipitates are also observed as seen in Figure 4.13.

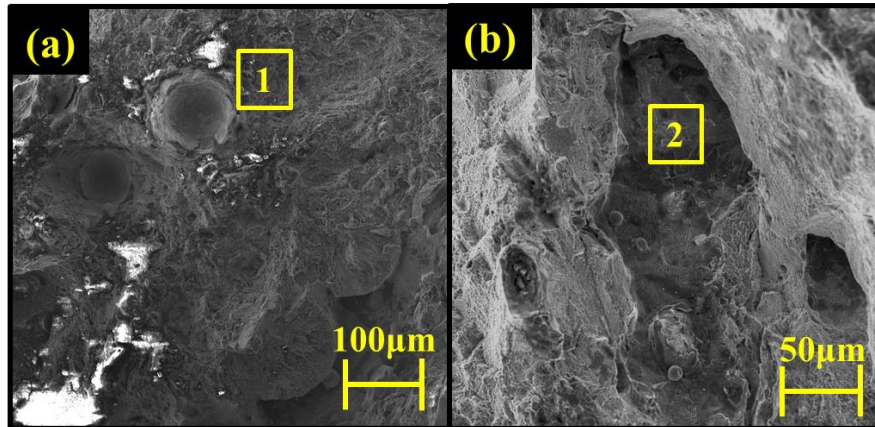


Figure 4.13 SEM fractography of SLM+EBW sample 16A (209.6 J/mm) that fractured in the base metal; (a) Spherical pores (label 1) and (b) Brittle carbides (label 2)

Figure 4.14 (a) shows a smooth and flat surface indicating a disjointed SLM layer formed due to inadequate adhesion between adjacent layers on SLM+EBW sample 17B. Unmelted IN718 powder surrounded by a more ductile surface was also observed on the 17B fracture surface as seen in Figure 4.14 (b). As this powder particle was not melted and did not have any bond with the surrounding matrix, it was suspected to be a contaminant of some other material. EDS analysis indicated the presence of a large percentage of aluminum (35.6-37.7%) and oxygen (49-51.4%) followed by titanium (7.3-9.6%) at certain sites (Figure 4.15) as compared to the surrounding matrix (0% oxygen, 0.6% aluminum, and 1% titanium). Similar observations were previously reported and the precipitates were concluded to be brittle oxides – Al_2O_3 (Popovich et al., 2017). Better control of the SLM environment was recommended to prevent the formation of such oxides that adversely affect the mechanical properties of the material.

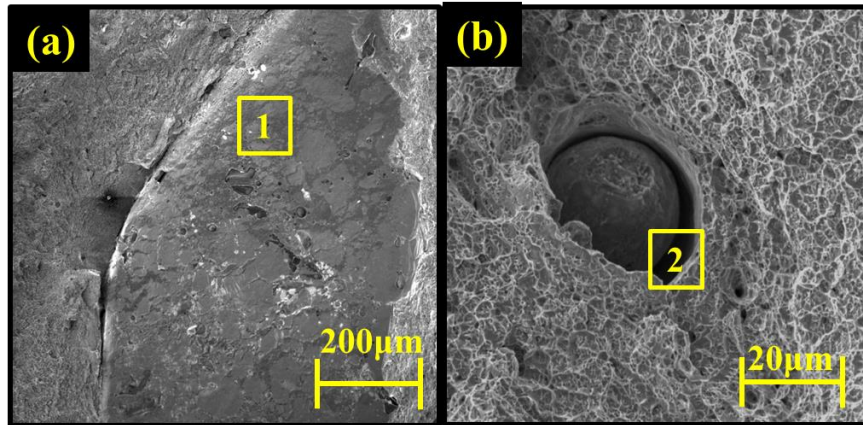


Figure 4.14 (a) Unfused SLM layer (label 1) and (b) Delaminated layer between the powder particle and the material matrix (label 2) on the fracture surface of sample 17B (213.2 J/mm). This sample fractured in the weld HAZ.

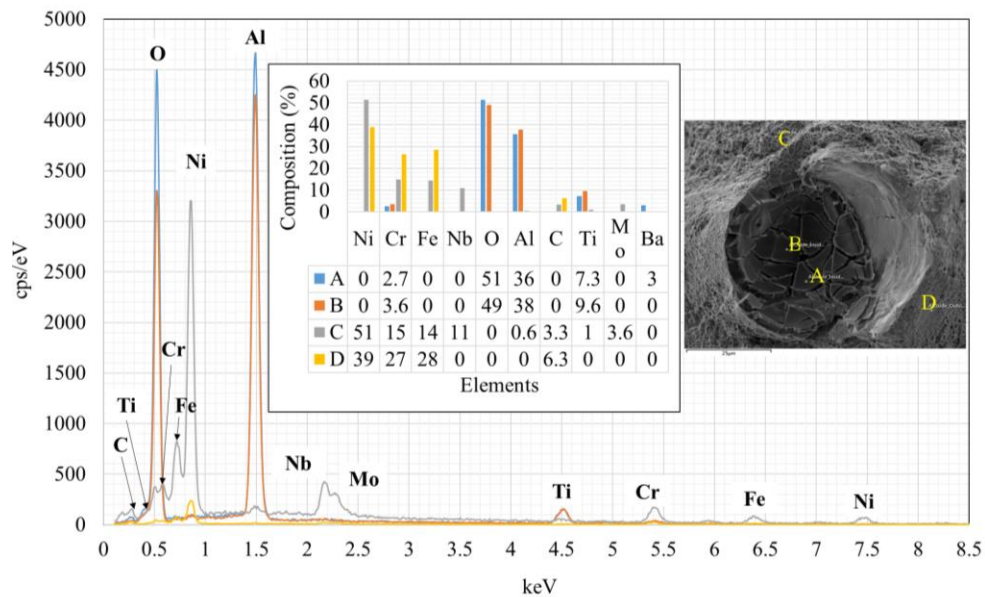


Figure 4.15 EDS analysis of a site on the fracture surface of sample 17B (213.2 J/mm) indicating the presence of metal oxides

The fracture surface of SLM+HIP+EBW sample 7A was extremely brittle with small-sized dimples and disjointed layers as seen in Figure 4.16 and Figure 4.17.

Perhaps, the exposure to high pressures and temperature during HIP led to a change in the grain structure of the samples leading to their extreme brittle nature.

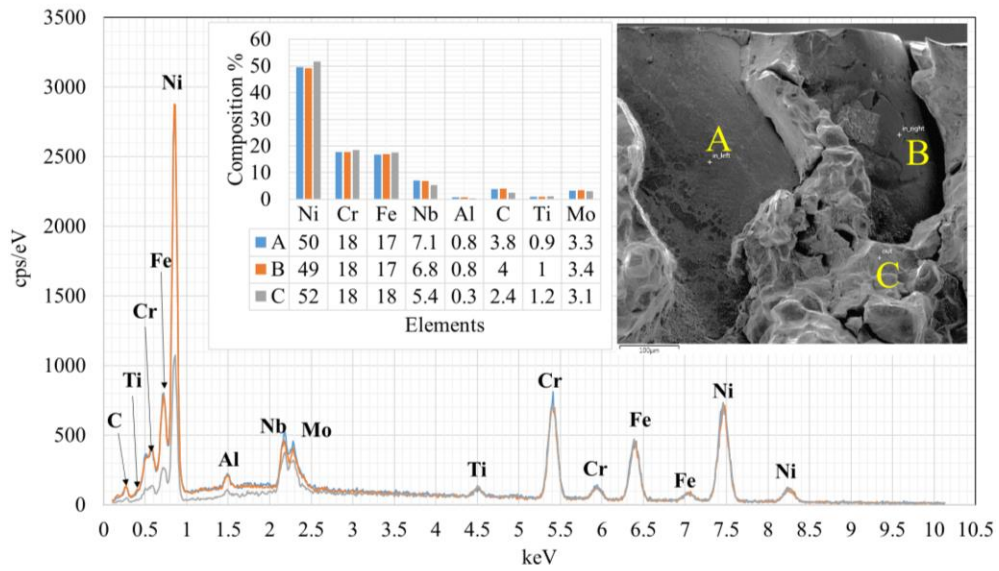


Figure 4.16 EDS analysis of a site on the fracture surface of SLM+HIP+EBW sample 7A (213.2 J/mm) showing disjointed IN718 layers (A and B)

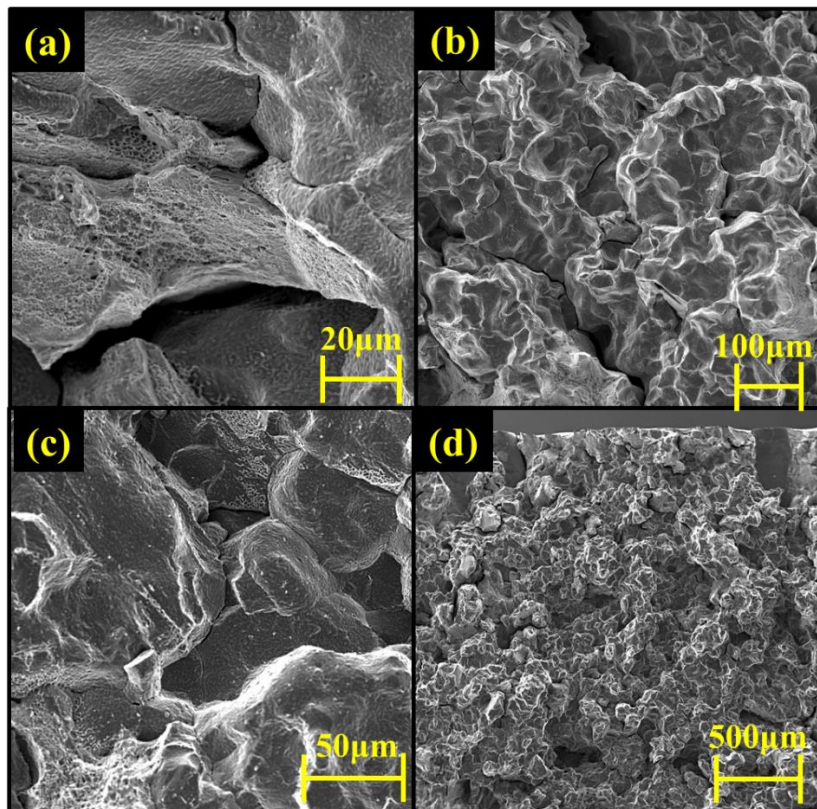


Figure 4.17 SEM fractography of SLM+HIP+EBW sample 7A (213.2 J/mm) indicating brittle surface. This sample was fractured in the weld HAZ.

Both SLM and EBW processes lead to the melting and solidification of the metal thereby affecting the chemical composition of the base metal alloy. The solidification of IN718 undergoes three stages (Janaki Ram et al., 2005). Initially, the liquid phase transformed into the secondary γ phase and led to the precipitation of solute particles such as Niobium, Carbon, Titanium, and Aluminum in the interdendritic region. This segregation led to the formation of Carbides (NbC). All or most percentages of carbon in the alloy were consumed in this process. The higher the percentage of carbon in the base alloy matrix, the higher is the tendency of the Carbide formation. This explains the presence of brittle carbide sites on the fracture surfaces of the SLM'ed base metal and welds as seen in Figure 4.12 and Figure 4.13. Further enrichment of solute led to the formation of the Laves phase before the solidification process ended. The formation of the laves phase was directly proportional to the presence of segregated niobium. Niobium segregation depends majorly on the cooling rate of the molten alloy. The higher the cooling rate, the lower is the segregation of niobium (Janaki Ram et al., 2005). Thus, favorable material characteristics can be observed at high cooling rates during SLM or EBW. Niobium present in the alloy solution was shared by various secondary phases (δ , γ , γ' and γ'') during solidification. Thus, a higher percentage of any of these phases led to a reduction in the percentage of the others. In the case of weld fusion zone, the percentage of strengthening phase γ' and γ'' reduced due to high consumption of Nb by the δ and γ phases (Gao et al., 2011)(Janaki Ram et al., 2005). Further, the formation of laves and δ phase in the grain boundaries provided favorable sites for the nucleation of voids and fissures. Due to factors such as the non-uniform size

of metal powder, gaps were formed between the adjacent layers during the SLM process. This led to inadequate heat distribution and left some metal particles unmelted. The SLM process induces thermal gradients between adjacent layers thereby fusing them and leading to a formation of homogenous metal in an ideal case. Uneven layer thickness, fluctuation of laser power, powder contamination can form gaps between the adjacent layers Figure 4.14 (a). This leads to inadequate heat distribution and also was the reason for some powder particles to remain un-melted as seen in Figure 4.12 (a)&(b), and Figure 4.14 (b).

In summary, the brittleness of the SLM'ed samples was due to:

1. Unmelted particles, and unfused layers during the SLM process.
2. Gas-filled pores and voids.
3. Laves, carbides, and oxides that prevent adhesion between adjacent layers.
4. Delamination between the unmelted powders and adjacent material matrix.
5. Change in grain structure after exposure to high pressure and temperature in HIP

5. CONCLUSION

SLM'ed IN718 parts were welded using EBW and the results were compared with EBW of rolled IN718. The study showed that:

1. Excellent penetration depth was achieved for SLM IN718 by EBW without beam oscillations. The penetration depth was directly proportional to the Heat input. The overall weld cross-section area also increased with an increase in the beam current and thus, the heat input.
2. The Weld zone was found to be softer as compared to the base metal hardness. This was due to the probable formation of laves and δ phases at the weld center in place of strengthening γ' and γ'' phases. Vickers hardness at the top of the weld (at the beam entrance) was also lower as compared to that at the bottom due to a faster cooling rate in the sample.
3. SLM+EBW samples exceeded the tensile and yield strength but could not match the ductility of the rolled samples and the ASTM F3055-14a specification. SLM+HIP+EBW samples were weaker than both SLM+EBW samples and the rolled samples and also could not meet the ASTM specifications in any aspect.
4. The analysis of the fracture surface revealed the presence of spherical pores, un-melted powder particles, delaminated layers, Nb-rich brittle Laves phase particles, and Al-Ti Oxide inclusions. These defects contributed to the brittle nature of the SLM'ed samples.

To improve the properties of the welds, the following steps are recommended:

1. Implementing statistical analysis to quantify the effect of variation in EBW parameters on the weld properties.
2. Optimizing the SLM parameters to minimize the defects:
 - SLM energy density levels to be explored: 45.5, 54.5, 68.2 J/mm³ against 53 J/mm³ used in the present study.
3. Improving the ductility of the welds by Homogenization at 1080°C, 1hr, water quenching.
4. Further improving the tensile strength by:
 - Solution Treatment: 980°C, 1hr, air cooling
 - Dual Aging: 720°C, 8hr, furnace cooling at 50°C /hr to 620°C + 620°C, 8hr, air cooling

REFERENCES

- [1] Agilan, M., Venkateswaran, T., Sivakumar, D., & Pant, B. (2014). Effect of Heat Input on Microstructure and Mechanical Properties of Inconel-718 EB Welds. *Procedia Materials Science*, 5, 656–662. <https://doi.org/10.1016/j.mspro.2014.07.312>
- [2] Arata, Y., Terai, K., & Matsuda, S. (1973). Characteristics of a Weld Defect and Its Prevention in Electron Beam Welding. Pt. 1. Characteristics of Weld Porosities. *Transactions of the JWRI, Report I*.
- [3] Aydinöz, M. E., Brenne, F., Schaper, M., Schaak, C., Tillmann, W., Nellesen, J., & Niendorf, T. (2016). On the microstructural and mechanical properties of post-treated additively manufactured Inconel 718 superalloy under quasi-static and cyclic loading. *Materials Science and Engineering A*, 669, 246–258. <https://doi.org/10.1016/j.msea.2016.05.089>
- [4] Casalino, G., Campanelli, S. L., & Ludovico, A. D. (2013). Laser-arc hybrid welding of wrought to selective laser molten stainless steel. *International Journal of Advanced Manufacturing Technology*, 68(1–4), 209–216. <https://doi.org/10.1007/s00170-012-4721-z>
- [5] Chi, C. T., Chao, C. G., Liu, T. F., & Wang, C. C. (2008). Optimal parameters for low and high voltage electron beam welding of AZ series magnesium alloys and mechanism of weld shape and pore formation. *Science and Technology of Welding and Joining*, 13(2), 199–211. <https://doi.org/10.1179/174329307X227274>
- [6] Deng, D., Peng, R. L., Brodin, H., & Moverare, J. (2018). Microstructure and mechanical properties of Inconel 718 produced by selective laser melting: Sample orientation dependence and effects of post heat treatments. *Materials Science and Engineering A*, 713(December 2017), 294–306. <https://doi.org/10.1016/j.msea.2017.12.043>
- [7] EISELSTEIN, H. L. (2020). *STP369-EB/Apr. 1965 metallurgy of a columbium - hardened nickel - chromium - iron alloy*.
- [8] Gao, P., Zhang, K. F., Zhang, B. G., Jiang, S. S., & Zhang, B. W. (2011). Microstructures and high temperature mechanical properties of electron beam welded Inconel 718 superalloy thick plate. *Transactions of Nonferrous Metals Society of China (English Edition)*, 21(SUPPL. 2), s315–s322. [https://doi.org/10.1016/S1003-6326\(11\)61598-7](https://doi.org/10.1016/S1003-6326(11)61598-7)

- [9] Hong, J. K., Park, J. H., Park, N. K., Eom, I. S., Kim, M. B., & Kang, C. Y. (2008). Microstructures and mechanical properties of Inconel 718 welds by CO₂ laser welding. *Journal of Materials Processing Technology*, 201(1–3), 515–520. <https://doi.org/10.1016/j.jmatprotec.2007.11.224>
- [10] Huang, C. A., Wang, T. H., Lee, C. H., & Han, W. C. (2005). A study of the heat-affected zone (HAZ) of an Inconel 718 sheet welded with electron-beam welding (EBW). *Materials Science and Engineering A*, 398(1–2), 275–281. <https://doi.org/10.1016/j.msea.2005.03.029>
- [11] Huang, J. (2011). the Characterisation and Modelling of Porosity Formation in Electron Beam Welded Titanium Alloys. *Computer*, September, 207.
- [12] Janaki Ram, G. D., Venugopal Reddy, A., Prasad Rao, K., & Madhusudhan Reddy, G. (2005). Microstructure and mechanical properties of Inconel 718 electron beam welds. *Materials Science and Technology*, 21(10), 1132–1138. <https://doi.org/10.1179/174328405X62260>
- [13] Jawwad, A. K. A., Strangwood, M., & Davis, C. L. (2005). Microstructural modification in full penetration and partial penetration electron beam welds in inconel-718 (IN-718) and its effect on fatigue crack initiation. *Metallurgical and Materials Transactions A: Physical Metallurgy and Materials Science*, 36(5), 1237–1247. <https://doi.org/10.1007/s11661-005-0216-y>
- [14] Kar, J., Chakrabarti, D., Roy, S. K., & Roy, G. G. (2019). Beam oscillation, porosity formation and fatigue properties of electron beam welded Ti-6Al-4V alloy. *Journal of Materials Processing Technology*, 266(June 2018), 165–172. <https://doi.org/10.1016/j.jmatprotec.2018.10.040>
- [15] Khairallah, S. A., Anderson, A. T., Rubenchik, A., & King, W. E. (2016). Laser powder-bed fusion additive manufacturing: Physics of complex melt flow and formation mechanisms of pores, spatter, and denudation zones. *Acta Materialia*, 108, 36–45. <https://doi.org/10.1016/j.actamat.2016.02.014>
- [16] Knorovsky, G. A., Cieslak, M. J., Headley, T. J., Romig, A. D., & Hammett, W. F. (1989). INCONEL 718: A solidification diagram. *Metallurgical Transactions A*, 20(10), 2149–2158. <https://doi.org/10.1007/BF02650300>
- [17] *Luvak Laboratories*. (n.d.). Retrieved August 20, 2020, from <http://www.luvak.com/>

- [18] Madhusudhana Reddy, G., Srinivasa Murthy, C. V., Srinivasa Rao, K., & Prasad Rao, K. (2009). Improvement of mechanical properties of Inconel 718 electron beam welds-influence of welding techniques and postweld heat treatment. *International Journal of Advanced Manufacturing Technology*, 43(7–8), 671–680. <https://doi.org/10.1007/s00170-008-1751-7>
- [19] Mei, Y., Liu, Y., Liu, C., Li, C., Yu, L., Guo, Q., & Li, H. (2016). Effect of base metal and welding speed on fusion zone microstructure and HAZ hot-cracking of electron-beam welded Inconel 718. *Materials and Design*, 89, 964–977. <https://doi.org/10.1016/j.matdes.2015.10.082>
- [20] Nahmany, M., Rosenthal, I., Benishti, I., Frage, N., & Stern, A. (2015). Electron beam welding of AlSi10Mg workpieces produced by selected laser melting additive manufacturing technology. *Additive Manufacturing*, 8, 63–70. <https://doi.org/10.1016/j.addma.2015.08.002>
- [21] Patel, V., Sali, A., Hyder, J., Corliss, M., Hyder, D., & Hung, W. (2020). Electron Beam Welding of Inconel 718 Electron Beam Welding of Inconel 718. *Procedia Manufacturing*, 48(2019), 428–435. <https://doi.org/10.1016/j.promfg.2020.05.065>
- [22] Popovich, V. A., Borisov, E. V., Popovich, A. A., Sufiiarov, V. S., Masaylo, D. V., & Alzina, L. (2017). Impact of heat treatment on mechanical behaviour of Inconel 718 processed with tailored microstructure by selective laser melting. *Materials and Design*, 131(January), 12–22. <https://doi.org/10.1016/j.matdes.2017.05.065>
- [23] Prashanth, K. G., Damodaram, R., Scudino, S., Wang, Z., Prasad Rao, K., & Eckert, J. (2014). Friction welding of Al-12Si parts produced by selective laser melting. *Materials and Design*, 57, 632–637. <https://doi.org/10.1016/j.matdes.2014.01.026>
- [24] Raza, T., Andersson, J., & Svensson, L. E. (2018). Vareststraint weldability testing of additive manufactured alloy 718. *Science and Technology of Welding and Joining*, 23(7), 606–611. <https://doi.org/10.1080/13621718.2018.1437338>
- [25] Strößner, J., Terock, M., & Glatzel, U. (2015). Mechanical and Microstructural Investigation of Nickel-Based Superalloy IN718 Manufactured by Selective Laser Melting (SLM). *Advanced Engineering Materials*, 17(8), 1099–1105. <https://doi.org/10.1002/adem.201500158>
- [26] Tillmann, W., Schaak, C., Nellesen, J., Schaper, M., Aydinöz, M. E., & Hoyer, K. P. (2017). Hot isostatic pressing of IN718 components manufactured by selective laser melting. *Additive Manufacturing*, 13(May 2018), 93–102. <https://doi.org/10.1016/j.addma.2016.11.006>
- [27] Voort, G. Vander. (1991). *Inconel 718 (Alloy 718) and Modified Inconel 718*.

- [28] Xia, C., Zhao, M., Sun, W., Li, H., & Liu, P. (2018). microstructure and properties of 3D printed Inconel 718 joint brazed with BNi-2 amorphous filler metal. *Materials Research*, 22(1), 1–10. <https://doi.org/10.1590/1980-5373-MR-2018-0348>
- [29] Yu, H., Li, F., Yang, J., Shao, J., Wang, Z., & Zeng, X. (2018). Investigation on laser welding of selective laser melted Ti-6Al-4V parts: Weldability, microstructure and mechanical properties. *Materials Science and Engineering A*, 712(November 2017), 20–27. <https://doi.org/10.1016/j.msea.2017.11.086>

APPENDIX A

TENSILE STRESS-STRAIN CURVES

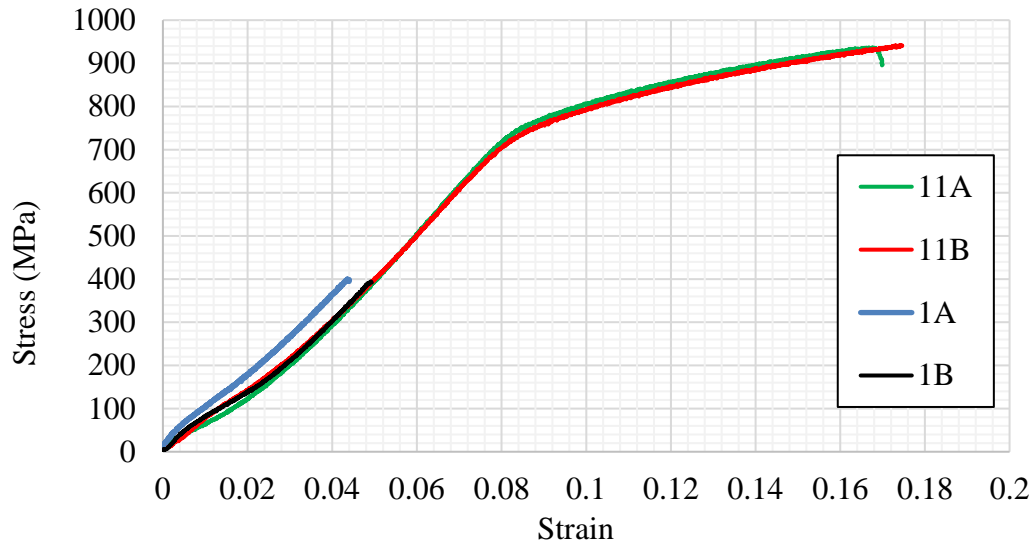


Figure 5.1 Stress-strain curve for samples welded at heat input 295.3 J/mm (1A/B - SLM+HIP+EBW, 11A/B - SLM+EBW)

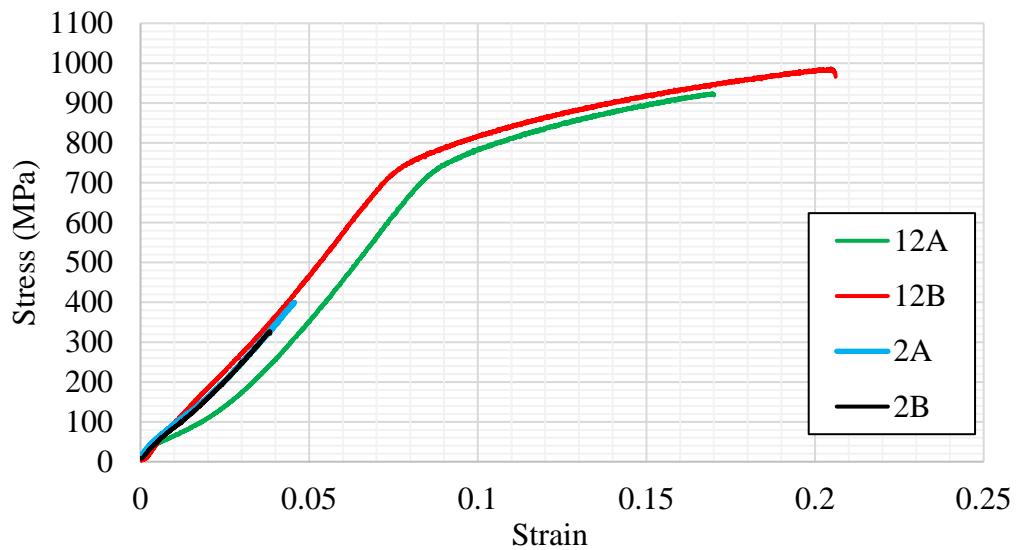


Figure 5.2 Stress-strain curve for samples welded at heat input 272.6 J/mm (2A/B - SLM+HIP+EBW, 12A/B - SLM+EBW)

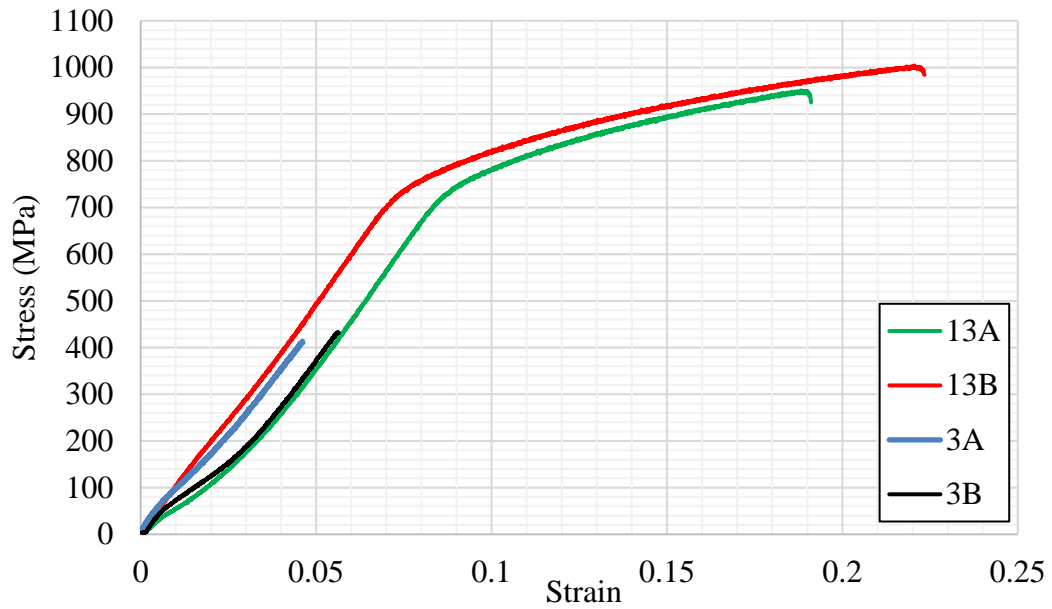


Figure 5.3 Stress-strain curve for samples welded at heat input 249.8 J/mm (3A/B - SLM+HIP+EBW, 13A/B - SLM+EBW)

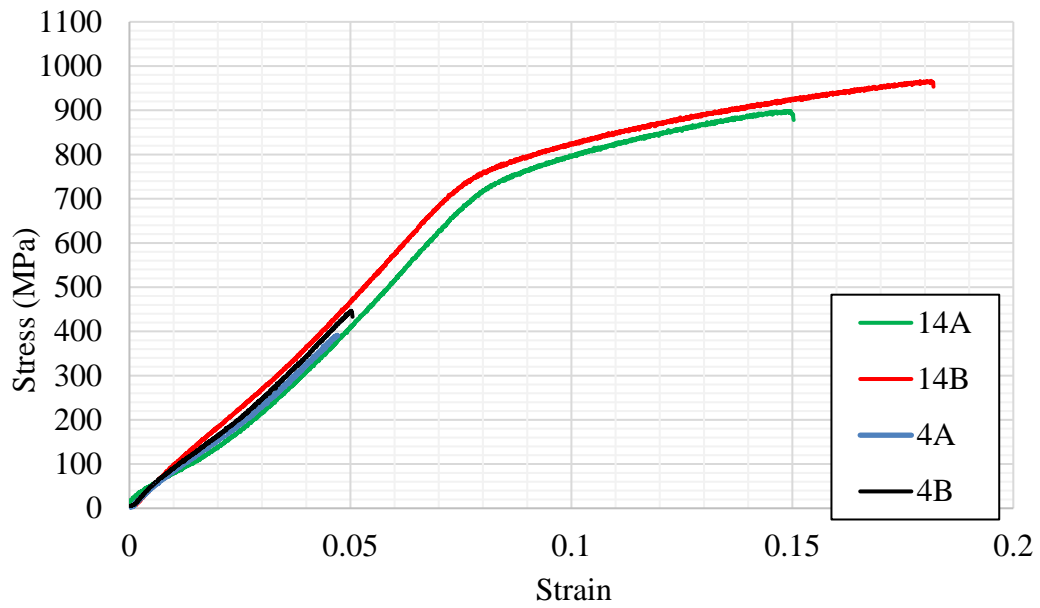


Figure 5.4 Stress-strain curve for samples welded at heat input 247.6 J/mm (4A/B - SLM+HIP+EBW, 14A/B - SLM+EBW)

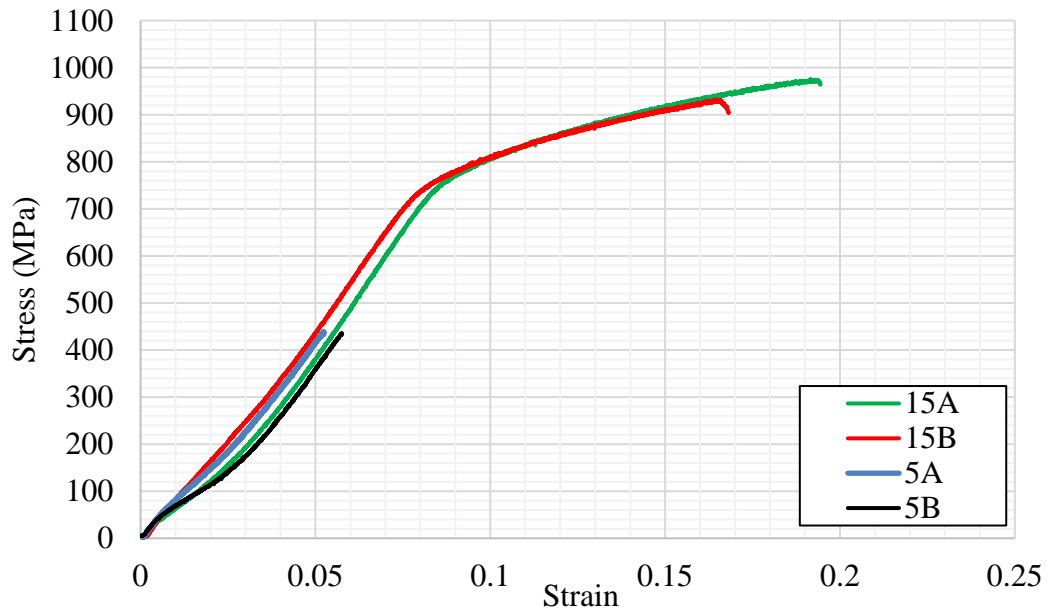


Figure 5.5 Stress-strain curve for samples welded at heat input 228.6 J/mm (5A/B - SLM+HIP+EBW, 15A/B - SLM+EBW)

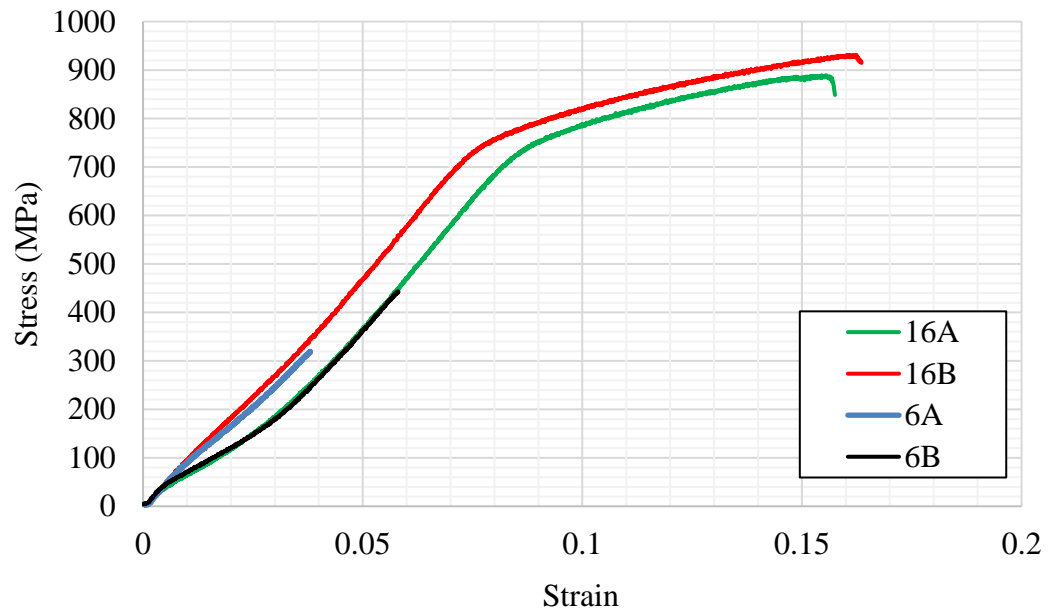


Figure 5.6 Stress-strain curve for samples welded at heat input 209.6 J/mm (6A/B - SLM+HIP+EBW, 16A/B - SLM+EBW)

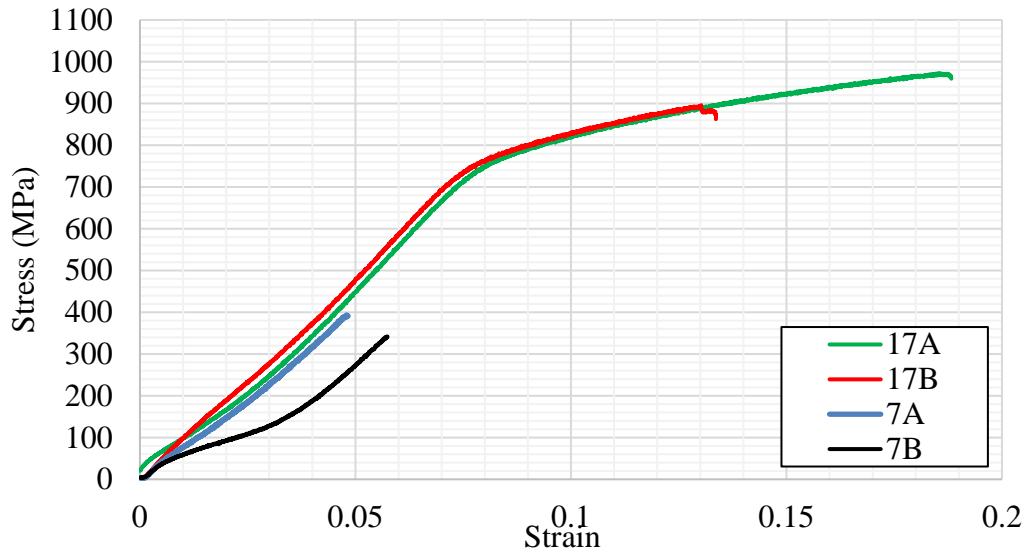


Figure 5.7 Stress-strain curve for samples welded at heat input 213.2 J/mm (7A/B - SLM+HIP+EBW, 17A/B - SLM+EBW)

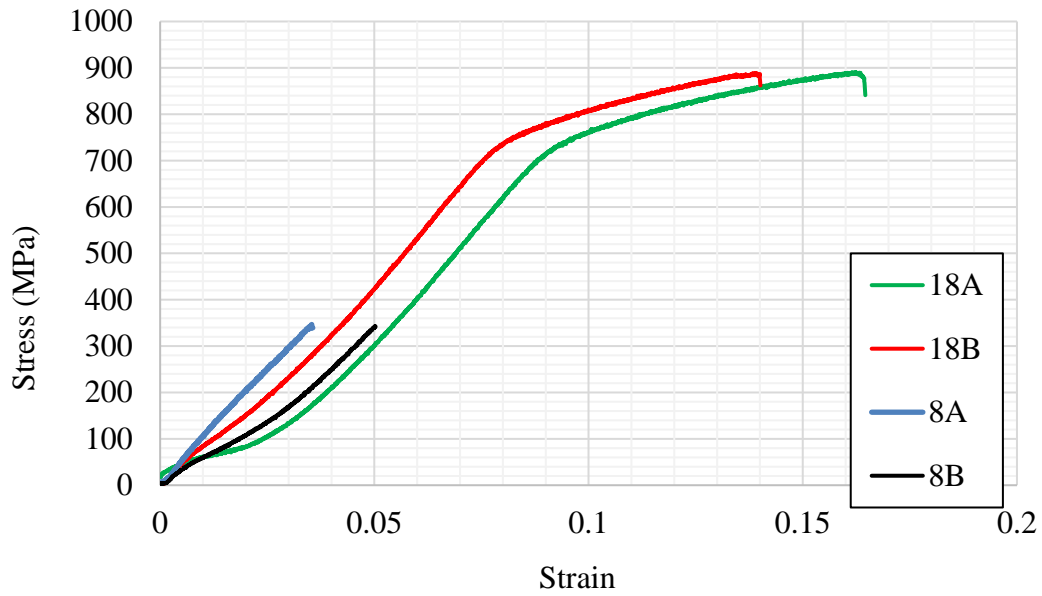


Figure 5.8 Stress-strain curve for samples welded at heat input 196.8 J/mm (8A/B - SLM+HIP+EBW, 18A/B - SLM+EBW)

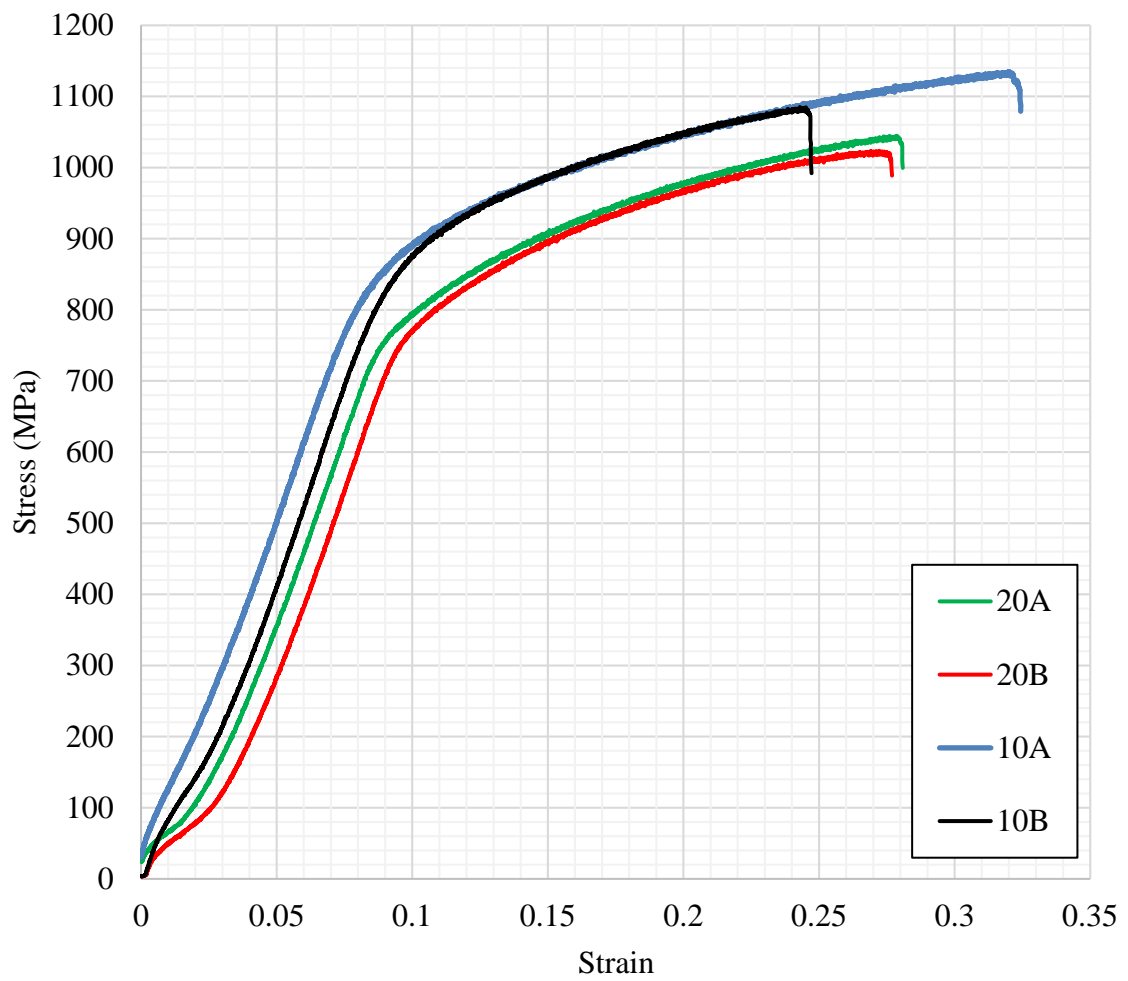


Figure 5.9 Stress-strain curve for as printed samples (10A/B - SLM+HIP+EBW, 20A/B - SLM+EBW)

APPENDIX B
MICROGRAPHS

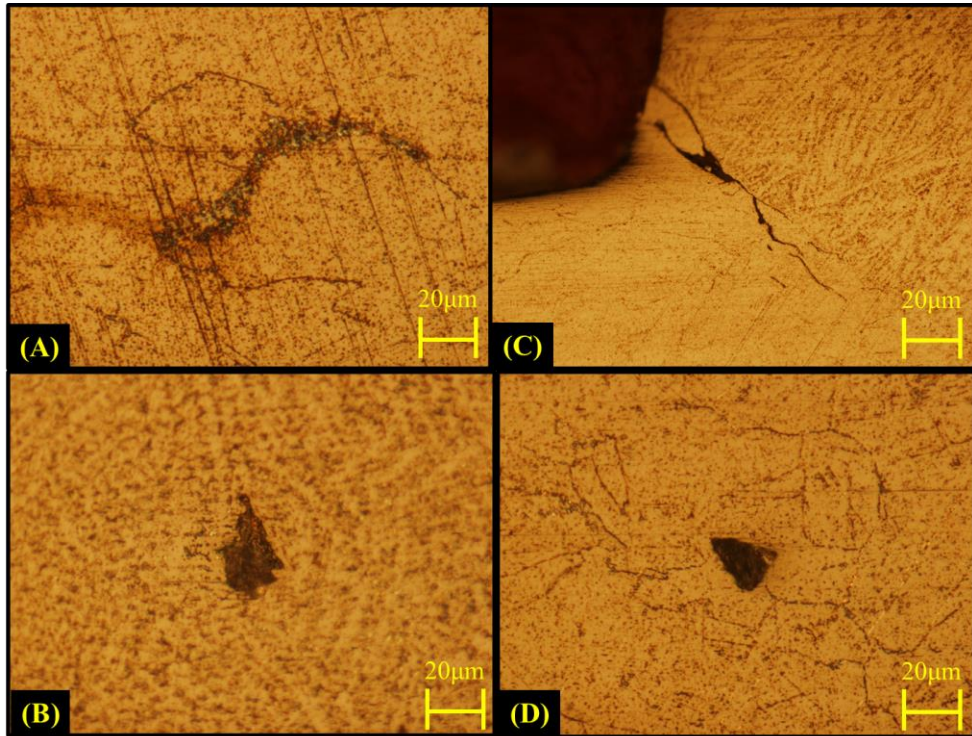


Figure 5.10 Defects on SLM+HIP+EBW sample 1A/1B (295.3 J/mm)

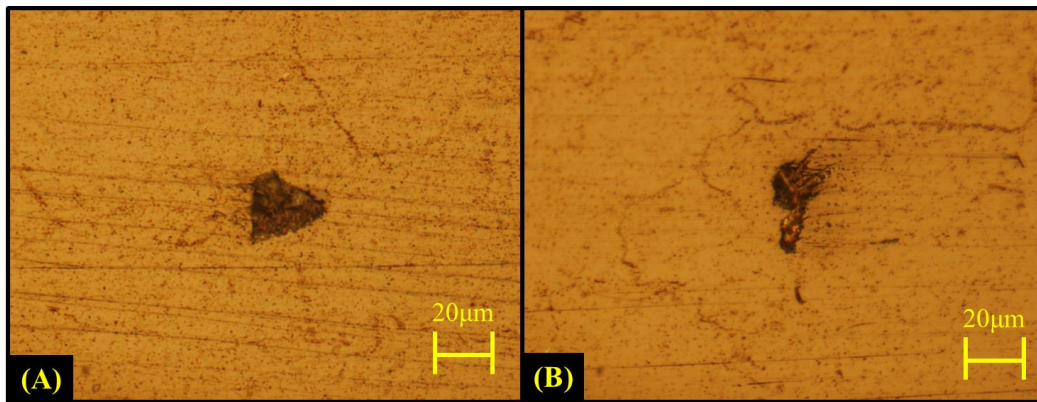


Figure 5.11 Defects on SLM+HIP+EBW sample 3A/3B (249.8 J/mm)

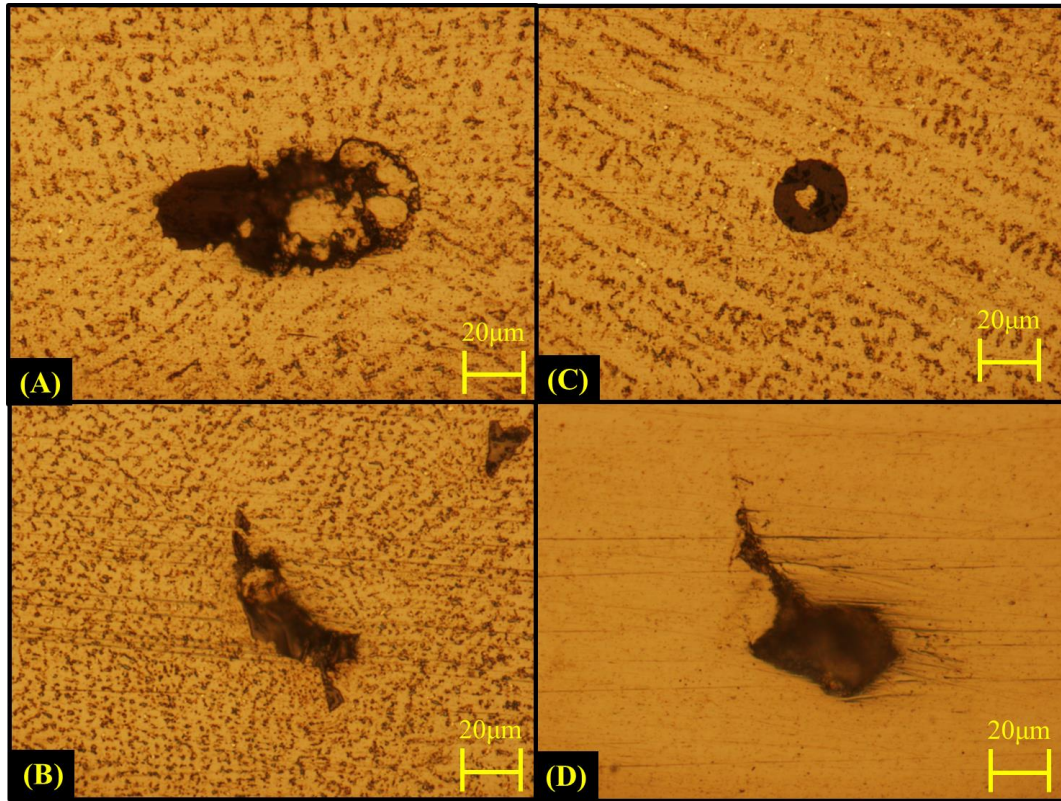


Figure 5.12 Defects on SLM+HIP+EBW sample 4A/4B (247.6 J/mm)

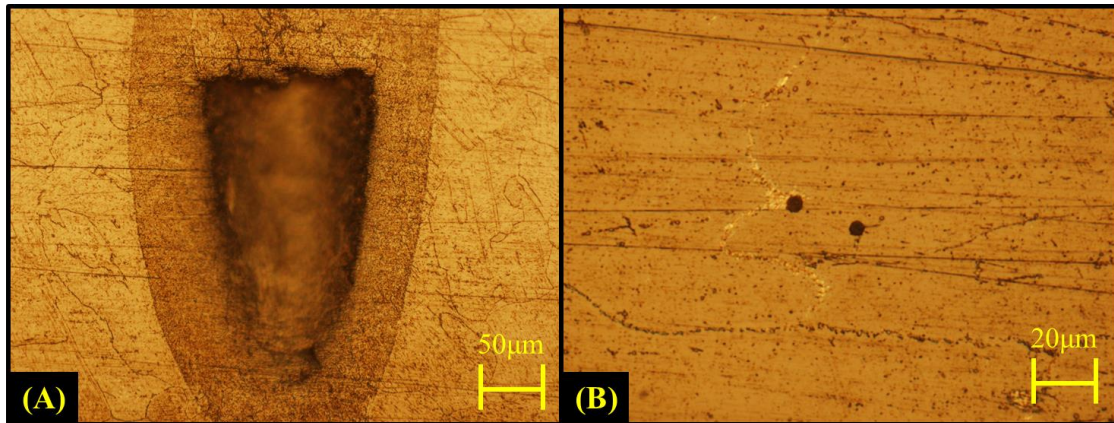


Figure 5.13 (A) Root keyhole defect on SLM+HIP+EBW sample 5A/5B (228.6 J/mm) (B) Pores on SLM+HIP+EBW sample 5A/5B base metal (228.6 J/mm)

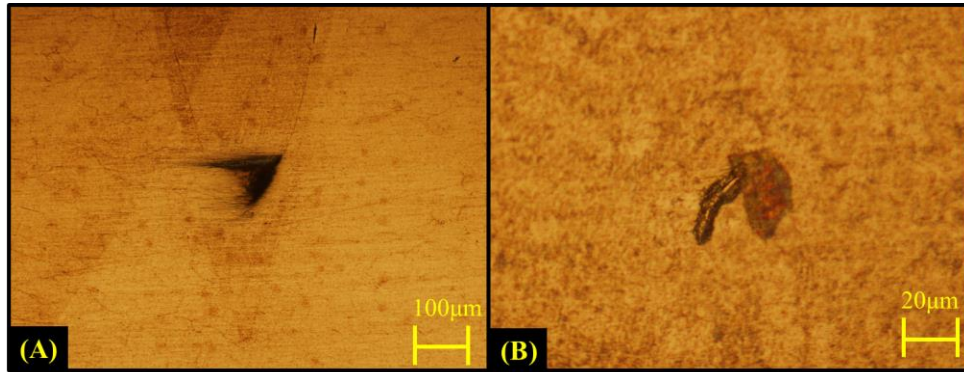


Figure 5.14 (A) Root keyhole defect on SLM+HIP+EBW sample 6A/6B (209.6 J/mm) (B) Defect on SLM+HIP+EBW sample 6A/6B weld (209.6 J/mm)

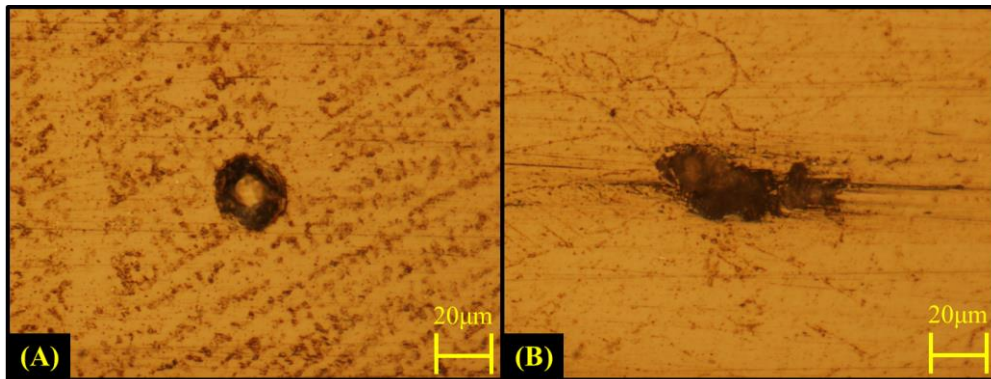


Figure 5.15 (A) Pore on SLM+HIP+EBW sample 7A/B weld (213.2 J/mm) (B) Defect on SLM+HIP+EBW sample 7A/B base metal (213.2 J/mm)

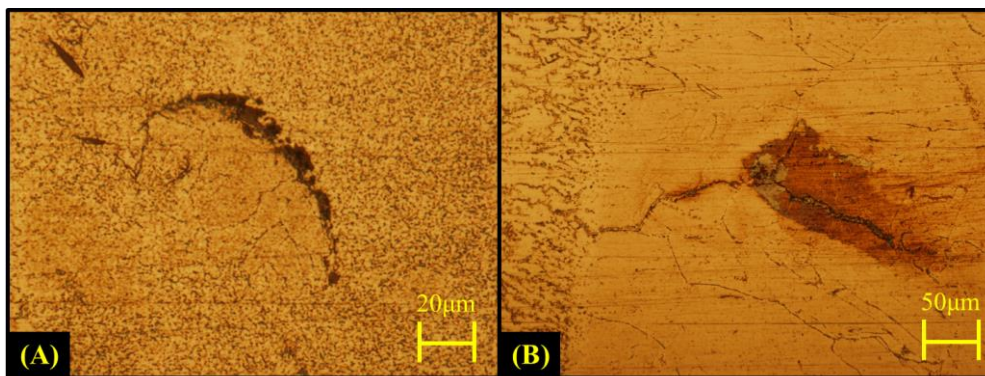


Figure 5.16 (A) Defect on SLM+HIP+EBW sample 8A/B weld (196.8 J/mm) (B) Crack on SLM+HIP+EBW sample 8A/B base metal (196.8 J/mm)

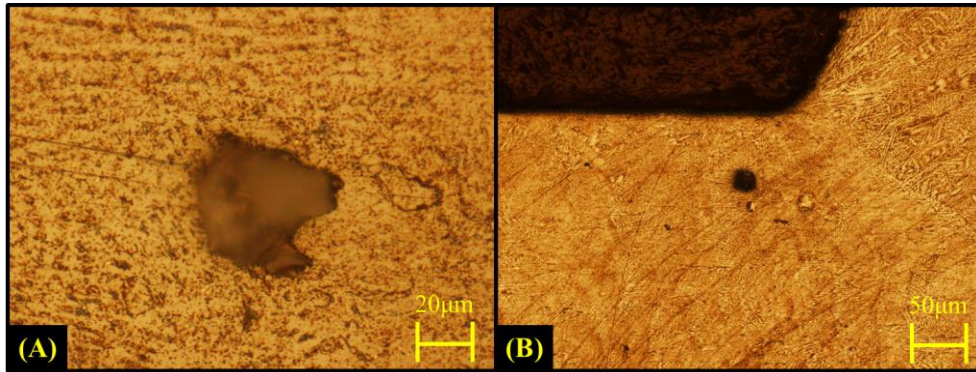


Figure 5.17 Defect on SLM+EBW sample 11A/B base metal (295.3 J/mm)

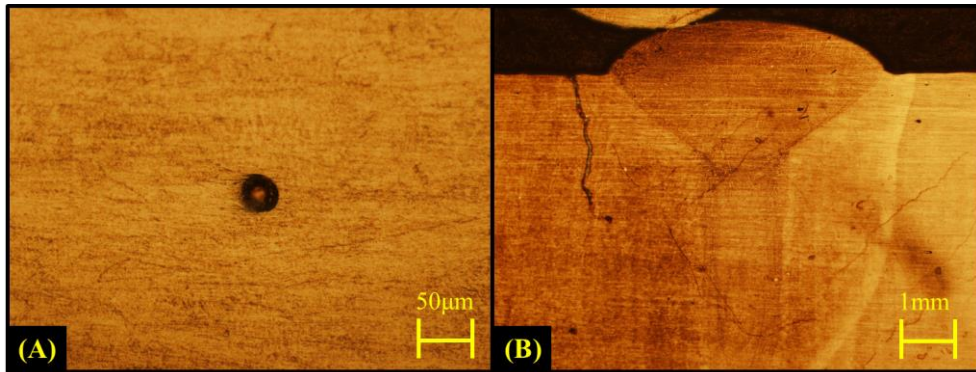


Figure 5.18 Defects on SLM+EBW sample 13A/B base metal (249.8 J/mm)

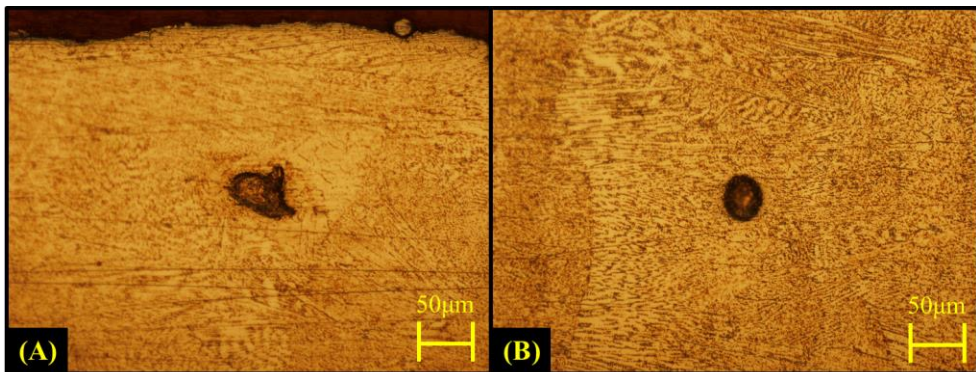


Figure 5.19 Defects on SLM+EBW sample 14A/B base metal (247.6 J/mm)

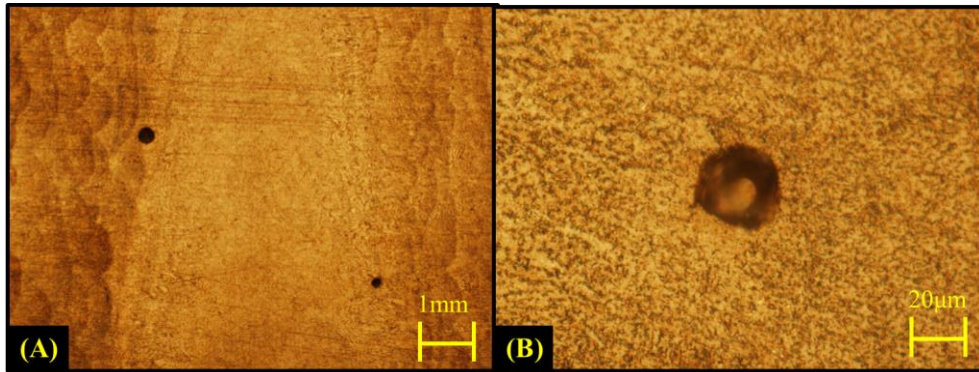


Figure 5.20 Pores on SLM+EBW sample 15A/B (228.6 J/mm)

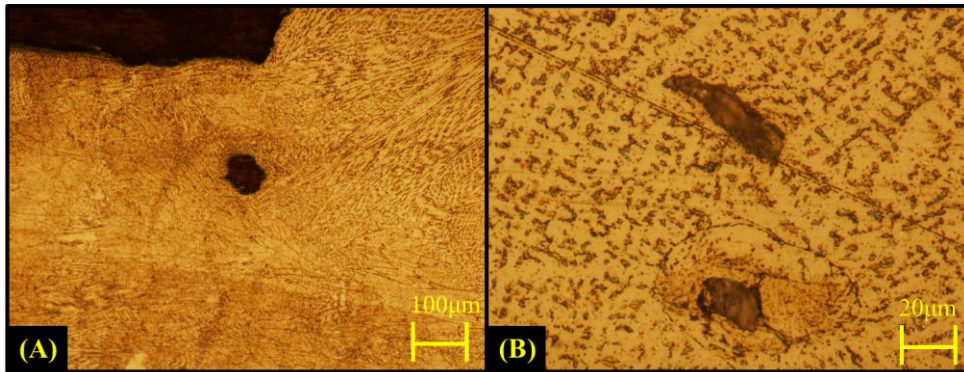


Figure 5.21 Pores on SLM+EBW sample 16A/B (209.6 J/mm) base metal

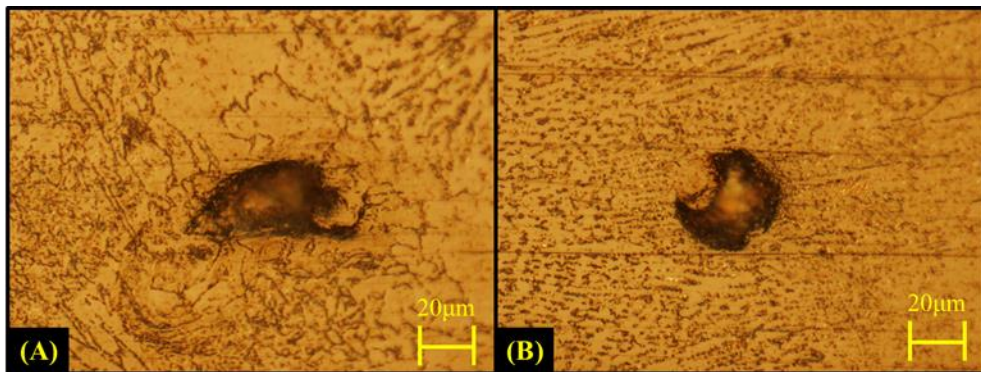


Figure 5.22 Defects on SLM+EBW sample 17A/B (213.2 J/mm) weld boundary

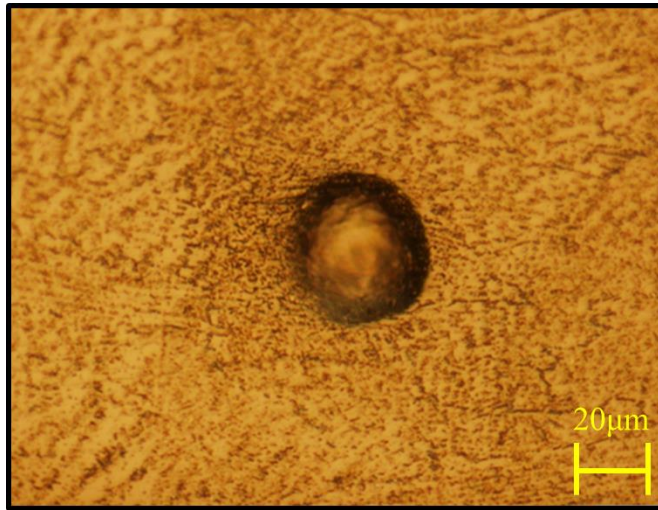


Figure 5.23 Pore on SLM+EBW sample 18A/B (196.8 J/mm) weld boundary

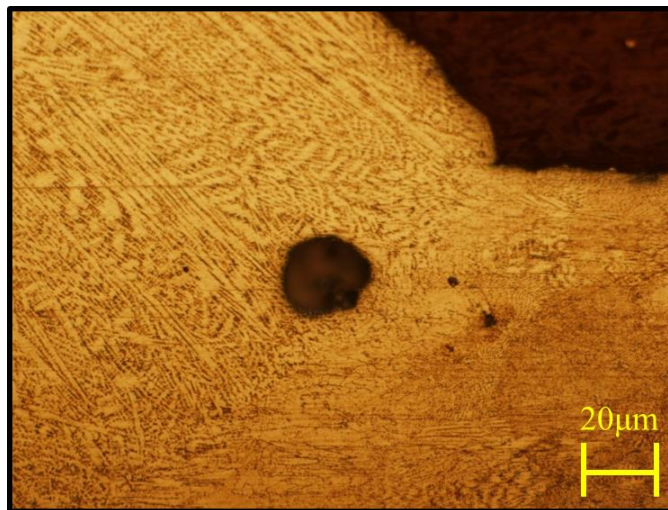


Figure 5.24 Pore on SLM+EBW sample 19A/B (180.4 J/mm) weld

APPENDIX C

FRACTOGRAPHY

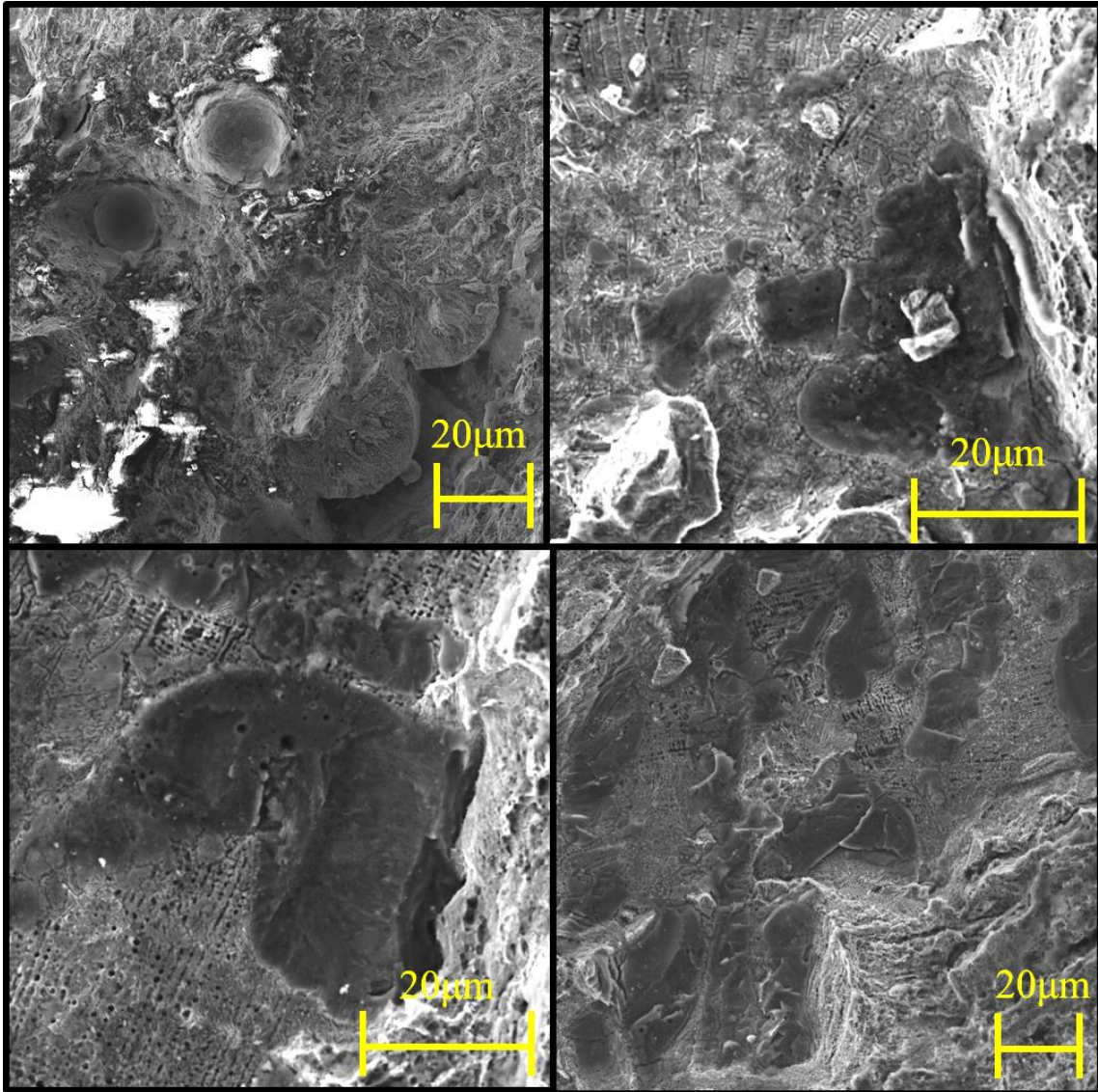


Figure 5.25 Fractography of SLM+EBW sample 16A/B (209.6 J/mm) fractured in the base metal

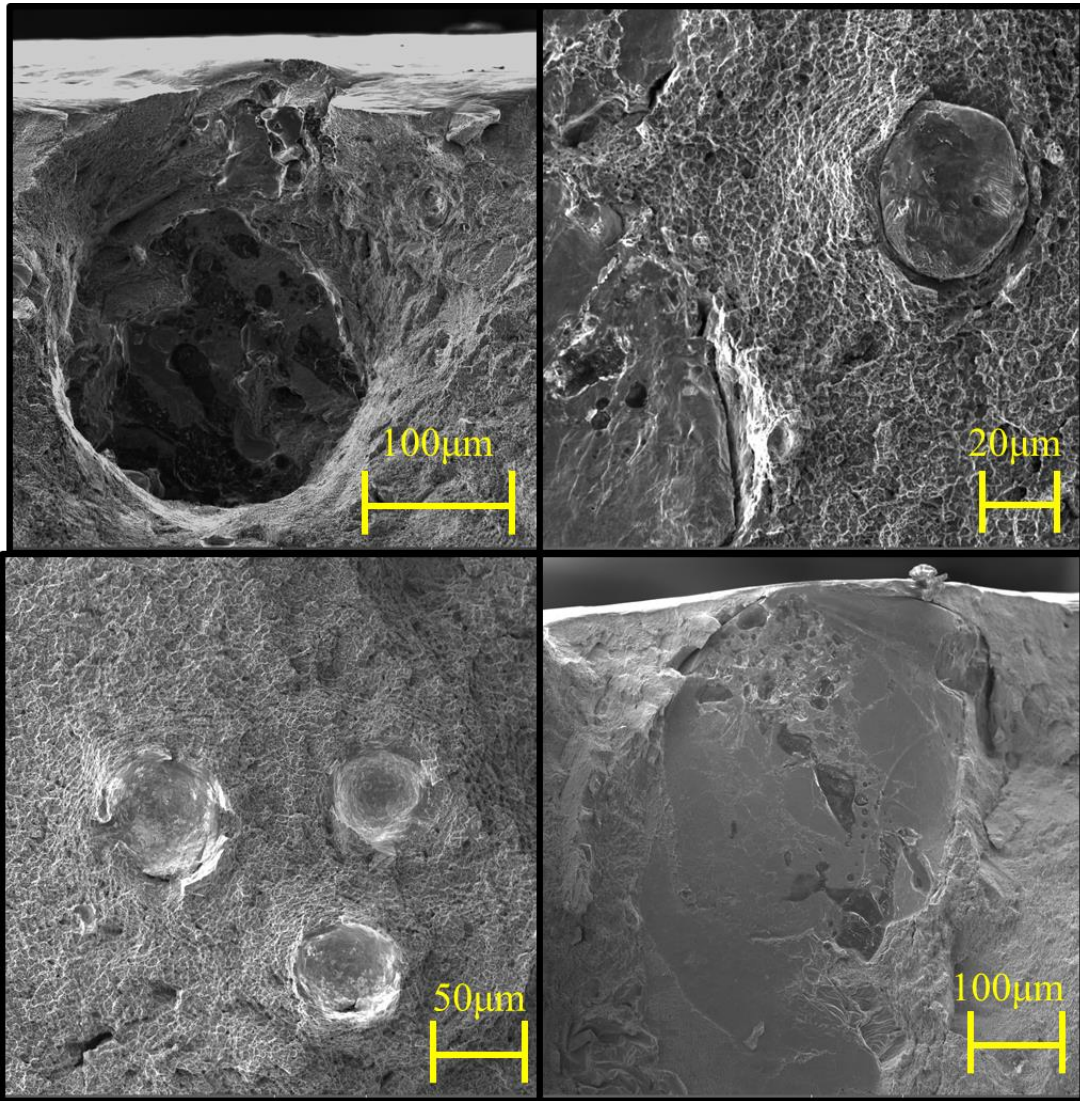


Figure 5.26 Fractography of SLM+EBW sample 17A/B (213.2 J/mm) fractured on the weld HAZ

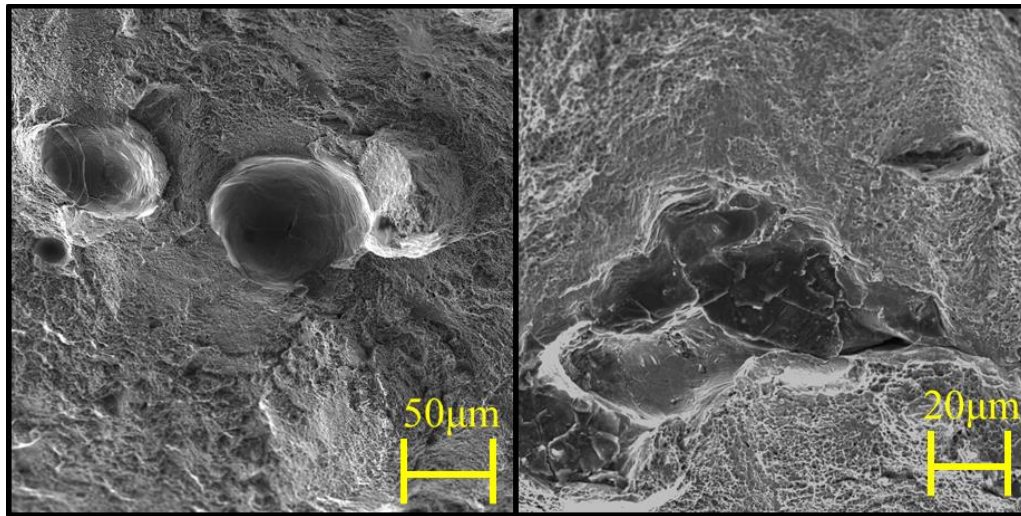


Figure 5.27 Fractography of as-printed SLM sample 20A/B

APPENDIX D

ENERGY DISPERSIVE SPECTROSCOPY

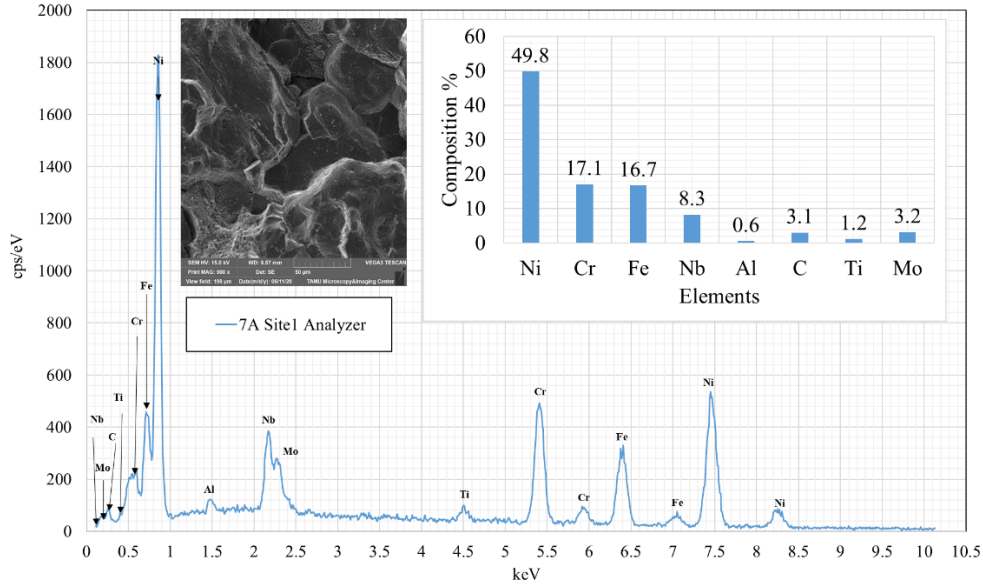


Figure 5.28 EDS of SLM+HIP+EBW sample 7A/B (213.2 J/mm) site 1

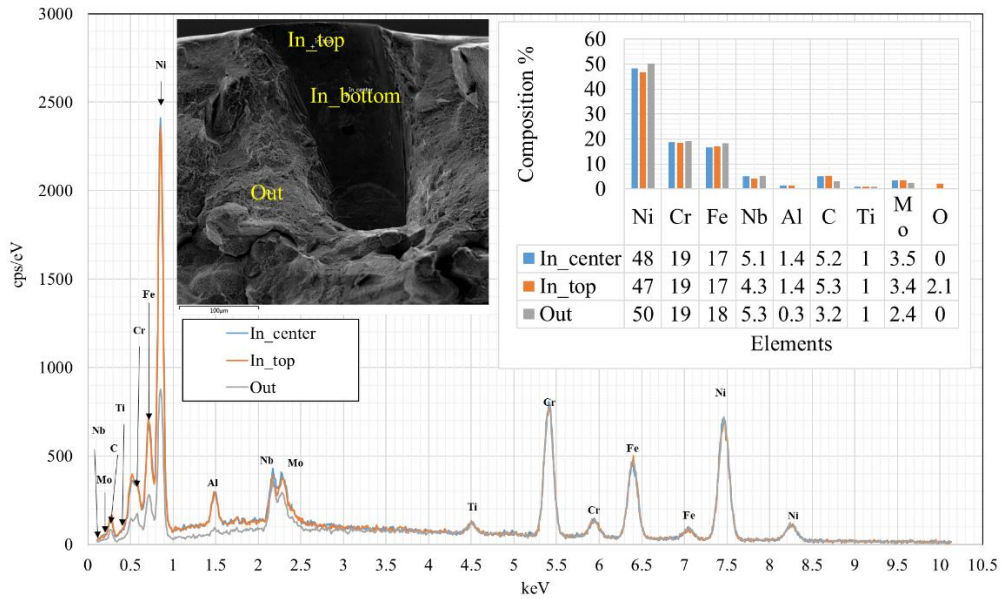


Figure 5.29 EDS of SLM+HIP+EBW sample 7A/B (213.2 J/mm) site 2

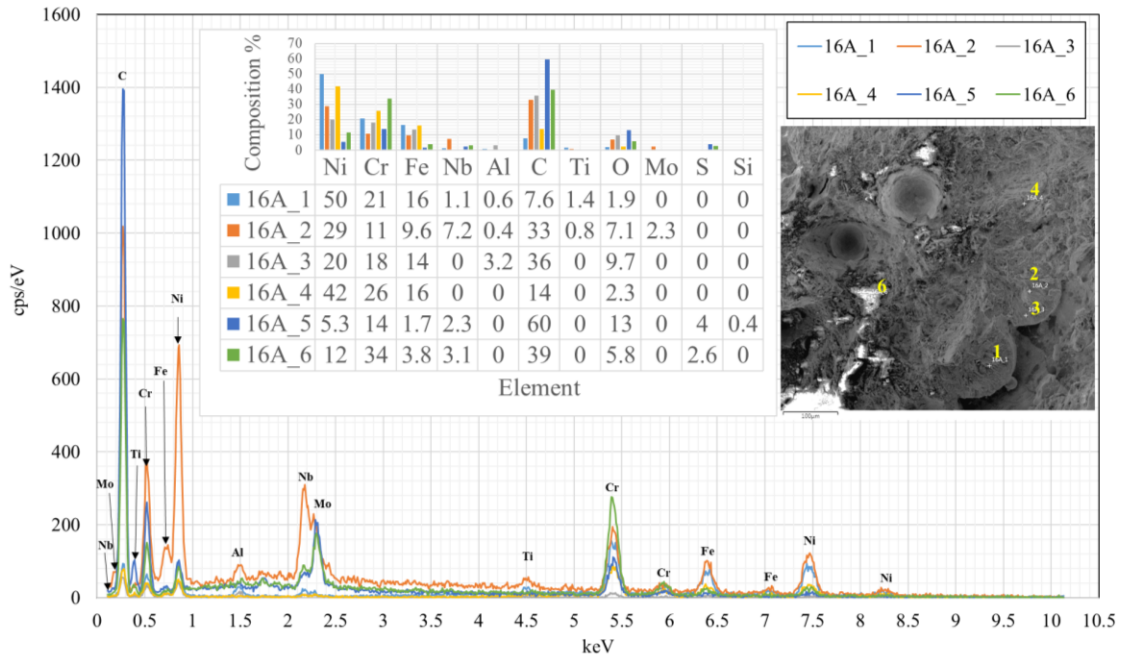


Figure 5.30 EDS of SLM+EBW sample 16A/B (209.6 J/mm) site 1

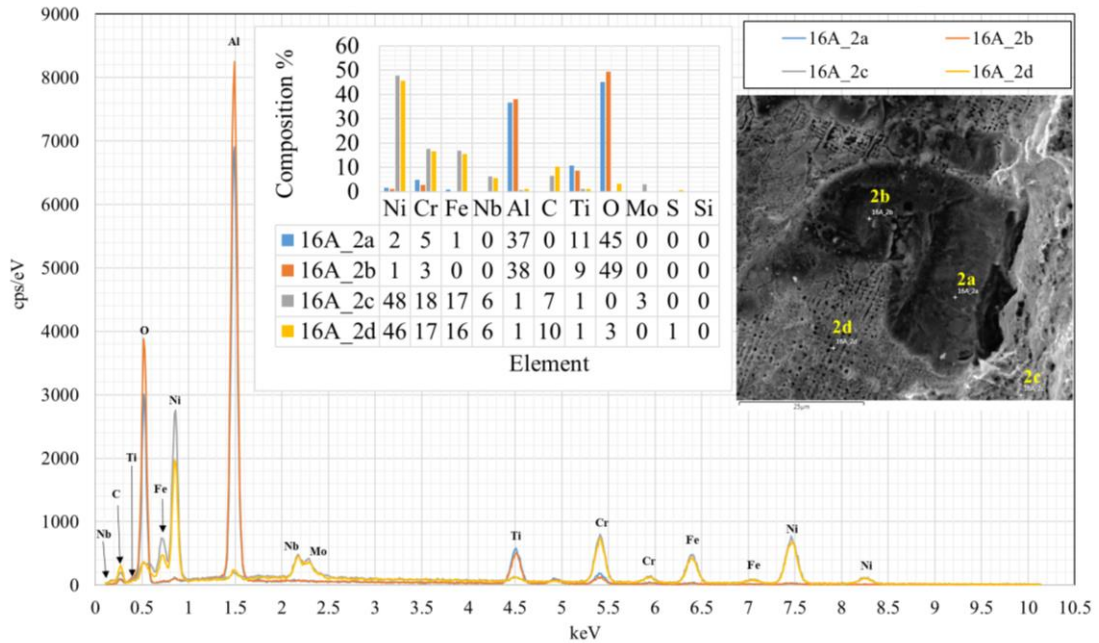


Figure 5.31 EDS of SLM+EBW sample 16A/B (209.6 J/mm) site 2

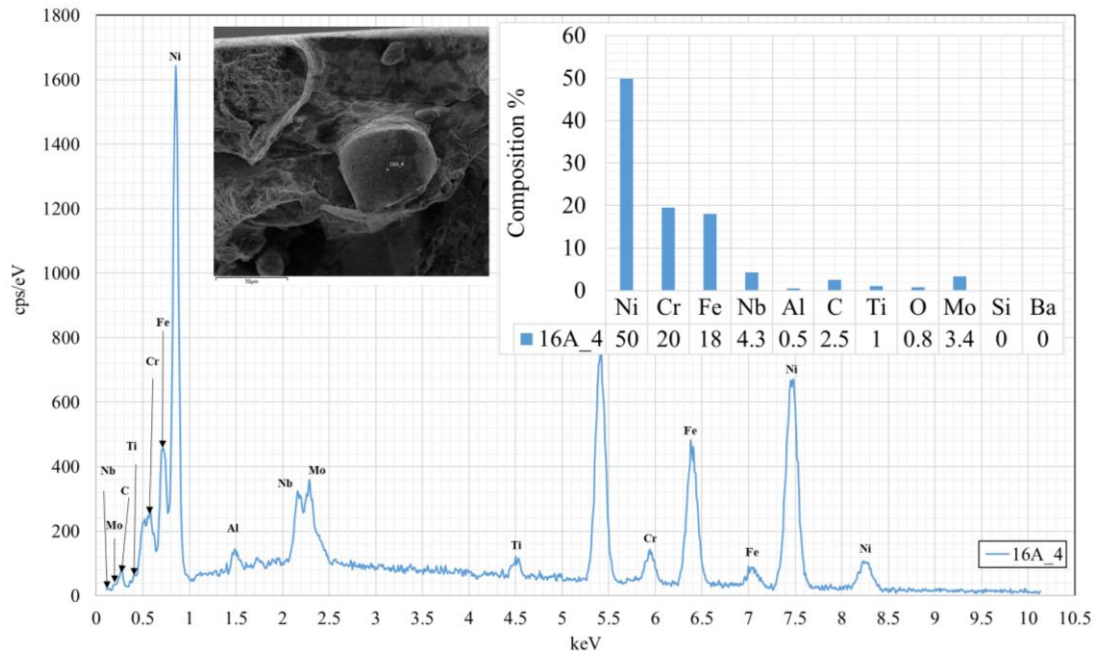


Figure 5.32 EDS of SLM+EBW sample 16A/B (209.6 J/mm) site 3

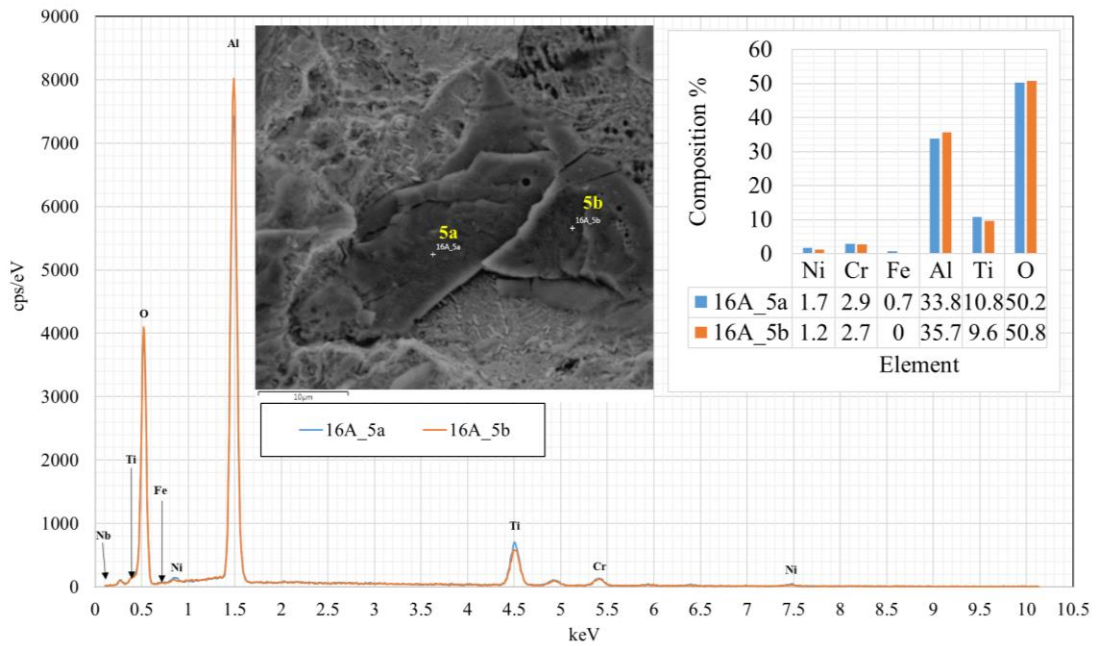


Figure 5.33 EDS of SLM+EBW sample 16A/B (209.6 J/mm) site 4

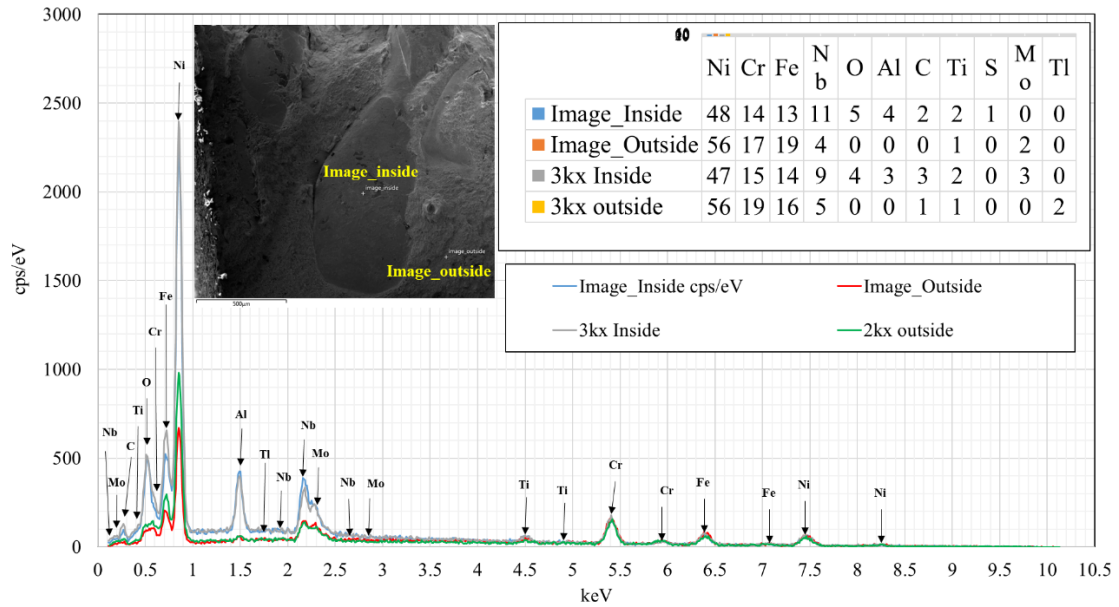


Figure 5.34 EDS of SLM+EBW sample 17A/B (213.2 J/mm) site 1

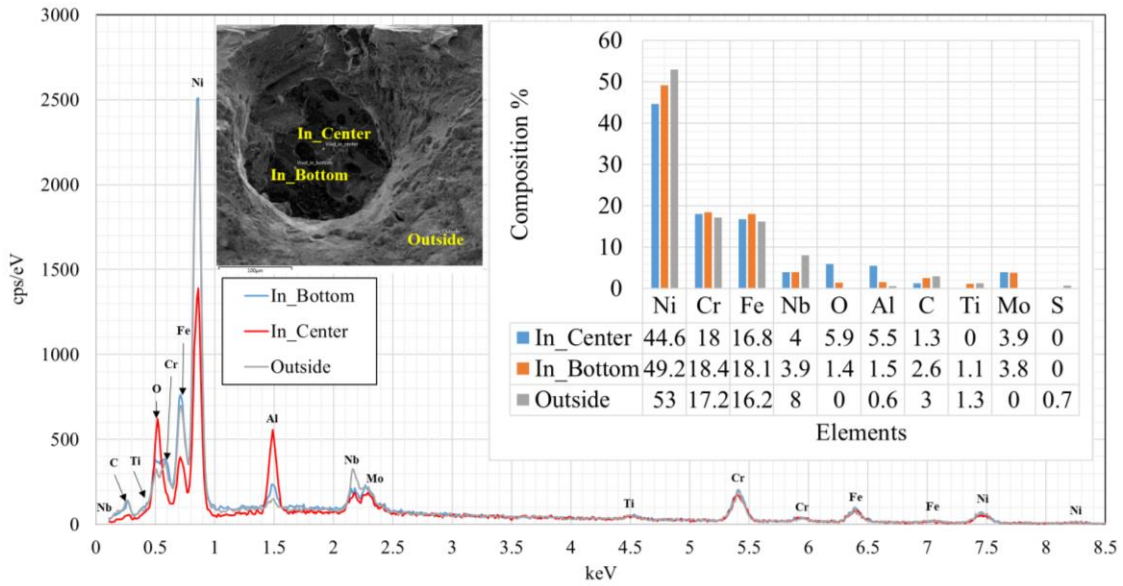


Figure 5.35 EDS of SLM+EBW sample 17A/B (213.2 J/mm) site 2

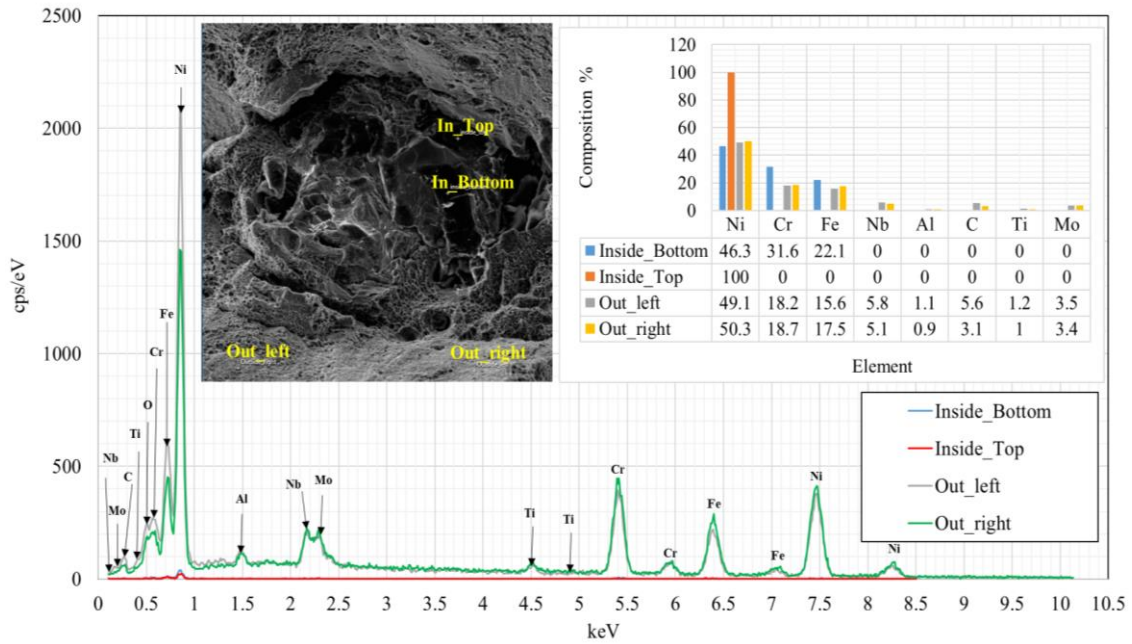


Figure 5.36 EDS of non-welded sample 20A/B site 1

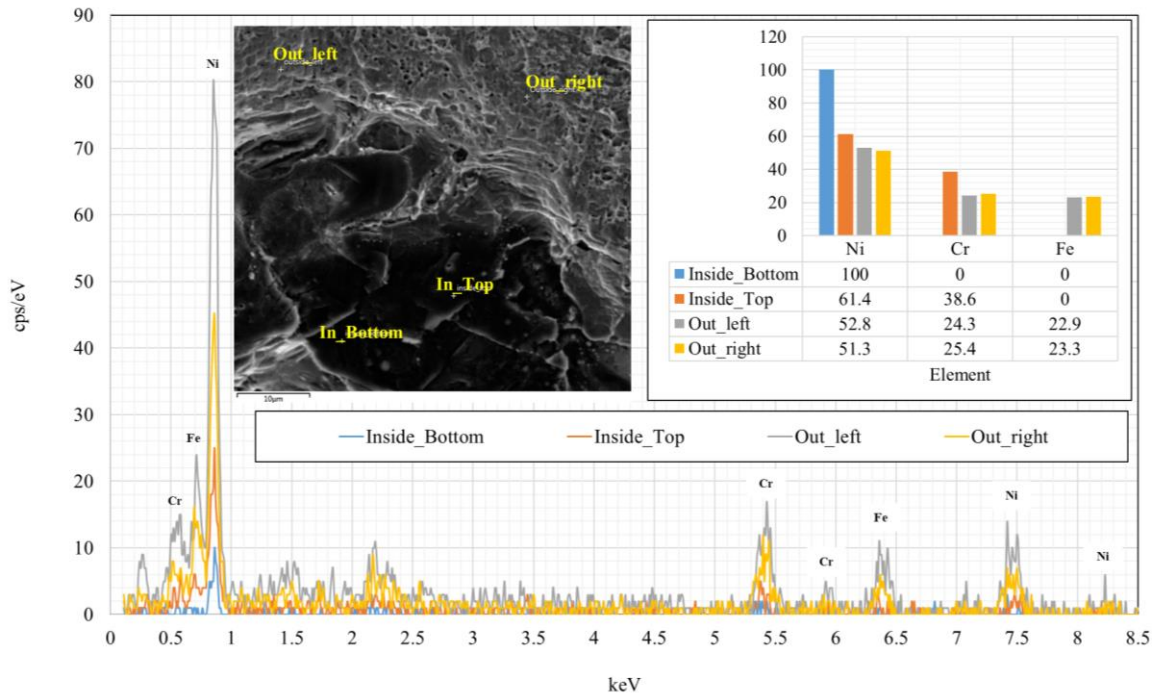


Figure 5.37 EDS of non-welded sample 20A/B site 2

APPENDIX E

MICROHARDNESS

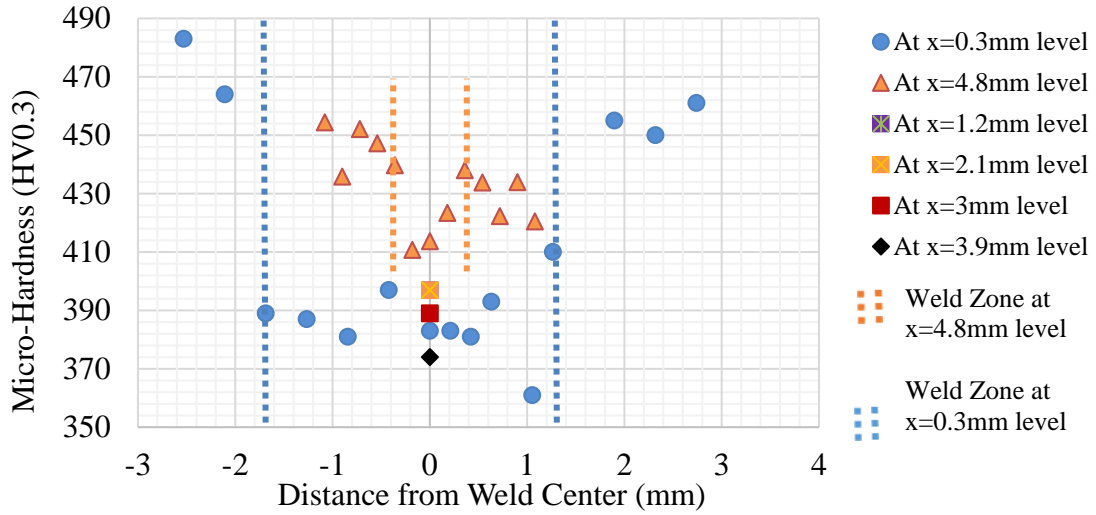


Figure 5.38 Microhardness test result of SLM+HIP+EBW sample 1A/B (295.3 J/mm)

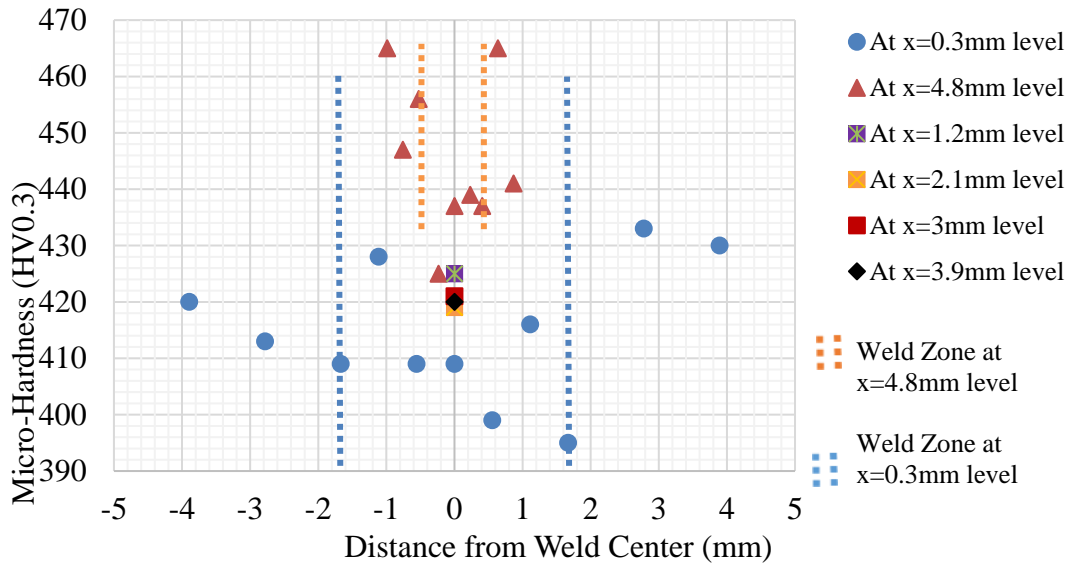


Figure 5.39 Microhardness test result of SLM+EBW sample 11A/B (295.3 J/mm)

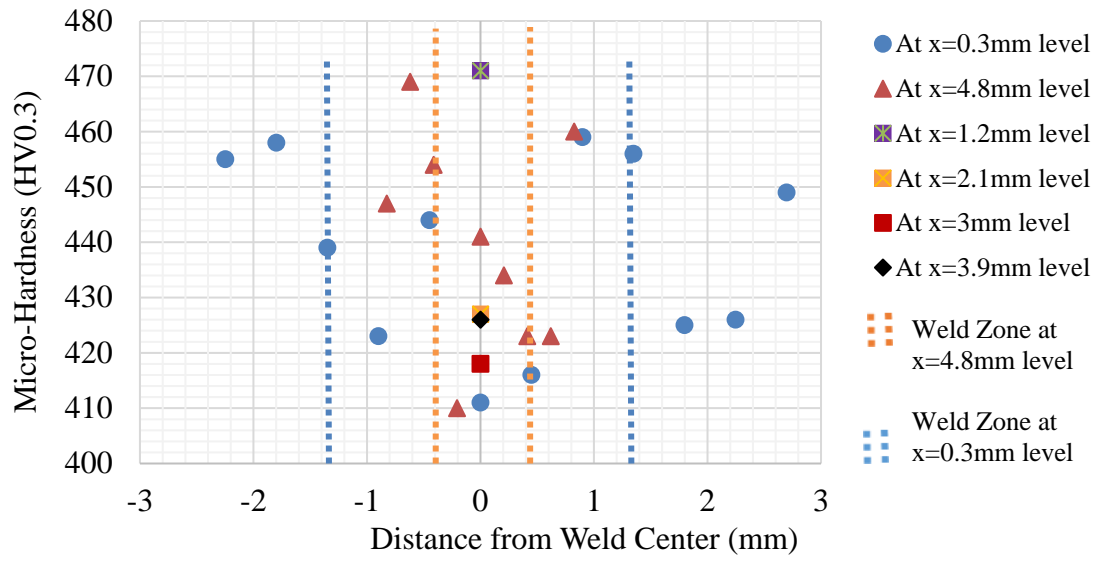


Figure 5.40 Microhardness test result of SLM+EBW sample 15A/B (228.6 J/mm)